Exploring the Effect of Polyfluorene Copolymerisation for Improved Material Design



Nikol Todorova Lambeva

Mansfield College

University of Oxford

A thesis submitted for the degree of

Doctor of Philosophy

Trinity 2020

Acknowledgements

My thanks go to my first supervisor Professor Donal Bradley for his support, guidance and insight throughout my DPhil, and to my second supervisor Professor Moritz Riede for his interest in my work and help during the final year of my studies. I thank Dr Toshihiro Ohnishi and Mr Takeshi Yamada of the Sumitomo Chemical Company Tsukuba Research Laboratory for supplying the following dioctylfluorene-arylamine copolymers used in the research described in Chapter 4: 95F8:5BSP, 90F8:10BSP, 80F8:20BSP and 50F8:50BSP; as well as the dioctylfluorene-phenoxazine copolymer F8BPPOZ used in the research presented in Chapter 5. I would also like to express my gratitude to Professor Youtian Tao and Xuyu Gao at Nanjing Tech University for providing the Pt-containing polyfluorene copolymers as well as the corresponding organic ligand copolymers described in Chapter 6.

I am most grateful to Professor Stephen Blundell for giving me the opportunity to follow my other passion - teaching, and trusting me with tutoring Mansfield students. He made Mansfield college feel like a home and without this my DPhil experience would not have been complete. I would like to thank him for the many stimulating discussions over college lunches and dinners and his constant support and encouragement throughout the past four years.

Many thanks go to my colleagues at the Department of Condensed Matter Physics. I would like to thank Alice, Florian and Bingjun for the many coffee breaks, experiment discussions and help, and for the late nights in the office which were made much easier in their company. I would like to also thank Claudius for his generous help with measurements, making sitting in a dark room all day enjoyable and a fun memory. I am also grateful to Saurav for his kind assistance with the APS measurements.

Last but not least, I would like to express my gratitude to my family for their support and always being there for me.

Не на последно място бих искала да благодаря на моето семейство за тяхната подкрепа и затова, че винаги са до мен.

Abstract

The discovery of electroluminescence from conjugated polymers was followed by tremendous academic and commercial interest in the field of polymer optoelectronics. Conjugated polymer materials have been shown to possess beneficial qualities for device fabrication such as low-cost, large area manufacturing and the potential for realizing flexible applications. Polyfluorenes, in particular, are a class of conjugated polymers which have been realized in a number of applications such as organic light emitting diodes, solar cells and field-effect transistors. The widespread commercialization of such products critically depends on improving device efficiencies. This can be accomplished by both advancing device engineering and improving material design. For the realization of the latter, fundamental understanding of the interplay between material chemistry and physics is required. This motivated the work in this thesis which is concerned with the structure-property relationship in polyfluorene containing copolymers. The well studied polyfluorene poly(9,9-dioctylfluorene) (PFO) was selected as the model polymer due to its complex phase morphology which allowed to additionally investigate the effect of film microstructure on the photophysics of the copolymers. The optoelectronic properties of PFO can be varied by the copolymerisation of suitable comonomers giving valuable insight into the relationship between chemical structure and photophysical properties that can guide future material design for device applications.

In this work three different comonomers have been studied. Firstly, the hole mobility of four fluorene-arylamine copolymers has been investigated. It is shown that transport in these copolymers is controlled over a large range by the copolymerisation of different amounts of a lower ionisation potential transporting moiety. Next, the effect of increasing backbone rigidity on hole carrier transport is studied via the copolymerisation of fluorene and phenoxazine. The resulting copolymer has a high glass transition temperature suggesting a rigid polymer chain. Yet, its hole mobility is lower than for the chemically similar hole transporting material poly(9,9-dioctylfluorene-*alt*-N-(4-butylphenyl)-diphenylamine) (TFB) which possesses a greater number of torsions. Finally, the copolymerisation of PFO with a cyclometalated platinum complex has been investigated. The heavy platinum atom increases spin-orbit coupling leading to the radiative decay of the triplet state. It is shown that at low temperatures kinetic frustration of the triplet state is lifted in the planarised β phase of the copolymer demonstrating that triplets can diffuse more effectively along highly conjugated polymer chains than along materials with short conjugation segments.

Contents

List of Figures **vii**

List of Tables **xi**

List of Abbreviations **xii**

1 Introduction **1**

2 Fundamentals **5**

2.1 The Electronic System of Conjugated Polymers 5
2.2 Conjugation Length 8
2.3 Density of States (DOS) 8
2.4 Excitations in Conjugated Polymers 9
2.5 Singlet and Triplet States 11
2.6 Radiative Transitions 13
2.6.1 The Electronic Factor 15
2.6.2 The Vibrational Factor 15
2.6.3 The Spin Factor 17
2.7 Electroluminescence 19
2.8 Nonradiative Transitions 20
2.9 Energy Transfer in Conjugated Polymers 21
2.9.1 Triplet-Triplet Annihilation 23
2.10 Aggregation and Quenching 24
2.11 Charge Transport 25
2.11.1 Band Transport 26
2.11.2 Hopping Transport 27
2.11.2.1 Polaronic Transport 27
2.11.2.2 Disorder-Controlled Transport 28
2.12 Charge Trapping 30
2.13 Poly(9,9-dioctylfluorene) Homopolymer 30
2.13.1 Conformation 31
2.13.1.1 Glassy Phase 32
2.13.1.2 β Phase 32

2.13.1.3 Crystalline Packing Arrangement 32
2.13.2 Optical Spectroscopy 33
2.14 Copolymers 36

3 Experimental Methods **38**
3.1 Optical Spectroscopy 38
3.1.1 Films for Spectroscopic Measurements 38
3.1.2 Absorption 39
3.1.3 Photoluminescence 41
3.1.4 Photoluminescence Quantum Efficiency 41
3.1.5 Temperature Dependent Photoluminescence 42
3.2 Electrical Characterisation 43
3.2.1 Dark Injection Transient Measurements 43
3.2.1.1 Dark Injection Transient Device Fabrication 45
3.2.2 Air Photoemission Spectroscopy 46
3.3 LED Characterisation 47

4 Arylamine Copolymerization **48**
4.1 Introduction 48
4.2 Materials 49
4.3 Optical Spectroscopy 51
4.4 Charge Transport 58
4.5 Conclusion 69

5 Phenoxazine Copolymerisation **71**
5.1 Introduction 71
5.2 Optical Characterisation 74
5.3 Thermal Characterisation 75
5.4 Electrical Characterisation 76
5.5 PLEDs 82
5.5.1 PLED Fabrication 83
5.5.2 PLED Characterisation 86
5.6 Polymeric Semiconductor Heterojunctions 91
5.7 Conclusions 96

6 Platinum-complex Copolymerisation **99**
6.1 Introduction 99
6.2 Materials 100
6.3 Absorption 102
6.4 Photoluminescence Spectroscopy 105

6.5 Triplet Energy Transfer 115
6.6 Excitation Power Dependence 122
6.7 Conclusion 124

7 Conclusions and Future Work **126**

Appendices

A Arylamine Copolymerisation **134**
A.1 Spectral Deconvolution for Determination of β Phase PL Contribution 134
A.2 Dark Injection Transient Measurements 137
A.3 Current-Voltage Characteristics 139

B Platinum-complex Copolymerisation **143**
B.1 Materials 143
B.2 Cyclometalated PyTPAPt(acac) Complex and Organic PyTPA Ligand 145
B.3 Temperature Dependence of Copolymer Photoluminescence Spectra 147

References **151**

List of Figures

2.1 Schematic illustration of π-bonding. 6
2.2 The singlet states S_0, S_1 and S_2 depicted in a one electron orbital diagram and in a many electron state diagram. 7
2.3 Schematic representation of different types of excitons in an organic crystal. 10
2.4 Schematic diagram of singlet and triplet states. 11
2.5 Absorption and emission in a conjugated polymer. 16
2.6 Singlet and triplet states in a state diagram. 18
2.7 Illustration of energy transfer by coulomb coupling (Förster energy transfer) and by exchange coupling (Dexter energy transfer). 22
2.8 Illustration of band transport and hopping transport under an applied electric field. 27
2.9 Depiction of the possible routes for a hole to travel from an initial state i to a final state j separated by an intermediate high-energy site k. 29
2.10 Chemical structure of poly(9,9-dioctylfluorene) (PFO). 30
2.11 The difference in intermonomer torsion angle between the glassy and β phases of PFO. 31
2.12 Peak normalized absorption and peak normalized PL of PFO thin films in the glassy phase and the β phase. 34

3.1 Schematic illustration of double beam absorption measurements with integrating sphere. 40
3.2 Illustration of the measurements performed to calculate PLQE. . . 42
3.3 Schematic illustration of the dark injection transient (DIT) method. 44
3.4 Cross section of the device structure of a hole-only copolymer DIT device. 45
3.5 Illustration of air photoemission spectroscopy. 46

4.1 Chemical structures of 100F8 (PFO) and the 9,9-dioctylfluorene:butyl-substituted phenylenediamine (F8:BSP) copolymers. 50

4.2 The thin film peak normalized PL spectra for hot spun and solvent annealed samples of PFO, 95F8:5BSP, 90F8:10BSP, 80F8:20BSP and PFB (50F8:50BSP). 52
4.3 The peak normalized PL spectra for solvent vapour annealed films of 90F8:10BSP following thermal annealing from 25 °C to 115 °C and 95F8:5BSP following thermal annealing from 25 °C to 130 °C. 54
4.4 Representative deconvolution of PL spectra for solvent vapour annealed film of 90F8:10BSP and solvent vapour annealed film of 95F8:5BSP following thermal annealing at 55 °C for 10 minutes. . . 56
4.5 The estimated β phase contribution to the PL emission as a function of thermal annealing temperature for solvent vapour annealed films of 90F8:10BSP and 95F8:5BSP. 57
4.6 Cross section of the device structure of a hole-only copolymer DIT device. 58
4.7 Representative hole injection transients for an 820 nm thick film of 50F8:50BSP under voltage pulses from bottom to top of 5, 6, 7, 8, 9, 10, 11 and 12 V. 59
4.8 Comparison of the room temperature field dependent hole mobility values for 50F8:50BSP, 80F8:20BSP, 90F8:10BSP and 95F8:5BSP. . 60
4.9 The room temperature hole mobilities of PFO, 95F8:5BSP, 90F8:10BSP, 80F8:20BSP and 50F8:50BSP at an electric field of $5 \times 10^5\,\mathrm{V\,cm^{-1}}$. 62
4.10 Illustration of charge trapping. 63
4.11 Air photoemission spectroscopy data for PFO, 95F8:5BSP, 90F8:10BSP, 80F8:20BSP and 50F8:50BSP. 65
4.12 Ionization potential energies derived from air photoemission spectroscopy for PFO, 95F8:5BSP, 90F8:10BSP, 80F8:20BSP and PFB. 67

5.1 Chemical structures of F8BPPOZ and TFB. 73
5.2 Peak normalized thin film absorption and photoluminescence spectra of F8BPPOZ. 74
5.3 DSC second heating/cooling thermograms of F8BPPOZ. 76
5.4 Air photoemission spectroscopy data for F8BPPOZ. 77
5.5 Representative hole injection transients for a 735 nm thick film of F8BPPOZ for voltage pulses from bottom to top of 5, 6, 7, 8, 9, 10, 11 and 12 V. 78
5.6 Field dependence of the hole mobility of F8BPPOZ. 79
5.7 Molecular geometries of TFB and poly[(10-methylphenoxazine-3,7-diyl)-*alt*-2,7-(9,9-dimethyl-fluorene)]. 80
5.8 PLED device structure and the corresponding schematic energy level diagram. 85

5.9 Current-voltage-luminance curves for PLEDs with no interlayer and with TFB, pristine F8BPPOZ and annealed F8BPPOZ interlayers. 87
5.10 Current-voltage plot of PLED with TFB interlayer. 88
5.11 Schematic energy level diagram for F8BPPOZ and Super Yellow. . 91
5.12 Schematic energy level diagram for heterojunction formed between F8BPPOZ and F8BT, TFB and F8BT, PFB and F8BT. 92
5.13 Thin film peak normalized photoluminescence spectra for TFB:F8BT and F8BPPOZ:F8BT blends as well as a reference F8BT film. . . . 93
5.14 Schematic illustration of exciton quenching and regeneration at TFB:F8BT and F8BPPOZ:F8BT heterojunctions. 94

6.1 Chemical structures of the investigated polyfluorene copolymers with cyclometalated PyTPAPt(acac) complex and organic PyTPA ligand. 101
6.2 The thin film absorption spectra of hot spun films and solvent vapour annealed films of the copolymers and PFO. 103
6.3 The absorption contribution of the PyTPAPt(acac) complex in the Pt copolymer absorption spectrum. 104
6.4 The thin film area-normalized PL spectra of hot spun films and solvent vapour annealed films of the copolymers and PFO. 106
6.5 The photoluminescence spectrum of a hot spun film of the 5% Pt copolymer at 5 K. 109
6.6 The photoluminescence spectra of solvent vapour annealed films of the Pt copolymers, the 5% ligand copolymer and PFO at 5 K and 300 K. 111
6.7 The phosphorescence spectrum of glassy phase and β phase 5% Pt copolymer at 5 K depicted on an extended energy scale. 114
6.8 Schematic illustration of spectral diffusion. 117
6.9 Fluorescence and phosphorescence spectra at selected temperatures for β phase PFO, 5% ligand, 5% Pt copolymers and glassy phase 5% Pt copolymer alongside the absorption spectra at 300 K. 118
6.10 Energy difference $\Delta\varepsilon$ between the center of the DOS and the center of the $S_1 \rightarrow S_0$ 0-0 fluorescence band or the center of $T_1 \rightarrow S_0$ 0-0 phosphorescence band normalized to σ versus kT/σ. 119
6.11 Dependence of fluorescence and phosphorescence on excitation power at 5 K for the β and glassy phases of the 5% Pt copolymer. 122

A.1 The peak normalized PL spectra for solvent vapour annealed films of 90F8:10BSP following thermal annealing from 25 °C to 115 °C and 95F8:5BSP following thermal annealing from 25 °C to 130 °C. 134

A.2 Full set of PL spectra deconvolutions for 90F8:10BSP solvent vapour annealed film following thermal annealing at stepwise increasing temperature intervals. 135
A.3 Full set of PL spectra deconvolutions for 95F8:5BSP solvent vapour annealed film following thermal annealing at stepwise increasing temperature intervals. 136
A.4 Representative hole injection transients for glassy phase films of 80F8:20BSP, 90F8:10BSP and 95F8:5BSP under voltage pulses from bottom to top of 5, 6, 7, 8, 9, 10, 11 and 12 V. 137
A.5 Representative hole injection transients for β phase films of 80F8:20BSP, 90F8:10BSP and 95F8:5BSP under voltage pulses from bottom to top of 5, 6, 7, 8, 9, 10, 11 and 12 V. 138
A.6 Current-voltage curves for hole-only devices made in a sandwich structure of ITO/PEDOT:PSS/Copolymer/Al with 50F8:50BSP, 80F8:20BSP, 90F8:10BSP and 95F8:5BSP. 141

B.1 Synthetic route to PyTPA ligand and PyTPAPt(acac) complex. . . 144
B.2 Synthetic route to polyfluorene copolymer with organic PyTPA ligand. 144
B.3 Synthetic route to polyfluorene copolymer with cyclometalated PyTPAPt(acac) complex. 144
B.4 The absorption spectra of the cyclometalated PyTPAPt(acac) complex and organic PyTPA ligand monomers in thin films and chloroform solutions. 145
B.5 The photoluminescence spectra of the cyclometalated PyTPAPt(acac) complex and organic PyTPA ligand monomers in thin films and chloroform solutions. 146
B.6 The temperature dependence of the thin film photoluminescence of β phase PFO. 147
B.7 The temperature dependence of the thin film photoluminescence of β phase 5% ligand copolymer. 148
B.8 The temperature dependence of the thin film photoluminescence of β phase 5% Pt copolymer. 149
B.9 The temperature dependence of the thin film photoluminescence of glassy phase 5% Pt copolymer. 150

List of Tables

4.1 Weight-average molecular weights of the fluorene-arylamine copolymers. 50
4.2 Comparison of the transport parameters of the four fluorene-arylamine copolymers and PFO. 61

5.1 Material chemical structures, electronic energy levels and electrical gaps of F8BPPOZ, TFB, PFO and F8BT. 84
5.2 Key device characteristics for PLEDs with and without interlayers. 89
5.3 Photoluminescence quantum efficiencies in thin films of F8BT and blends of TFB:F8BT and F8BPPOZ:F8BT. 93

6.1 Photoluminescence quantum efficiency in thin films at room temperature of the copolymers under study and PFO. 108

B.1 Weight-average molecular weight and polydispersity index of the Pt-containing fluorene copolymers and corresponding organic ligand copolymers. 143

List of Abbreviations

AFM . . . . . atomic force microscopy

Al . . . . . aluminium

APS . . . . . air photoemission spectroscopy

BSP . . . . . butyl-substituted phenylenediamine

Ca . . . . . calcium

CCD . . . . . charge coupled device

CDM . . . . . correlated disorder model

CT . . . . . charge transfer

CV . . . . . cyclic voltammetry

DIT . . . . . dark injection transient

DOS . . . . . density of states

DSC . . . . . differential scanning calorimetry

EA . . . . . electron affinity

EL . . . . . electroluminescence

EM . . . . . electromagnetic

EMA . . . . . effective medium approximation

FET . . . . . field effect transistor

F8 . . . . . 9,9-dioctylfluorene

F8BPPOZ . . poly(9,9-dioctylfluorene)-*co*-(10-(4-butylphenyl)phenoxazine)

F8BT . . . . . poly(9,9-dioctylfluorene-*alt*-bithiophene)

GDM . . . . . gaussian disorder model

HIL . . . . . hole injection layer

HOMO . . . . highest occupied molecular orbital

IDTBT . . . . indacenodithiophene-*co*-benzothiadiazole

IP . . . . . ionization potential

IL . . . . . interlayer

ITO . . . . . indium tin oxide

IVL . . . . . current-voltage-luminance

IV . . . . . current-voltage

LED . . . . . light emitting diode

LUMO . . . . lowest unoccupied molecular orbital

MA . . . . . Miller-Abrahams

MLCT . . . . . metal-to-ligand charge transfer

OLED . . . . . organic light emitting diode

PBTTT . . . . poly(2,5-bis(3-alkylthiophen-2-yl)thieno(3,2-b)thiophene)

PEDOT:PSS . poly(3,4-ethylenedioxythiophene):polystyrene sulphonate

PF . . . . . Poole-Frenkel

PFB . . . . . poly(9,9-dioctylfluorene-*alt*-bis-N,N'-(4-butylphenyl)-bis-N,N'-phenyl-1,4-phenylenediamine)

PFO . . . . . poly(9,9-dioctylfluorene)

PF2/6 . . . . . poly(9,9-bis(2-ethylhexyl)fluorene-2,7-diyl)

PL . . . . . photoluminescence

PLED . . . . . polymer light emitting diode

PLQE . . . . . photoluminescence quantum efficiency

PMMA . . . . poly(methyl methacrylate)

POZ . . . . . phenoxazine

PPV . . . . . poly(*p*-phenylene vinylenes)

Pt . . . . . platinum

SCLC . . . . . space charge limited current

SVA . . . . . solvent vapour annealed

TCA . . . . . triplet-charge annihilation

TFB . . . . . poly(9,9-dioctylfluorene-*alt*-N-(4-butylphenyl)-diphenylamine)

THF . . . . . tetrahydrofuran

TSL . . . . . thermally stimulated luminescence

TTA . . . . . triplet-triplet annihilation

UPS . . . . . ultraviolet photoelectron spectroscopy

1 Introduction

Scientific interest in conjugated polymers began in the 1970s with the discovery of high conductivities in doped polyacetylene [1]. This motivated subsequent research into the electronic properties of this class of materials and led to the key finding of polymer electroluminescence [2]. Ever since conjugated polymers have been the focus of extensive research due to their beneficial characteristics for technological applications.

The molecular nature of conjugated polymers results in comparatively weak van der Waals interchain bonding. This allows them to be solution processed with a range of deposition techniques including spin coating, ink-jet printing or industrial reel-to-reel coating. As a result they have the potential for low-cost, large surface area manufacturing. Additionally, the relatively weak intermolecular bonding enables low temperature processability resulting in straightforward and cost effective fabrication. Finally, conjugated polymers are particularly attractive due to the chemical tunability of their properties as well as mechanical flexibility and light weight.

The technological applications of conjugated polymers are constantly advancing. At the time of writing this thesis, interest lies in replacing vacuum deposition

by cheaper printing techniques as well as flexible device fabrication for the solar cell and display markets. To facilitate the exploitation of conjugated polymers in the commercial market a thorough understanding of the electronic processes in these materials is required. Their potential for chemical modification allows a large variety of structures to be synthesised, however, targeted development of materials with desirable device properties is necessary to improve device efficiencies that can dominate the market. Insight into the relationship between electronic properties and chemical structure would enable design of customized materials for specific applications. One approach for the modification of polymer properties is combining two or more monomers through covalent links between them called *copolymerization*. A copolymer structure can combine functionality without the unwanted phase separation often found in blends. To this end, studying suitable model systems is useful in order to gain a better understanding of the structure-property relationship in copolymers.

The potential of incorporating different amounts of a functional moiety into the backbone of a polymer via copolymerization for targeted material design motivated the research presented in this thesis. To investigate the structure-property relationship in such compounds, the well studied polyfluorene poly(9,9-dioctylfluorene) (PFO) was selected as the model polymer. PFO has become a promising material for display applications due to its efficient blue emission [3] and high hole mobility with trap free transport [4]. Furthermore PFO is an interesting system for the study of fundamental photophysical processes as it can be prepared in a variety of morphological phases [5, 6]. The morphological diversity of PFO allows to investigate the effect of film microstructure on material photophysics while keeping the chemical composition constant. Three different modifications have been investigated:

- the copolymerisation of PFO with an arylamine moiety,
- the copolymerisation of PFO with a phenoxazine unit,

- the copolymerisation of PFO with a cyclometalated platinum complex.

The content of this thesis may be summarised as follows:

Chapter 2 presents an introduction to the physics of conjugated polymers. This includes a review of fundamental optical properties and charge transport models. A special section is dedicated to the optoelectronic properties of PFO.

Chapter 3 describes the experimental methods used for the work in this thesis.

Chapter 4 presents a study of the hole charge carrier transport in four fluorene-arylamine copolymers comprising different ratios of 9,9-dioctylfluorene and butyl-substituted phenylenediamine. The dependence of the hole mobility on arylamine content has been investigated using dark injection transient measurements and the results are discussed in the context of a transition from trap-controlled to trap-to-trap hopping transport.

Chapter 5 introduces the characterization of a novel alternating fluorene-phenoxazine copolymer, F8BPPOZ. It is investigated whether increasing the backbone rigidity through the incorporation of the phenoxazine ring compared to the widely known hole transporting copolymer poly(9,9-dioctylfluorene-*alt*-N-(4-butylphenyl)-diphenylamine) (TFB) can improve charge hopping and increase hole carrier mobility. Subsequently, F8BPPOZ is tested as a hole injecting interlayer in a polymer light emitting diode and compared against TFB and devices without an interlayer. Finally, the exciton dynamics at a semiconductor polymer heterojunction with layers comprising blends of F8BPPOZ:F8BT and TFB:F8BT are studied.

Chapter 6 gives a thorough spectroscopic characterisation of a series of platinum containing polyfluorene copolymers. The platinum atom is introduced through a cyclometalated PyTPAPt(acac) complex embedded into the backbone of PFO. The heavy platinum atom increases the spin-orbit coupling in these compounds leading

to the radiative decay of the triplet state. It is found that the copolymers are able to adopt both the glassy and β phase chain conformations characteristic of PFO. The phosphorescence spectral diffusion in the two phases of the copolymer with the highest platinum content (5% Pt) is compared to give information about the triplet exciton transfer in disordered polymer films with different conjugation lengths.

Chapter 7 summarises the main conclusions of this thesis and offers suggestions for future work.

2 Fundamentals

The material in this chapter is primarily drawn from "Electronic Processes in Organic Semiconductors" by Anna Köhler and Heinz Bässler [7], "Molecular Quantum Mechanics" by Peter Atkins and Ronald Friedman [8], "Electronic Processes in Organic Crystals and Polymers" by Martin Pope and Charles Swenberg [9] and "Molecular Physics" by Wolfgang Demtröder [10].

2.1 The Electronic System of Conjugated Polymers

Conjugated polymers are organic compounds that can be regarded as a chain of molecular repeat units covalently bound together. They mainly consist of carbon atoms that are found both in the backbone and in the side chains attached to it. Their favourable electronic and optical properties arise from the π-electron system that extends along the polymer backbone. The mechanism that gives rise to this delocalised π-electron system is orbital hybridisation in carbon [10].

Atomic carbon has the configuration $(1s)^2(2s)^2(2p_x)^1(2p_y)^1(2p_z)^0$, in this form it can form two covalent bonds. Whenever other atoms approach as binding partners one of the two electrons of the $2s$ orbital is promoted to the empty $2p_z$ orbital and

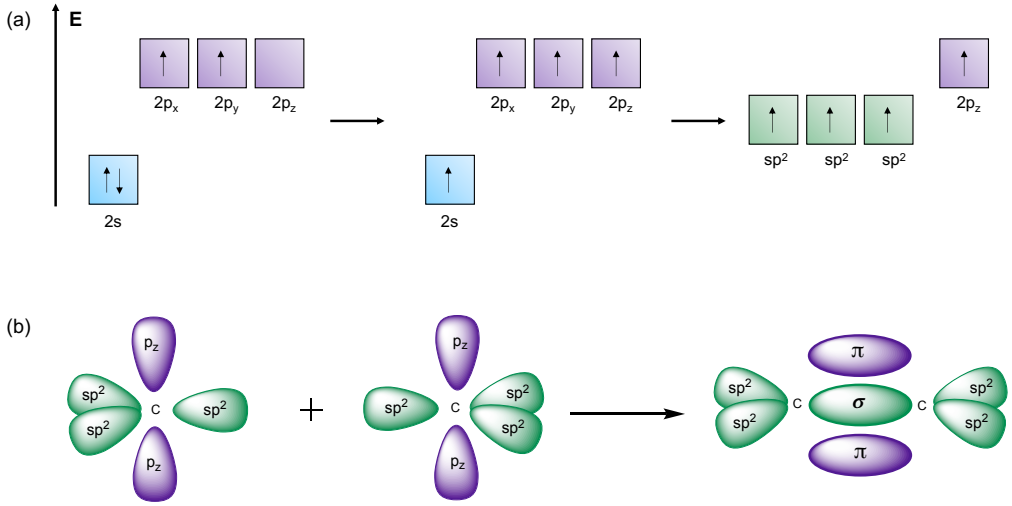


Figure 2.1: Schematic illustration of π-bonding. (a) The formation of sp^2 hybrid orbitals from s and p atomic obitals. (b) σ and π bonds in ethene (the hydrogen atoms are omitted for clarity). Adapted from [11].

in this configuration it can form four covalent bonds (figure 2.1 (a)). This happens since the binding energy gained in making additional bonds exceeds the energy required to promote the electron to the empty orbital. The mixing of the $2s$, $2p_x$ and $2p_y$ orbitals results in the formation of three hybrid sp^2 orbitals which lie in the xy-plane at 120° to each other. The remaining $2p_z$ orbital is orthogonal to that plane and each orbital contains an electron that is available for forming bonds (figure 2.1 (b)). The three sp^2 hybrid orbitals give rise to three σ bonds that make up the polymer backbone, while the p_z orbitals of adjacent carbon atoms overlap forming a delocalised π orbital above and below the molecular axis [8, 10].

The p_z orbitals overlap constructively and destructively leading to a bonding π orbital (the highest occupied molecular orbital - HOMO) and an antibonding π^* orbital (the lowest unoccupied molecular orbital - LUMO), respectively. The energy splitting between the bonding and antibonding orbitals largely depends on the resonance integral between those orbitals. The resonance integral measures the interaction between a nucleus and the overlap of two atomic orbitals located on different centres [7]. This leads to the lower splitting between the π and π^*

compared to the σ and σ^* orbitals as the π electron overlap density is further away from the internuclear axis. In this manner, the σ bonds hold the polymer together while the π orbitals contribute little to the attractive force between units in the polymer chain. It is this lower splitting of the π orbitals that allows conjugated polymers to absorb and emit light in the visible range and inject charges from metal electrodes making them suitable for semiconductor application.

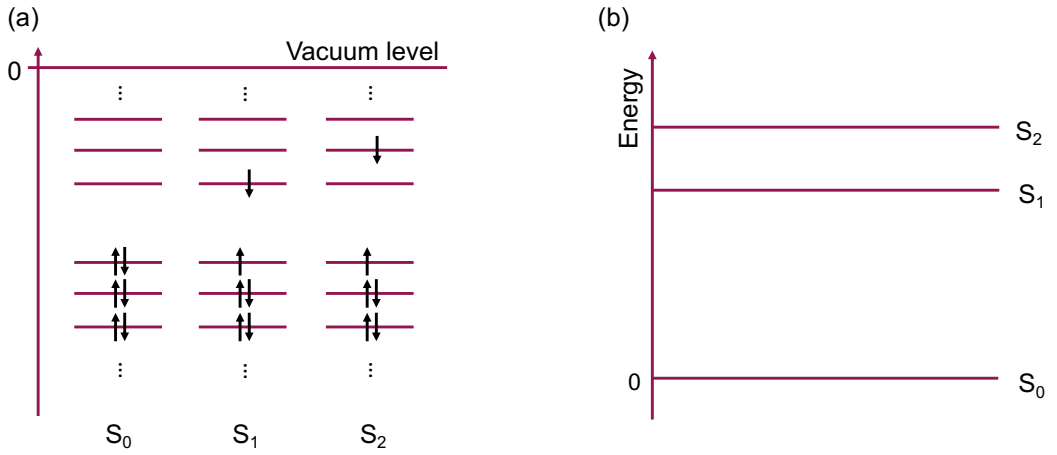


Figure 2.2: The singlet states S_0, S_1 and S_2 depicted (a) in a one electron orbital diagram and (b) in a many electron state diagram. Adapted from reference [7].

It is important here to distinguish between one electron orbitals and many electron states in order to avoid confusion in following discussions. Molecular orbital energies are below the vacuum energy since electrons in orbitals are bound to nuclei. In an orbital picture usually only the HOMO and LUMO are drawn, however, there will be more molecular orbitals at energies above and below (figure 2.2 (a)). An alternative electronic state picture exists where the lowest possible state of the molecule, the ground state, acts as a reference at zero energy. This picture is particularly useful when trying to represent effects due to electron-electron interactions, for example. Here the energies of the excited states have positive values and there are no states below the ground state (figure 2.2 (b)). A final point to note is the difference between HOMO and LUMO energies and ionization potential and electron affinity. The ionization potential is defined as the energy required to

remove an electron from a neutral molecule while the electron affinity is the energy gained when placing an electron onto a neutral molecule. These are not equivalent to the HOMO and LUMO energies introduced above because they are defined in a one electron orbital picture neglecting electron correlation effects such as coulomb binding between charges [12].

2.2 Conjugation Length

Moving from a system with two carbon atoms to a polymer chain, the π orbitals allow electrons to delocalise along the whole polymer backbone making it one homogeneous unit. This can occur for polymer chains containing alternating single (σ) and double bonds (σ and π) between carbon atoms. As a result of structural periodicity not only neighbouring π orbitals overlap but theoretically all π electrons are delocalised over the chain. This phenomenon is termed *conjugation*. In practice, the delocalisation is limited to an *effective conjugation length* due to impurities and chemical chain defects which interfere with the conjugation system. Additionally, twists between repeat units can reduce the spatial overlap between neighbouring p_z orbitals by forcing them out of plane again leading to a decreased conjugation length. The conjugation length of a polymer strongly influences its optoelectronic properties and represents the chromophore. Lastly, increased conjugation and, thereby, delocalisation of the electrons leads to lowering of the excited state energies of the conjugated system analogous to a particle in a box model. This is observed as a red shift of the absorption and emission spectra of polymers [13].

2.3 Density of States (DOS)

As conjugated polymers are a disordered system they do not have a set of discrete energy levels but a distribution of states. The energy levels vary statistically as a result of spatial fluctuations of the dielectric polarization. This can be modelled by

a Gaussian distribution, $g(\varepsilon) = \left(1/\sqrt{2\pi\sigma}\right) \exp\left(-\left(\varepsilon - \varepsilon_0\right)^2 / 2\sigma^2\right)$, where ε is the energy of an individual molecule, ε_0 is the energy of the centre of the distribution and the standard deviation σ, also known as the disorder parameter, describes the width of the distribution. The distribution arises from both the van der Waals interactions with neighbouring sites and the variation of the lengths and therefore the energies of the conjugated segments of the polymer chains [7].

2.4 Excitations in Conjugated Polymers

In conjugated polymers the occupancy of electronic states is strongly connected to the chain geometry (electron-phonon coupling). The fundamental excitations are polarons, bipolarons and excitons. A *positive* or a *negative polaron* is an additional or missing electron (hole) on a chromophore together with the associated molecular distortion resulting from the electron-phonon coupling [9]. This molecular distortion reduces the energy of the system and results in the polaron energy level being located inside the HOMO-LUMO energy gap. A pair of like polarons can form *positive* or *negative bipolarons*.

A geminate pair of positive and negative polarons strongly bound by coulomb interaction is called an *exciton*. The coulomb interaction leads to the shift of the exciton energy further into the HOMO-LUMO gap by the exciton binding energy. The exciton binding energy arises from the low dielectric constant in organic semiconductors ($\epsilon \approx 3.5$). In comparison, the dielectric constant in inorganic semiconductors is higher (for crystalline silicon $\epsilon \approx 12$) and the coulomb effects between electrons and holes are insignificant due to efficient dielectric screening. Further, the electron-electron interactions in organic semiconductors lead to a difference in the optical and electrical gap. The optical gap of organic semiconductors, E_{opt}, is the energy of the first excited state of a molecule, $E_{opt} = E_{S_1}$, found from the absorption or fluorescence spectra. The electrical gap, E_{el}, is defined as the difference between the electron affinity, E_a, and ionization potential, I_p, of a

molecule, $E_{el} = I_p - E_a$. In an inorganic semiconductor due to the high dielectric constant the energies of the optical and electric gap are the same. However, in an organic semiconductor where the lower dielectric constant no longer screens electron-electron interactions, the onset of absorption is below the energy difference between the ionization potential and electron affinity. The optical and electrical gap in an organic semiconductor differ by the exciton binding energy, $E_b = E_{el} - E_{opt}$ [12].

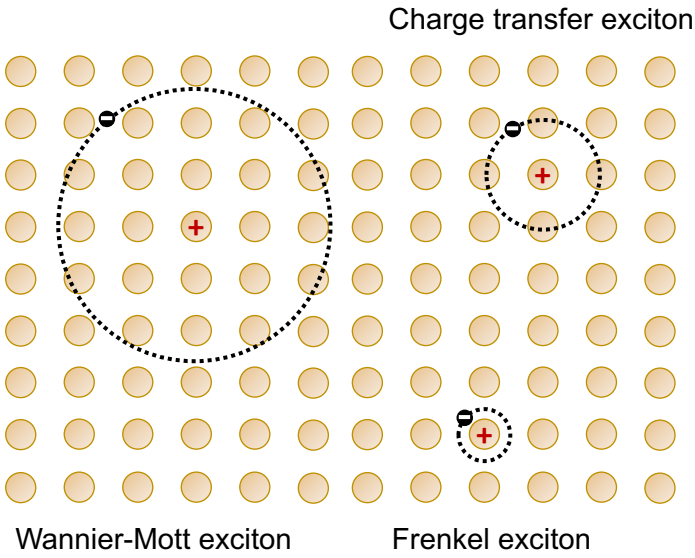


Figure 2.3: Schematic representation of different types of excitons in an organic crystal. In this point charge diagram, the electron orbits around the positively charged molecule either at a distance shorter than the lattice constant for a Frenkel exciton, at a distance comparable to the lattice constant for a charge transfer exciton or at a very large distance in comparison to the lattice constant for a Wannier-Mott exciton. After [9].

Excitons can be classified into three different types depending on the size of their binding energy, those have been defined in terms of organic crystals and are schematically represented in figure 2.3. The most strongly bound excitons are called *Frenkel excitons* where the electron and hole are located on a single conjugated unit. In *charge transfer (CT) excitons* the electron or the hole has been transferred to a neighbouring chain. The third type of exciton is the *Wannier-Mott exciton* where the electron and hole are separated by a large distance. Finally, the excitons can be of either singlet or triplet nature. The distinction between singlet and triplet

excited states will be discussed in more detail in the next section.

2.5 Singlet and Triplet States

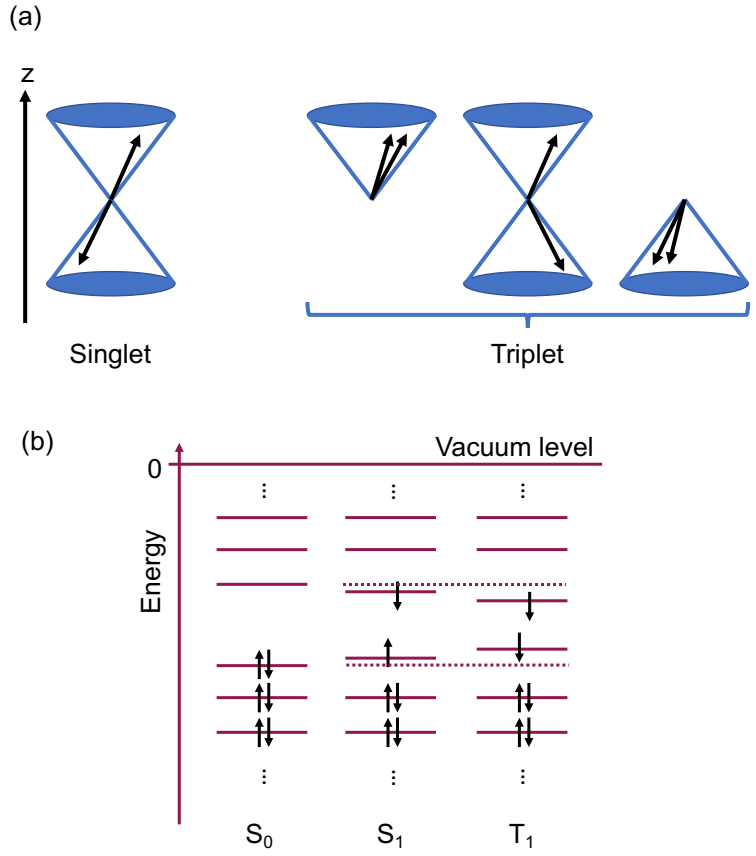


Figure 2.4: Singlet and triplet states. (a) Singlet and triplet states represented in a vector diagram showing the relative orientations of the spins of the two electrons for the singlet and triplet states. The spins are depicted as arrows precessing around a local magnetic field in the z-direction. The singlet state corresponds to an antiparallel and 180° out of phase configuration while the three in-phase configurations represent a triplet state. (b) Singlet and triplet states in an orbital diagram. The arrows depict the spin of the electrons, coulomb and exchange energies are included in the positions of the frontier orbitals. Only one spin configuration is drawn for the triplet state. After [8].

Following the approach given by Anna Köhler and Heinz Bässler in reference [7], to move conceptually from molecular orbitals to the ground and excited electronic states of a molecule, we can adopt a wavefunction representation where the total wavefunction of a molecular state, Ψ_{total}, is approximated by the product of

an electronic wavefunction, Ψ_{el}, a spin wavefunction, Ψ_{spin}, and a vibrational wavefunction, Ψ_{vib}. The electronic wavefunction depends on the position of the electrons and the position of the nuclei. The vibrational wavefunction describes the vibrational motion of the nuclei while the spin wavefunction reflects the electron's spin. For a complete description of the molecule's state the spin of the electrons needs to be taken into account. The spin of a state is equal to the total spin of all the electrons in all orbitals but since the electrons in filled orbitals have their spins antiparallel and add up to zero, we only need to consider the spins of unpaired electrons. Usually, these are an electron in a π^* orbital and another one in a π orbital. The motion of their spin vectors relative to one another determines whether the state is a singlet or a triplet. The singlet is a state where the two spin vectors are in anti-phase, whereas a triplet states is defined as any of the three possible in-phase spin vector configurations (figure 2.4 (a)) [8].

The ground state of aromatic hydrocarbons is a singlet since the two electrons are in the same lowest energy orbital and due to the Pauli principle, their spins must be in anti-phase. Since in the excited state the two electrons are in different orbitals they can be in either a singlet or triplet state. The energies of the first singlet and first triplet excited states differ by the exchange energy. The exchange interaction represents the electrostatic repulsion between the electrons, one in a π^* orbital and the other one in a π orbital, and it is proportional to the overlap of the electron wavefunctions. The energy of the triplet is lower since the electron-electron repulsion is minimised in the triplet configuration (figure 2.4 (b)). This is due to the fact that the electrons in the triplet state have a symmetric spin wavefunction and an antisymmetric spatial wavefunction [8]. The motion of a pair of electrons in the triplet state is better coordinated than in the singlet state since the Pauli principle acts like a quantum mechanical force helping the electrons to avoid one another [14]. For conjugated polymers the $S_1 - T_1$ gap is experimentally found to be about 0.7 eV irrespective of chemical structure [15–17].

It is informative to mention here that the energetic distinction between the singlet and triplet state in inorganic semiconductors is marginal since the exchange energy is small due to the large polarizability in inorganics as seen from the large dielectric constant. The large polarizability means that electron-electron interactions can be neglected, whereas in organic semiconductors coulomb and exchange interaction are central and largely determine the material photophysical properties.

To convert between singlet and triplet states there needs to be a magnetic torque able to flip or rephase the spin vector of only one of the electrons in the pair. This cannot be done by an externally applied magnetic field or the magnetic field of an electromagnetic wave since it will act on the spins of both electrons in the pair. This is the origin of the quantum mechanical selection rule that the spin of a system remains unchanged in an optical transition.

2.6 Radiative Transitions

The intensity of light absorption (emission) depends on the number of photons absorbed (emitted) per unit time per molecule. This can be expressed by a transition rate, k_r. Upon absorption (emission) the total energy of a molecule increases (decreases) by a certain amount. Still following the treatment in reference [7], to calculate the transition rate in terms of quantum mechanics an appropriate term needs to be added to the Hamiltonian. The new Hamiltonian, $\widehat{H}$, would be the sum of the original, $\widehat{H_0}$, and the new term, $\widehat{H'}$. Since the ability of a material to absorb and emit light depends on how easily it can follow a change in applied electric field, the electric dipole operator, $e\hat{r}$, would be a suitable operator for light absorption and emission. Thus, we would expect the new wavefunction to be an eigenfunction of this operator and the eigenvalue to reflect the energy of the molecule in the excited state. To calculate the transition rate between an initial wavefunction, Ψ_i, and a final wavefunction, Ψ_f, we use Fermi's golden rule which tells us how the transition rate, k_r, depends on the perturbing Hamiltonian which causes the transition:

$$k_r = \frac{2\pi}{\hbar}|\langle\Psi_f|\widehat{H'}|\Psi_i\rangle|^2\rho, \tag{2.1}$$

where ρ is the density of the final states and $\hbar$ is the reduced Planck constant. Inserting the total molecular wavefunction, $\Psi_{total} = \Psi_{el}\Psi_{vib}\Psi_{spin}$, introduced in section 2.5 and using the dipole operator we obtain

$$k_r = \frac{2\pi}{\hbar}|\langle\Psi_{el,f}\Psi_{vib,f}\Psi_{spin,f}|e\hat{r}|\Psi_{el,i}\Psi_{vib,i}\Psi_{spin,i}\rangle|^2\rho. \tag{2.2}$$

The dipole operator only acts on the electronic wavefunction since the time-dependent electrical dipole of the electromagnetic (EM) wave would make the electrons move in resonance. The vibrational wavefunction would not be affected as the nuclei are too heavy to respond on the time scale of the oscillation and the spins are only influenced by the magnetic field of the EM wave which would be too small to have a significant effect [7]. We can, thus, rearrange the transition into three separate factors each of which would affect the transition rate

$$k_r = \frac{2\pi}{\hbar}\rho|\langle\Psi_{el,f}|e\hat{r}|\Psi_{el,i}\rangle|^2|\langle\Psi_{vib,f}|\Psi_{vib,i}\rangle|^2|\langle\Psi_{spin,f}|\Psi_{spin,i}\rangle|^2. \tag{2.3}$$

In conclusion, the macroscopic intensity of absorption and emission depends on the following three factors:

- The electronic factor
- The vibrational factor
- The spin factor

If any of these takes the value of zero the transition is said to be forbidden [7].

2.6.1 The Electronic Factor

Here, we refer to the integral $\langle \Psi_{el,f} | e\hat{r} | \Psi_{el,i} \rangle$ as the electronic factor. Depending on whether the value of this expression is equal or not to zero the transition is termed dipole-forbidden or dipole-allowed, respectively. The value of the integral depends on both the wavefunction overlap of the initial and final state and the value of the transition dipole moment. This means that transition rates between orbitals that occupy the same region of a molecule such as $\pi - \pi^*$ transitions would be larger than transitions between orbitals that are located in different places such as charge transfer (CT) transitions [7]. Additionally, the transition rate would be higher for orbitals with large transition dipole moment. Therefore, the transition rate would be large for well overlapping and well extended orbitals with transition dipole moment along the molecular axis.

2.6.2 The Vibrational Factor

While the electronic factor can be viewed as determining the overall transition intensity, the vibrational factor, $\langle \Psi_{vib,f} | \Psi_{vib,i} \rangle$, controls the spectral shape of absorption and emission. The electronic and vibrational energy levels as a function of configuration coordinate, Q, of a molecule are schematically shown in figure 2.5 (a). The shape of the electronic levels reflects the fact that as the nuclei approach each other the resonance interaction between atomic orbitals takes place and reduces the energy of the state, while at very small internuclear distances the Pauli exclusion principle raises the energy of the molecule as a result of repulsive interactions and a minimum is formed in between [7]. Since the excited state, S_1, will be in an antibonding orbital there will be less binding force between atoms in the molecule compared to the bonding ground state, S_0. This is reflected in the diagram in the greater equilibrium separation of atoms in the S_1 state compared to S_0. The vibrational levels are represented by horizontal lines.

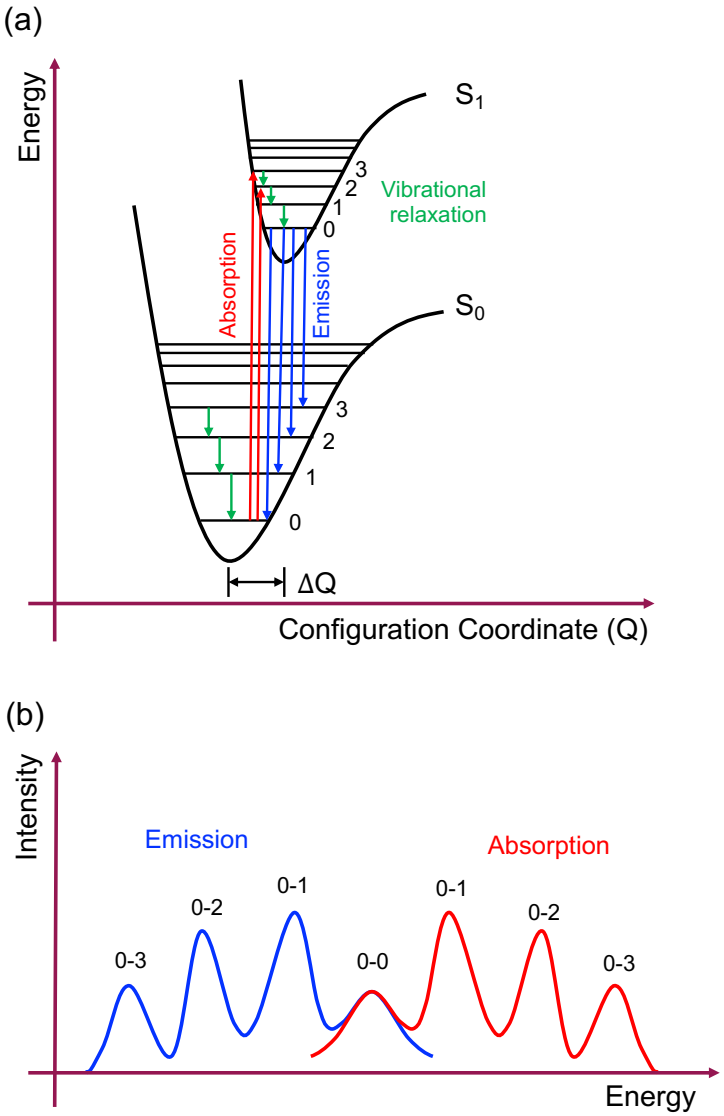


Figure 2.5: Absorption and emission in a conjugated polymer. (a) The electronic and vibrational potential energy levels of a molecule as a function of configuration coordinate. (b) A schematic of the absorption and emission spectra of a conjugated polymer. Adapted from [9].

Light absorption by a molecule results in the promotion of an electron from the lowest vibration level of the ground S_0 state to any of the higher energy singlet excited states and vibrational levels. Transitions are indicated by vertical arrows as the Born-Oppenheimer approximation applies for conjugated polymers. This states that the motion of electrons is much faster than the motion of nuclei so the nuclei can be considered stationary during an electronic transition [8]. This leads to the *Franck-Condon principle* that electronic transitions are much faster than vibrational

ones and so there is not enough time for a change in configuration coordinate. Once the molecule is in the excited states it loses vibrational energy by the emission of phonons and returns to the lowest vibrational level of the S_1 state. When a photon is emitted the transition takes place from the lowest vibrational level of the excited state to any of the vibrational levels of the ground state as illustrated in the diagram. The strength of the transition is determined by the vibrational factor, namely, by the vibrational wavefunction overlap of the initial and final states. The degree to which ground and excited state are radiatively coupled is determined by the *Huang-Rhys factor* which is related to the distortion of an excited state as a result of the displacement ΔQ from the ground state [7].

The idealised emission and absorption spectra would be mirror images of each other as illustrated in figure 2.5 (b). However, a complication arises in conjugated polymers due to the variety of conjugation lengths that can exist in a single polymer sample. In emission, excitations not only relax to the lowest vibrational energy level of the excited state but the excitons also migrate by hopping to the chromophores with the longest conjugation lengths and the lowest energies. Yet, in absorption all conjugation lengths are sampled at once leading to significant inhomogeneous broadening of the absorption spectrum. Finally, due to the vibrational relaxation of excitations to the bottom of the excited state potential, the wavelength of fluorescence is always longer than the wavelength of absorption. This energy loss via the relaxation of the molecule in the excited state is quantified by the *Stokes shift* which is the energy difference between the absorption edge and fluorescence onset.

2.6.3 The Spin Factor

The final term in the molecular wavefunction is the spin factor, $\langle \Psi_{spin,f} | \Psi_{spin,i} \rangle$. It can take only two values. It is equal to one if the spins of the initial and final states are the same and it is equal to zero if they are not. The implication of this is

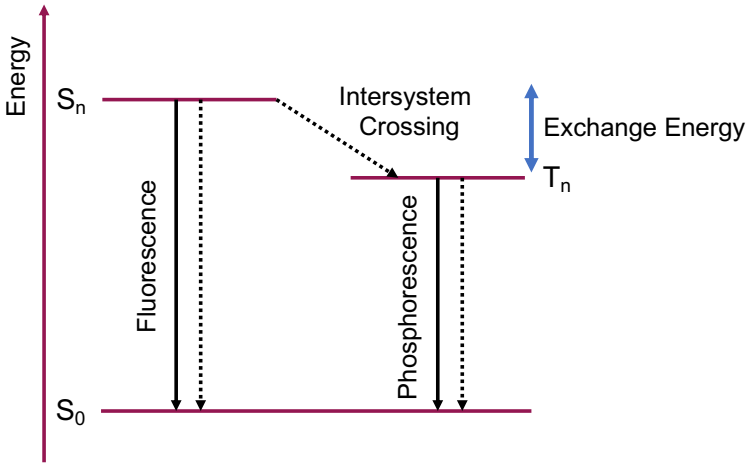


Figure 2.6: Singlet and triplet states in a state diagram. Solid and dotted lines stand for radiative and nonradiative decay, respectively. Adapted from [7].

that transitions between different spin states are forbidden and since the ground state is a singlet, transitions between the ground state and triplet excited states are spin-forbidden. Nevertheless, emission from triplet states, T_n, is observed and the luminescence resulting from $T_n \rightarrow S_0$ transitions is termed *phosphorescence* to differentiate it from luminescence arising from transitions between singlet states, $S_n \rightarrow S_0$, which is called *fluorescence* (figure 2.6).

For spin-forbidden phosphorescence emission to occur there needs to be some perturbation effect which can cause the triplet state to obtain some singlet state contribution and vice versa. This perturbation is called *spin-orbit coupling*. It results from the fact that only the total angular momentum $j = l + s$ has to be conserved in an optical transition. Thus, a change in the spin angular momentum, s, of a molecule could be compensated by a corresponding change in the orbital angular momentum, l [8]. In this formalism a flip in the spin of an electron can occur if it is accompanied by a change in the associated angular momentum from l_x to l_y. Such a change in angular momentum can be provided by vibrations within the molecule and is termed *vibrationally induced spin-orbit coupling* [18]. In conjugated polymers such vibrational perturbations are rarely observed which makes the study

of phosphorescence from these materials very difficult.

The perturbation can also be provided by the orbital motion of electrons. Spin-orbit coupling is essentially a magnetic torque that is able to either flip or rephase the spin magnetic dipole vector of a single electron. In molecules, the strongest magnetic torques are provided by the orbital motion of electrons. The accelerating force is proportional to the charge of the nucleus with the highest atomic number that influences the orbit of the electron [14]. Hence, this mechanism is most effective for materials containing heavy atoms and is termed *heavy atom induced spin-orbit coupling* [7].

In conclusion, optical generation of triplet states is spin-forbidden. However, triplet emission can become partially allowed if a perturbation such as spin-orbit coupling mixes nearby singlet and triplet states resulting in *intersystem crossing* of singlet excitons to the triplet manifold. Lastly, as radiative transitions from the triplet excited state to the singlet ground state are spin-forbidden, the lifetime of the triplet is much longer in comparison to the singlet.

2.7 Electroluminescence

Since optical transitions between the singlet ground state and the triplet excited state are forbidden, optical excitations initially create only singlet excited states. Subsequently some triplets can be formed by intersystem crossing. In contrast to optical excitations, electrical excitations can form both singlet and triplet excitons. In a light emitting diode (LED), electrons and holes are injected from opposite electrodes, they move through the semiconductor film until as a result of their coulomb attraction they recombine and form either a singlet or triplet state. Since there are three triplet substates and only one singlet state, triplets should be formed with a 75% probability in comparison to a 25% probability for singlet states. This ratio has been observed for small molecules, for example, a singlet generation fraction

of $22 \pm 3\%$ has been reported for Alq_3 [19], however, much higher singlet generation has been measured in conjugated polymers. For poly(9,9-dioctylfluorene) singlet generation fractions of over 50% have been reported [20, 21]. Proposed explanations for this deviation from the statistical value are spin-dependent recombination [22] and triplet-triplet annihilation (TTA) [23]. In TTA two triplets collide leading to the formation of one excited singlet state and one ground state singlet. Finally, since in conjugated polymers only singlet states decay with a high radiative rate, triplet state formation places a limit on the efficiency of LEDs.

2.8 Nonradiative Transitions

The radiative decay of an excited state competes with nonradiative transitions. A nonradiative transition that takes place between states of the same spin (e.g. $S_2 \rightarrow S_1, T_2 \rightarrow T_1$) is called *internal conversion* while a transition taking place between states of different spin (e.g. $S_1 \rightarrow T_1, T_1 \rightarrow S_0$) is referred to as *intersystem crossing* and it requires spin-orbit coupling. Nonradiative transitions emit phonons instead of photons which is why they are favoured when there is only a small energy gap to be bridged. It is important to distinguish nonradiative transitions between two different electronic states from thermal relaxation within a single electronic state.

The relationship between the nonradiative transition rate, k_{nr}, and the energy difference between the initial and final states, ΔE, is called the *energy gap law* and it is expressed as

$$k_{nr} \propto \exp\left(-\gamma \frac{\Delta E}{\hbar \omega_M}\right), \tag{2.4}$$

with $\hbar\omega_M$ being the vibrational quanta of the highest frequency mode and γ a term that can be expressed through molecular parameters [24–26]. The energy gap law specifies that there is an exponential dependence between the transition rate and the energy difference between the two states [27]. This is why intersystem crossing rates

from S_1, for example, into higher triplet states, T_n, are often faster due to smaller energy gaps. The mechanism of nonradiative decay associated with the energy gap law is multiphonon emission through the vibration of bonds on the conjugated polymer. An important consequence of the energy gap law is that emission always occurs from the lowest excited state of a spin manifold. This phenomenon is known as *Kasha's rule*. It results from the fact that internal conversion of $S_2 \rightarrow S_1$ and $T_2 \rightarrow T_1$ is fast in comparison to radiative decay of $S_2 \rightarrow S_0$ and $T_2 \rightarrow S_0$ due to the small $S_2 - S_1$ and $T_2 - T_1$ energy gaps. Finally, the energy gap law is one of the causes for low phosphorescence emission. Nonradiative decay competes with the radiative decay for $T_1 \rightarrow S_0$ transitions due to the lower energy of the triplet state while internal conversion in the case of $S_1 \rightarrow S_0$ transitions is negligible because of the higher energy of the first excited singlet S_1.

2.9 Energy Transfer in Conjugated Polymers

During its lifetime an excitation can be transferred from one molecule, the energy donor D, to another, the energy acceptor A. This energy transfer can occur radiatively by emission and *reabsorption* of light or nonradiatively by quantum chemical coupling. Radiative transfer can be expressed as

$$D^* \rightarrow D + h\nu, \tag{2.5}$$

$$h\nu + A \rightarrow A^*. \tag{2.6}$$

This can only take place if the emission spectrum of the donor and the absorption spectrum of the acceptor sufficiently overlap. When D and A are identical molecules the strongest overlap is found between the absorption spectrum and the first fluorescence mode leading to a low first vibronic and a relatively high second vibronic peak for polymer films where the light path is long (usually several hundred nanometers).

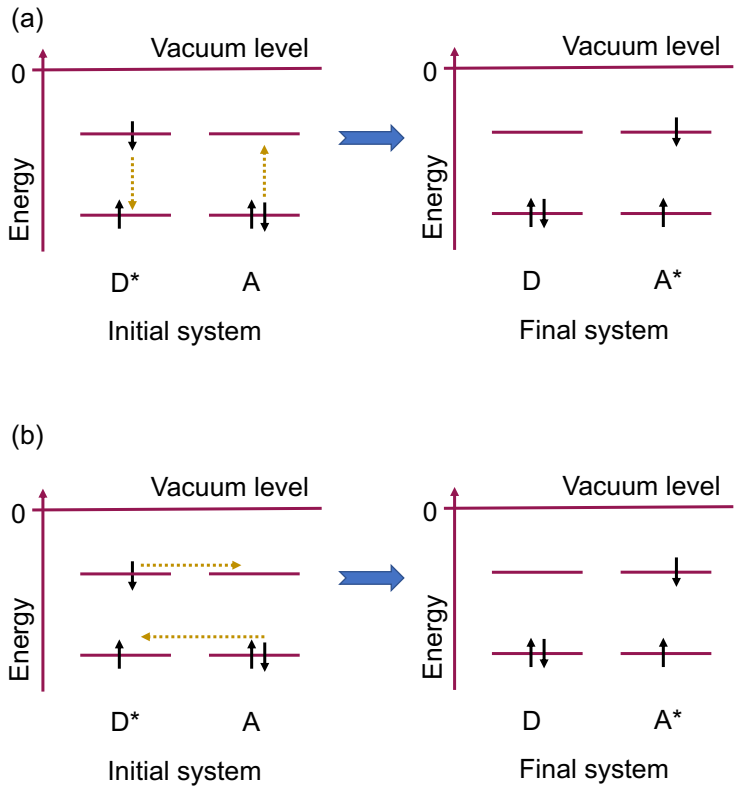


Figure 2.7: Illustration of energy transfer (a) by coulomb coupling (Förster energy transfer) and (b) by exchange coupling (Dexter energy transfer). After reference [7].

The other energy transfer mechanism via quantum chemical coupling differs from reabsorption in that it is a one step process where the deexcitation of the donor and the excitation of the acceptor occur simultaneously,

$$D^* + A \rightarrow D + A^*. \tag{2.7}$$

Depending on the mode of coupling two types of transfer are distinguished: *Förster transfer* [28] where the coupling is provided by electromagnetic dipole-dipole interaction and *Dexter transfer* [29] where the coupling is of an exchange type. Förster energy transfer is based on the transfer of energy between two dipoles. The donor oscillates at its resonant frequency and transfers the energy of this oscillation to an acceptor molecule of similar resonant frequency (figure 2.7 (a)). The resonant frequencies of the donor and acceptor are quantified by their emission and absorption spectra. Therefore, for Förster transfer to take place the emission of the donor needs to overlap with the absorption of the acceptor. Additionally, the

dipole orientations are of importance since it has been proven that energy transfer does not take place between perpendicular dipoles [7]. Finally, the range of Förster transfer is quantified by the Förster radius which is defined as the distance at which energy transfer to an acceptor and decay of the excited donor have equal probability. Förster transfer allows singlet excitons to move within a polymer, however, it cannot occur for triplet excitations since triplet decay to the ground state is spin-forbidden [28].

The Förster theory was extended by Dexter [29] to allow for forbidden transitions such as those for triplets. In Dexter transfer the coupling is provided by an exchange interaction where electronic orbitals are close enough to overlap. The requirement for orbital overlap means that Dexter transfer can only occur over relatively short distances. For spin to be conserved it is necessary that the two electrons are exchanged between the orbitals as illustrated in figure 2.7 (b).

2.9.1 Triplet-Triplet Annihilation

Dexter transfer is the mechanism by which triplet migration occurs. The process of triplet migration becomes important when there is a high triplet concentration such as in electroluminescence devices where triplets can be formed directly as a result of charge carrier recombination. When triplet excitons are mobile they can interact bimolecularly. If two triplets collide they can annihilate. This phenomenon is called triplet-triplet annihilation (TTA). In TTA, the total spin angular momentum has to be conserved. Therefore, depending on the spins of the interacting triplets, three cases can occur as follows:

$$T_1 + T_1 \rightarrow S_1 + S_0 + heat, \tag{2.8}$$

$$T_1 + T_1 \rightarrow T_1 + S_0 + heat, \tag{2.9}$$

$$T_1 + T_1 \rightarrow Q_1 + S_0 + heat. \tag{2.10}$$

If the two triplets have opposite spin their total spin angular momentum would be zero and the process in 2.8 would take place resulting in delayed fluorescence. If the two spins add up to 1, case 2.9 would happen and lead to the nonradiative quenching of one of the triplets. In theory, a state of spin 2 called a quintet can be formed (2.10), however, it is not observed. As a result of TTA, one or both triplets are lost, therefore, it is an important triplet quenching mechanism.

2.10 Aggregation and Quenching

Emission from aggregate species can constitute a major contribution in the spectra of polymer films. Aggregate formation occurs when conjugated segments are close together and interact forming a weak bond. When the interaction is moderate and the two interacting units are identical the aggregate is called a *dimer* [9]. Dimers possess both an absorption and an emission spectrum as the attractive force between the two units does not cause significant changes in the intermolecular distance or orientation. Sandwich and herringbone arrangements of molecules favour dimer formation. An *excimer* is formed when the interaction is strong enough to cause the two units to reorient themselves in order to optimise their interaction [7]. Excimers are characterised by structureless strongly red shifted emission. No absorption contribution is observed for excimers since the interaction causes significant changes in the intermolecular distance leading to absorption taking place at a configuration coordinate where the interaction effect is not noticeable. Therefore, the excimer absorption coincides with the non-interacting chromophore absorption. Excimers are common for flat, disc-shaped or elongated chromophores. An excimer formed between two dissimilar molecules is termed an *exciplex*. Aggregates act as structural traps and emit at the cost of single chromophore polymer luminescence.

Quenching is defined as any process that decreases the emission of a sample. Quenching is usually caused by an unwanted energy transfer process such as a transfer to a nonradiatively decaying state. Both singlet and triplet emission can

be quenched. Common quenchers for singlets in polyfluorene are keto defects in the polymer backbone which are formed by photo- or electro-oxidation and can also be introduced during synthesis [30–32]. A major triplet quencher is oxygen. Molecular oxygen has a triplet ground state and its next higher excited states are two singlets with energies of 0.98 eV and 1.63 eV above the ground state [7]. Therefore, when a chromophore molecule in an excited triplet state, ${}^3M^*$, is next to an oxygen molecule in the triplet ground state, ${}^3O_2$, energy transfer can result in the promotion of the oxygen molecule to an excited singlet state, ${}^1{O_2}^*$, and the transition of the chromophore molecule to the ground state, ${}^1M$, so that phosphorescence is no longer observed (${}^3M^* + {}^3O_2 = {}^1M + {}^1{O_2}^*$) [7]. Since the energy level of singlet oxygen is only 0.98 eV, it is able to quench the phosphorescence of most organic semiconductors [33]. Additionally, singlet oxygen is chemically reactive and can damage the π-bonds in organic semiconductors. This may lead to reduced luminescence efficiency of a material as well as shorter lifetime of LEDs made with it.

2.11 Charge Transport

Charge transport is an important attribute of organic semiconductors and is critical for device applications. A key parameter that describes the motion of charge carriers in a material is their *mobility*, μ. It is defined as the drift velocity, v, per unit electric field, E,

$$\mu = \frac{v}{E}. \tag{2.11}$$

Mobility is typically specified in units of $\mathrm{cm^2V^{-1}s^{-1}}$. It should be clarified that the drift velocity does not need to be proportional to the electric field and the mobility is, indeed, often dependent on the electric field. This leads to mobility not being a purely material dependent property as it can also depend on the charge density at which an experiment is performed.

Charge transport is governed by the transfer of an electron from the LUMO of a donor site to the empty LUMO of an electron accepting site. Equivalently, a hole can be transferred at the HOMO level. In the limit of strong electronic coupling between the sites, an electron (or a hole) would move coherently within a band of states constructed from the LUMO (or HOMO) orbitals of the molecules involved. Under an applied electric field the charge carrier would move with a constant mobility due to scattering at the band edge. This is the case for a perfectly ordered crystal at $T = 0\,\mathrm{K}$. The band model is no longer applicable when structural irregularities and lattice vibrations begin to strongly affect charge transport. In the limit when a charge carrier is scattered at each site, a transition from band transport to a hopping motion takes place. Therefore, transport is controlled by (i) the electronic coupling among the constituent molecular units, (ii) the coupling to intra-molecular as well as inter-molecular vibrations (polaronic effects) and (iii) the static intra- as well as inter-molecular disorder [7]. Different transport models have been established depending on which coupling mechanism dominates such as *band transport*, *polaronic transport* and *disorder-controlled transport*.

2.11.1 Band Transport

In rigid, highly ordered systems where the electronic coupling between nearest neighbour sites dominates over polaronic and disorder effects, band transport takes place. A charge is delocalised and forms a propagating Bloch wave that can be scattered by lattice vibrations as illustrated in figure 2.8 (a). High purity molecular crystals of naphthalene have been shown to exhibit band transport at low temperatures [34, 35]. Due to the weak van der Waals intermolecular forces and disordered structures characteristic for organic semiconductors, band transport is rarely observed. In organic materials transport is better described by a hopping mechanism.

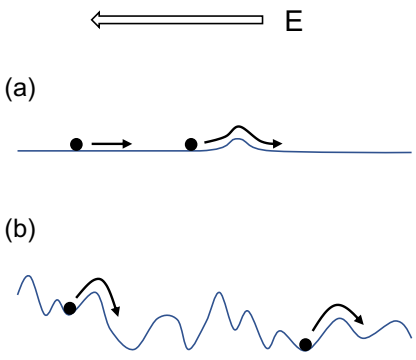


Figure 2.8: Illustration of (a) band transport and (b) hopping transport under an applied electric field, E. In ordered materials, charges travel within energy bands and are scattered by phonons (depicted as a bump). In disordered materials, charges are localised to individual sites due to polaronic and disorder effects and transport proceeds by hopping. After reference [36].

2.11.2 Hopping Transport

If polaronic and disorder effects become significant compared to the electronic coupling between nearest neighbour sites, the transport band is destroyed and transport becomes incoherent. In this case, charge carriers are localized at individual sites and transport occurs by a series of non-coherent transfer events termed *hopping* (figure 2.8 (b)). Hopping transport takes place once there is too much geometric relaxation when a charge carrier is placed on a molecule, too much vibration or too much variation in inter-site distance or site energy.

2.11.2.1 Polaronic Transport

Polaronic transport occurs when effects due to intra-molecular or inter-molecular vibrations become significant. They introduce dynamic disorder since they are based on coupling of electronic excitations to vibrations. Consequently, a charge carrier is localised at a site due to this dynamic disorder. The charge forms a polaron as a result of coupling to surrounding molecules since inter-molecular displacements and polarization effects modify the van der Waals interactions between molecules. Transport takes place via inter-site polaron hopping. Since the charge

transfer is accompanied by a distortion of the molecule and its environment a reorganization energy, λ, is required and the process is thermally activated [9]. A Marcus type equation has been derived for polaronic hopping by Holstein [37]. It yields a hopping rate

$$k_{ET} = \frac{J^2}{\hbar}\sqrt{\frac{\pi}{2E_{pol}kT}}\exp\left(-\frac{E_{pol}}{2kT}\right), \tag{2.12}$$

where J is the transfer integral, E_{pol} is the polaron binding energy which has been shown to be half of the reorganization energy [7], k is the Boltzmann constant, $\hbar$ is the reduced Planck constant and T is temperature. For polaronic transport between identical molecules, the hopping rate is symmetric (forward and backward jumps require the same amount of energy) as sites are isoenergetic and have the same polaronic binding energy. Nevertheless, for increasing static disorder this model no longer accurately describes charge transport and a different approach is necessary.

2.11.2.2 Disorder-Controlled Transport

For disordered materials such as conjugated polymers a different model based on energetic and spatial disorder has been shown to be more successful. This method is called the *Gaussian Disorder Model (GDM)* and has been developed by Bässler [38]. Here, charges are localized at sites due to static disorder and the effects due to electron-phonon coupling are considered insignificant. Contrary to the symmetric polaron hopping rate, in the case of disorder-controlled hopping, forward and backward jumps require different amounts of energy. If a forward jump is uphill in energy, the backward jump would be downhill. This is described by a Miller-Abrahams (MA) hopping rate [39]

$$k_{ij} = \nu_0 \exp\left(-2\gamma r_{ij}\right) \times \begin{cases} \exp\left(-\frac{\varepsilon_j - \varepsilon_i}{kT}\right), & \varepsilon_j > \varepsilon_i \\ 1, & \varepsilon_j \leq \varepsilon_i \end{cases} \tag{2.13}$$

where r_{ij} is the jump distance between sites i and j, ν_0 is the attempt-to-hop frequency and ε_i and ε_j are the energies of site i and j, respectively. γ is the inverse localization radius of the electron wavefunction and it is associated with the

electronic coupling matrix element between adjacent sites [7]. In this model excess energy is released for a downhill jump while an uphill jump requires activation energy in the form of a Boltzmann factor. The MA rate assumes the Boltzmann factor is equal to 1 for a downhill jump and that there is always an energy accepting phonon available to dissipate the excess energy.

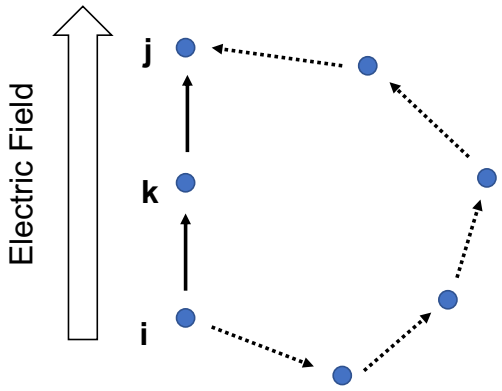


Figure 2.9: Depiction of the possible routes for a hole to travel from an initial state i to a final state j separated by an intermediate high-energy site k. The direct route (solid arrows) via site k can be avoided by a detour (dotted arrows) over energetically more favourable sites. This detour includes jumps against the direction of the electric field which can become blocked at high fields. After reference [7].

The hopping mobility μ of a charge depends on the applied electric field since the field lowers the activation energy for a jump in the field direction (figure 2.9). Experimentally, it has been shown that for amourphous organic semiconductors μ obeys a *Poole-Frenkel type field dependence*, $\ln(\mu) \propto \sqrt{E}$. This behaviour has been reproduced using simulations based on the *Correlated Disorder Model (CDM)*. The CDM extends the GDM by the incorporation of site energy correlation which is expected in real world samples [40, 41].

Depending on the organic semiconductor material under study and its morphology, both polaron and disorder effects can contribute to charge transport. Therefore, a combination of both may be required to fully describe the motion of charges [42].

2.12 Charge Trapping

Trapping effects frequently impede charge transport. When traps are present, a charge carrier that hops from molecule to molecule might end up captured by a trap. Its subsequent release would require an activation energy, therefore, this process slows down transport. Trapping sites can be structural defects, deliberate or inadvertent dopant molecules or aggregates. Since the electronic coupling in an aggregate is enhanced compared to a monomeric molecular structure it is possible that aggregate sites can act as charge carrier traps when they form intraband energy states. For hole trapping, the trap depth is calculated from the difference between the ionization potentials of the trap and host material. The same applies for electron trapping where the difference between the electron affinities of the materials is important. Subsequently, the higher the ionization potential of the host material, the more likely it is that inadvertent dopants can act as charge traps.

2.13 Poly(9,9-dioctylfluorene) Homopolymer

Polyfluorenes are a family of conjugated polymers based on a *fluorene* repeat unit with one of the most well studied examples being poly(9,9-dioctylfluorene) (PFO). PFO is a dialkyl-substituted polyfluorene with alkyl side chains attached to the 9-position of the fluorene (figure 2.10). It has been investigated extensively due to its blue emission, high charge carrier mobility, high optical gain and good thermal stability [43–46].

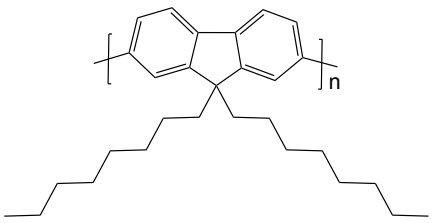


Figure 2.10: Chemical structure of poly(9,9-dioctylfluorene) (PFO).

The fluorene unit is made up of two para-linked phenylene rings that are bridged by the carbon atom in the 9-position, thus, making it quite rigid. However, neighbouring fluorene units are only linked by a single C-C bond that allows for considerable rotational freedom within the chain [11]. This leads to PFO's morphological diversity and enables it to adopt different chain conformations.

PFO's favourable optoelectronic properties together with its morphological diversity make it a good model system for the modifications studied in this thesis. It is a widely researched homopolymer against which copolymers incorporating different functional moieties can be compared enabling the study of structure-property relationships, including the influence of chain conformation on photophysical and optoelectronic properties.

2.13.1 Conformation

Chain conformation can strongly affect the optoelectronic properties of conjugated polymers. As the electronic wavefunctions are primarily localized on individual chains, the conformation influences the electronic coupling along the chain. Solid-state PFO can adopt *glassy* and *β phase* chain conformations characterised by different torsion angles between the constituent molecular units (figure 2.11). PFO also supports a *crystalline packing arrangement*.

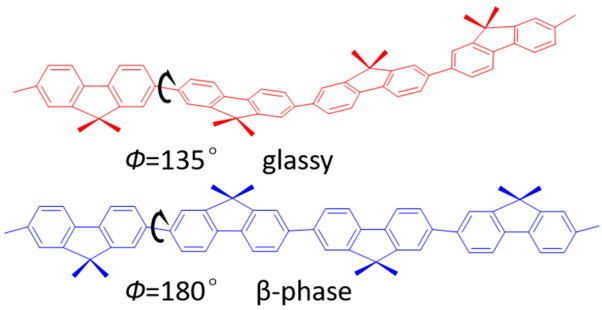


Figure 2.11: The difference in intermonomer torsion angle, ϕ, between the glassy and β phases of PFO. The n-octyl side chains of PFO (C_8H_{17}) are omitted for clarity. Image by Zhang *et al.* [47] licensed under CC BY 4.0.

2.13.1.1 Glassy Phase

The glassy phase is a disordered phase with a broad distribution of intermonomer torsion angles centered around $\phi \sim 135°$ [48]. Glassy phase films are obtained when sufficiently rapid solvent evaporation occurs during film deposition. This can be done by spin coating from good solvents with low boiling points [49] such as tetrahydrofuran (THF) and chloroform. Glassy films can also be obtained using higher boiling point solvents such as toluene when solution and substrate are both heated prior to spin coating to ensure fast solvent escape from the film [46]. Finally, glassy films can be prepared by rapidly cooling samples from the nematic and isotropic melts [50, 51].

2.13.1.2 β Phase

The β phase conformation is an ordered chain-extended geometry with a torsion angle of $\phi = 180°$ between adjacent monomer units leading to their coplanar orientation with the octyl side chains positioned on alternating sides of the backbone [48, 52, 53]. The β phase is induced by either a postdeposition treatment including exposure to solvents in liquid [43, 54] or vapour [55, 56] form, or by slowing down the kinetics of film formation using poor or high boiling point solvents/additives [49, 57]. The formation of the β phase is proposed to be a result of mechanical or thermodynamic stress [3, 52, 58]. The elongated chain geometry has been suggested to reduce overall stress by minimising intra-chain steric interactions [11]. For simplicity, we will adopt the convention that samples that contain a fraction of β phase chains in a mostly glassy PFO sample irrespective of the exact amount will be called β phase.

2.13.1.3 Crystalline Packing Arrangement

Crystalline PFO has a more extended chain geometry with an intemonomer torsion angle $\phi \sim 150°$ [48, 59]. Crystalline PFO is formed by slow cooling from the nematic melt and results in films with increased haze due to light scattering from

the crystallites. The crystalline packing arrangement can also be generated from the glassy phase by heating samples past the crystallisation temperature [42, 60, 61].

2.13.2 Optical Spectroscopy

The different chain conformations of PFO can be readily identified by specific signatures in their optical spectra. The work in this thesis is only concerned with the disordered glassy phase and the ordered β phase so from now on we will concentrate on them. Their absorption and photoluminescence (PL) spectra are presented in figure 2.12.

Due to its disordered chain geometry, the glassy phase has an inhomogeneously broadened absorption spectrum with a peak located at $\sim 381\,\text{nm}$ (3.25 eV) while the PL spectrum is characterised by vibronic peaks at 422, 447 and 476 nm (2.94, 2.77 and 2.60 eV). The presence of a fraction of β phase chains is identified by the appearance of a new red shifted $S_1 \rightarrow S_0$ 0-0 absorption peak. This has been reported to lie from 430 nm (2.89 eV) to 436 nm (2.84 eV) with increasing β phase fraction [57, 63]. The PL spectrum has a pronounced vibronic structure with peaks at 436, 464 and 498 nm (2.84, 2.67 and 2.49 eV). Additionally, the β phase has a reduced Stokes shift between its absorption and emission spectra. The good intermixing of the glassy and β phases and the large spectral overlap between the emission of the glassy phase and the absorption of the β phase lead to efficient picosecond transfer of excitations to the lower energy β phase chains [5]. This explains why the β phase dominates the emission even from films that contain only a small fraction of planarized chains [49]. In absorption, it appears as a minor constituent since there all chain conformations are sampled simultaneously and differences in fraction of chains in the two phases are more apparent.

Also, the PL spectra show a decrease in the Huang-Rhys parameter (the magnitude of the 0-0 vibronic peak increases relative to the 0-1 and 0-2 vibronics)

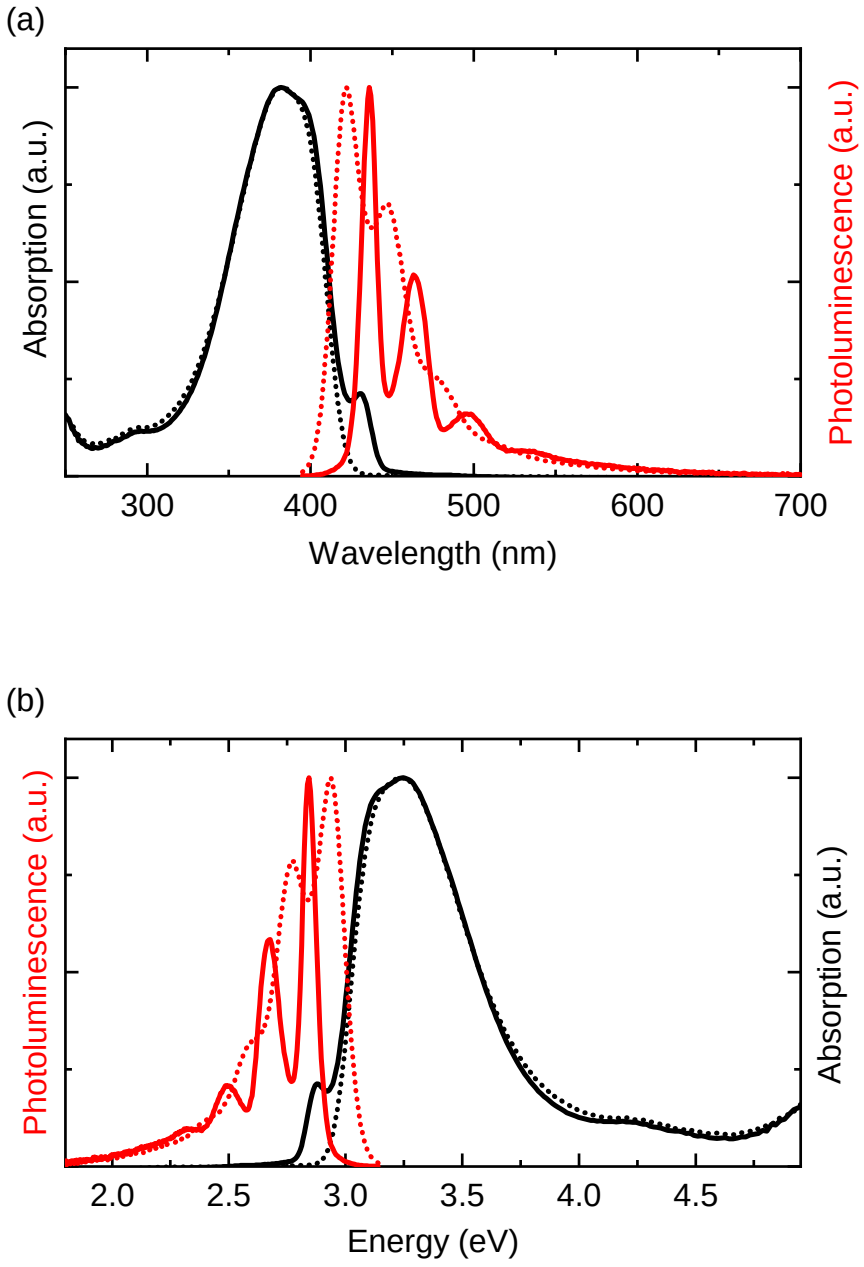


Figure 2.12: Peak normalized absorption (black) and peak normalized PL (red) of PFO thin films in the glassy phase (dotted line) and the β phase (solid line). The spectra are presented as a function of wavelength in (a) and energy in (b). The PL spectra are converted to an energy scale using the Jacobian transformation [62].

for the planar chains compared to the nonplanar ones. This is in agreement with a more delocalized exciton in the β phase supported by the red shifted absorption and emission spectra of the β phase relative to the glassy phase. X-ray fiber diffraction measurements of PFO have found that the correlation length in the chain direction (which is a measure of the intrachain order of a polymer) is much longer (22 nm) for the β phase compared to the glassy phase (8 nm) [58, 64]. In the glassy phase topological defects disrupt the π-conjugation. As repeat units in a polymer chain are linked by covalent π-bonds, the electronic coupling between neighbouring units depends on any torsional angles between them. The highest coupling corresponds to a planar arrangement and the poorest to a 90° bend. The low Huang-Rhys parameter for the β phase also indicates that there is minimal geometric rearrangement related to the $S_1 \rightarrow S_0$ transition, hence, both the ground and excited states have planar chain geometries [65].

PFO samples with a fraction of β phase chains have been shown to present a number of improvements in optoelectronic performance compared to purely glassy samples. For example, polymer light emitting diodes (PLEDs) based on a PFO active layer have been enhanced by introducing a small fraction of β phase chains. The β phase containing PLEDs displayed a $\sim 300\%$ increase in external quantum efficiency and improved color purity (external quantum efficiency 3.33% with CIE color coordinates $x + y < 0.3$) [43]. Moreover, β phase PFO dispersed in an inert poly(methyl methacrylate) (PMMA) matrix shows enhanced optical gain properties compared to neat glassy PFO as a result of increased magnitude of stimulated emission and a broader wavelength range over which optical gain occurs [66]. Ultrafast optical gain switching (~ 300 GHz) in the stimulated emission region has been reported for such blends of β phase PFO and PMMA [66]. Finally, the substantial refractive index difference between the glassy and β phases of PFO has demonstrated potential for the fabrication of conformational-metamaterial based photonic elements. A range of photonic structures could be made by simultaneous structuring and spatial patterning of the β phase chain conformation in thin film

glassy PFO via local dip-pen nanolithography using selected solvent inks [46].

2.14 Copolymers

A polymer is a compound that consists of a sequence of repeat units covalently bound together. A *homopolymer* is formed when all the repeat units are identical while a *copolymer* results from the joining of different monomer units. The three main types of copolymers are *random*, *block* and *alternating*. In an alternating copolymer the repeat units regularly alternate in contrast to a random (statistical) copolymer where the sequential distribution of the monomers obeys known statistical laws [67]. Finally, a block copolymer is defined as containing alternating segments of different polymer composition (blocks) linked together [68]. Homopolymers and copolymers are most commonly synthesised through either Yamamoto [69] or Suzuki coupling [70]. While Yamamoto coupling can only produce homopolymers or random copolymers, Suzuki coupling is able to form alternating copolymers as it uses two differently functionalized monomers.

Linking two or more monomer units into a copolymer offers the advantage of combining and adjusting the properties of the resulting compound. One very common type of copolymer is the donor-acceptor type copolymer where an electron-withdrawing and an electron-donating moieties are combined. As a result of the different electronegativities of the two units there is partial charge transfer. The HOMO of the pair is primarily localized on the donor while the LUMO on the acceptor [7]. The strong CT character results in a small overlap between the HOMO and LUMO and, therefore, a decrease in the electronic exchange energy. Consequently, the small energy gap between the singlet and triplet states allows for an efficient thermally activated reverse intersystem crossing rate that allows upconversion of triplet states to the emissive singlet level [71]. Such materials are known as *thermally activated delayed fluorescence emitters*. Furthermore, donor-acceptor copolymers are often employed in solar cell devices due to their red shifted

absorption spectra compared to the spectra of the individual constituents. The optical gap is reduced as a result of the resonance interaction between the frontier orbitals of the donor and acceptor moieties as well as the charge transfer interaction. This leads to a better match to the Sun's emission spectrum and, therefore, more efficient photovoltaic devices.

3
Experimental Methods

3.1 Optical Spectroscopy

Optical spectra throughout this thesis are presented as a function of wavelength or energy. The selection was determined by the convention adopted in referenced literature. The conversion of photoluminescence spectra from wavelength to energy units was done using the Jacobian transformation [62].

3.1.1 Films for Spectroscopic Measurements

All polymers were readily dissolved in toluene (anhydrous, 99.8%, Sigma-Aldrich). Solutions were prepared in a dry nitrogen glovebox and left to stir at room temperature for 12 hours. The solution concentrations used were $10 - 15\,\mathrm{mg\,ml^{-1}}$ depending on the material. The PFO used throughout this thesis was supplied by 1-Material Inc. (weight-average molecular weight, $M_w = 55 \times 10^3\,\mathrm{g\,mol^{-1}}$, polydispersity index, $PDI = 2.5$). For spectroscopic measurements thin films were spin coated on square quartz substrates ($15 \times 15\,\mathrm{mm}$). The substrates were cleaned for 10 minutes each in a sequence of ultrasonic baths using acetone and isopropyl alcohol. Then they were blown dry with nitrogen gas and subjected to a 10 minute UV ozone treatment. All films were processed in ambient atmosphere

inside a fumehood unless the polymers were air sensitive as are the materials studied in chapter 6 in which case the fabrication process took place inside a dry nitrogen glovebox. Typically 100 µl of solution was measured with a micropipette and dropped onto the substrate, then it was spun at a speed of 2000 rpm to form ~ 70 nm films. The back sides of the substrates were cleaned after spin coating to remove any material that may have adhered to them during deposition. The film thickness was measured using a Dektak surface profiler.

For polymers capable to adopt glassy phase and β phase chain segments, additional processing parameters were necessary to control the film conformation. For the fabrication of glassy phase films both solutions and substrates were placed on a hot plate at 100 °C for 5 minutes immediately before spin coating. Such samples are referred to as *hot spun* in the text. For fabricating β phase containing films postdeposition swelling of the glassy films was employed. This was done by exposing the hot spun glassy films to toluene vapour at room temperature for 12 hours. The swelling induced by the solvent vapour causes a mechanical stress which leads to the planarisation of a fraction of the polymer chains [49, 55, 56]. These films are called *solvent vapour annealed (SVA)* in the text.

3.1.2 Absorption

Optical absorption spectra were measured with a Perkin-Elmer Lambda 1050 UV/Vis/NIR Spectrophotometer equipped with a Perkin-Elmer 100 mm integrating sphere accessory. In the spectrophotometer, the light from the source is directed into a monochromator which disperses it to separate the different wavelengths. A slit at the exit determines which narrow range of wavelengths passes through. Then the beam is split into two identical components, a sample beam and a reference beam. The integrating sphere has three ports: a sample beam entrance port (transmittance port), a reference beam entrance port and a sample reflectance port. This is illustrated schematically in figure 3.1.

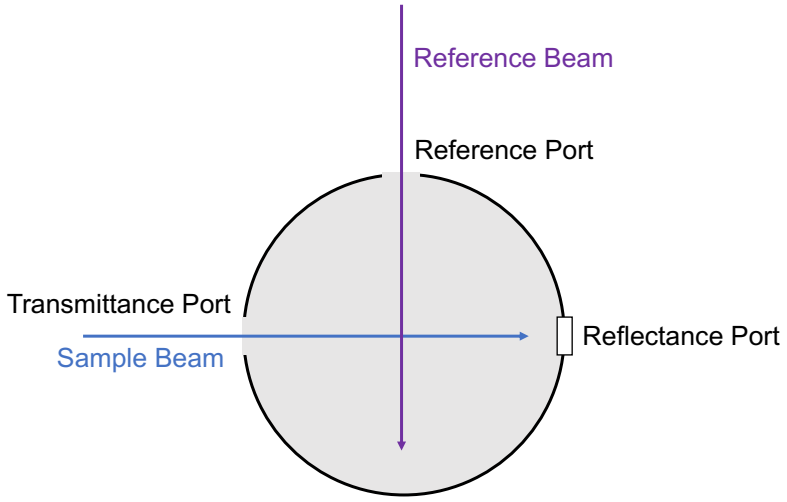


Figure 3.1: Schematic illustration of double beam absorption measurements with integrating sphere.

For transmission measurements, the sample of interest is placed at the transmittance port while a spectralon standard is located at the reflectance port. A baseline scan is performed at the beginning without a sample. The percentage transmission, T, is calculated as the ratio of the light transmitted through the sample with respect to the baseline. The reference beam is used to take into account fluctuations of the source. For reflection measurements, the transmittance port is left empty and a baseline scan is taken with the spectralon standard at the reflectance port. Then the spectralon standard is replaced by the samples for measurements. The percentage reflection, R, is computed as the ratio of the light reflected from the sample with respect to the baseline. The reference beam is used to avoid *substitution error*. This error arises because when a sample is placed at the reflectance port the total internal reflectivity of the sphere drops. This can cause samples to appear less reflective than they are as the energy throughput of the sphere is reduced. In a double beam configuration, the reference beam reflects off the sphere wall and reference reflectivity data can be obtained with the sample in place. The absorption, A, is then calculated from the measured transmission, T, and reflection, R, as follows

$$A = 100\% - (T + R). \tag{3.1}$$

3.1.3 Photoluminescence

Photoluminescence spectra were recorded in reflection geometry with a Jobin Yvon Fluoromax-3 spectrofluorometer. The Fluoromax-3 uses a continuous xenon light source which shines on an excitation monochromator. There the specified excitation wavelength light is picked out and directed onto the sample causing it to fluoresce. The sample fluorescence is sent to a second emission monochromator which selects wavelengths and shines them onto a photomultiplier tube detector. Finally, the signal read from the detector is displayed on a computer. In the spetrofluorometer a beam splitter takes $\sim 8\%$ of the excitation light to a reference photodiode. This signal is used to correct for the wavelength and time response of the xenon lamp and monochromator. Both detectors have correction files run for them to account for the wavelength dependencies of the optical component.

3.1.4 Photoluminescence Quantum Efficiency

Thin film photoluminescence quantum efficiency (PLQE) was measured with a Jobin Yvon Fluoromax-3 spectrofluorometer equipped with a diffusely reflecting integrating sphere (barium sulfate inner coating). PLQE is defined as the number of emitted photons per number of absorbed photons. The PLQE measurements performed in this thesis were done using the method proposed by de Mello *et al.* [72]. This consists of a sequence of three measurements (figure 3.2).

First, a measurement of the empty integrating sphere is taken. The spectrum due to the scattered light is recorded. It shows an intense peak at the excitation wavelength. Next, the sample is placed inside the sphere and the light is directed to hit the sample. Now the detected spectrum consist of the scattered excitation light and the light emitted by the sample. The excitation peak intensity is reduced since a fraction of the laser light has been absorbed by the sample. A final measurement is required to correct for the fact that some of the excitation light is first reflected from the sample, then reflected from the walls of the integrating sphere and then

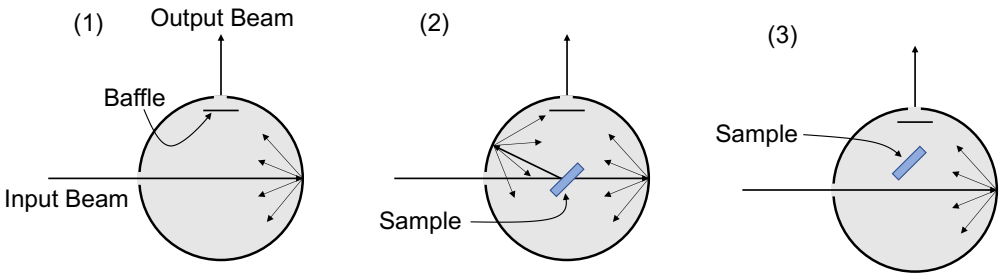


Figure 3.2: Illustration of the measurements performed to calculate PLQE. (1) The excitation is directed into an empty sphere in order to measure the photon flux at the excitation wavelength. (2) Next, the sample is placed inside the sphere and the light beam excites the sample directly. This gives the photon flux of the sample fluorescence and the flux of the incident laser photons decreased by the absorbed light photons. (3) Finally, a measurement with the sample in the sphere but outside the beam path is made to correct for absorption of scattered laser light. Adapted from de Mello *et al.* [72].

absorbed by the sample. To do this a third measurement is done where the sample is placed inside the sphere, however, the excitation light is directed to hit the integrating sphere wall and not the sample. The integrated area of the peaks at the excitation wavelength (L_1, L_2 and L_3 where the subscripts stand for the three measurements as indicated in figure 3.2) can be used to determine how much light was not absorbed by the sample in each measurement. While at longer wavelengths the sample fluorescence can give the amount of light emitted by the sample (the integrated areas under the fluorescence curves are P_2 and P_3). Then the PLQE, η, is calculated using the formula:

$$\eta = \frac{P_2 - (1 - A)P_3}{L_1 A}, \tag{3.2}$$

where A is defined as $A = 1 - (\frac{L_2}{L_3})$. For further details about the derivation of the PLQE formula please refer to [72].

3.1.5 Temperature Dependent Photoluminescence

Temperature dependent photoluminescence measurements of films were made using a micro-PL setup with the kind assistance of Claudius Kocher, DPhil student in the Department of Physics, University of Oxford. The samples were mounted on

xyz piezo positioners in a closed cycle AttoDRY800 cryostat and cooled down to 4 K under a pressure of around 10^{-6} mbar. For PL measurements, excitation was provided by a femtosecond Titanium-Sapphire laser Coherent Mira 900. The laser provides short pulses of about 100 fs at a repetition rate of 76 MHz. The repetition frequency was reduced using a Coherent Pulse Picker. Typical frequencies used were $0.76 - 3.8$ MHz. The excitation energy of 3.15 eV (394 nm) was obtained by second harmonic generation using an INRAD 5-050 Ultrafast Harmonic Generation System. A single mode optical fibre was used to route the excitation light to the micro-PL setup. The excitation power was adjusted using a neutral density filter. The light was focused onto a roughly 1 µm diameter spot on the sample by a Mitutoyo Apo objective (NA = 0.7, 100× magnification), which also collected the PL. A Semrock Di02-R405-25x36 dichroic mirror was placed in the emission path to reflect the excitation light and transmit the PL. A Semrock BLP01-405R-25 filter was also included to remove residual excitation light from the collection path. The emission spectra were recorded using an Andor spectrometer coupled to a thermoelectrically cooled iDus 420 charge coupled device (CCD). The spectral resolution was about 0.5 nm.

3.2 Electrical Characterisation

3.2.1 Dark Injection Transient Measurements

The Dark Injection Transient (DIT) experiment is a technique used to measure the mobility of charge carriers in a semiconductor. It involves the application of a long step voltage to the injecting contact of a semiconductor film sandwiched between an injecting and an injection blocking contact (figure 3.3 (a)). The transit of the leading front of injected carriers across the film under the applied field results in a time-dependent current (figure 3.3 (b)). The current response consists of an initial spike at the beginning of the voltage step due to the device capacitance (τ is related to the device RC response). This is followed by an increase in the current to a maximum value as the leading front of the charge carriers travels

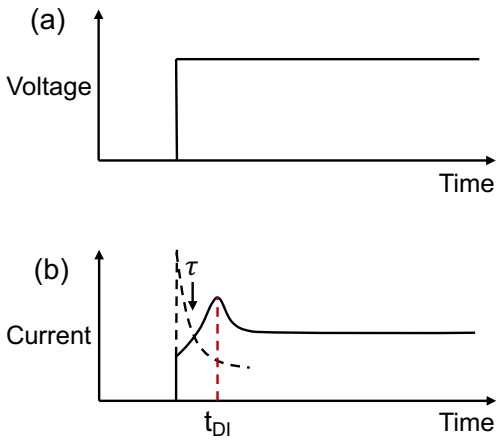


Figure 3.3: Schematic illustration of the dark injection transient (DIT) method, (a) a voltage step is applied to the injecting contact of sample consisting of a thin organic semiconductor sandwiched between an injecting and an injection blocking contact, (b) the dark injection transient in response to the applied voltage step. A time dependent current response is observed as described in the text.

through the organic semiconductor film. The leading front of space charge advances thought the film with time under the applied field. As the charges are transported through the film, the distance between the leading front and the counter electrode decreases and leads to an increase in the electric field. This results in a faster transit time, t_{DI}, compared to the space charge free transit time, t_{tr} ($t_{DI} = 0.787 t_{tr}$) [73]. Subsequently, the current density at the peak is slightly higher than the equilibrium space charge limited current (SCLC) density [74]. At longer times, the charge distribution reaches dynamic equilibrium and the SCLC density is reached. The arrival time of the first injected carriers at the counter electrode, t_{DI}, is related to the carrier mobility μ via the relation [73]

$$\mu = \frac{0.787 d^2}{V t_{DI}}, \tag{3.3}$$

where V is the voltage across the material and d is the material film thickness. The sign of the carriers studied depends on the choice of contacts.

DIT measurements were performed using the DIT function of PAIOS, a multi-measurement instrument for solar cell and OLED characterisation from Fluxim. All measurements were performed at room temperature and in ambient air. There was no evidence of sample degradation during the experiments.

3.2.1.1 Dark Injection Transient Device Fabrication

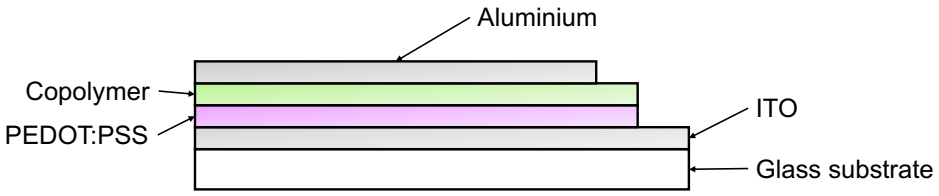


Figure 3.4: Cross section of the device structure of a hole-only copolymer DIT device.

Hole-only devices with the structure ITO/PEDOT:PSS/Copolymer/Al were fabricated for DIT measurements of hole mobility (figure 3.4). PEDOT:PSS was used as an interlayer to ensure only a moderate barrier for hole injection. Commercial ITO-coated glass substrates with a typical resistance of $20\,\Omega\,\square^{-1}$ were employed. The substrates were cleaned for 10 minutes each in a sequence of ultrasonic baths using acetone and isopropyl alcohol. Then they were blown dry with nitrogen gas and subjected to a 10 minute UV ozone treatment. Next, a 40 nm thickness film of PEDOT:PSS (Clevios P VP AI 4083) was deposited as a hole-injecting layer by spin coating at 3000 rpm and annealing in air for 20 minutes at 150 °C. The copolymers were spin coated on top of the PEDOT:PSS layer at 2000 rpm from toluene solutions ($10-60\,\mathrm{mg\,ml^{-1}}$). Spin coating was performed in ambient air inside a fumehood. In order to fabricate glassy films, both the solutions in toluene and the substrates were placed on a hot plate at 100 °C for 5 minutes immediately prior to spin coating. For fabrication of β phase containing films postdeposition swelling of the glassy films by toluene vapour annealing for 12 hours at room temperature was used. Aluminium electrodes of 70 nm thickness were then deposited through a shadow mask onto the

copolymer films yielding sandwich structures with an active area, defined by the electrode overlap, of 25 mm^2. The evaporation took place in a thermal evaporator in a nitrogen atmosphere glovebox at pressures lower than 10^{-6} mbar.

3.2.2 Air Photoemission Spectroscopy

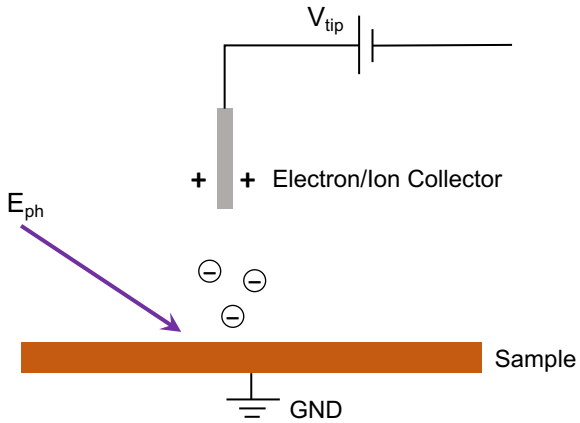


Figure 3.5: Air photoemission spectroscopy. The grounded sample is illuminated by a tunable UV light source of photon energy E_{ph}. Electrons are emitted at the sample surface where they interact with air molecules producing negative ions. The ions are collected by a positively biased tip (V_{tip}) above the sample. After reference [75].

Air photoemission spectroscopy (APS) is a method to determine the energies of molecular orbitals of organic semiconductors. APS employs the photoelectric effect by measuring the number of photoelectrons emitted from a sample illuminated by a tunable monochromatic UV light source. Photoelectrons are emitted from the surface when the photon energy is greater than the material's ionisation potential. Therefore, the ionisation potential is obtained by scanning the excitation photon energy and measuring the photoemission current. Most photoemission spectroscopy techniques involve measurements under vacuum since the electron mean free path under ambient pressure ($1 - 3\,\mu m$) is too short to reach the detector [76]. In APS, under ambient pressure electrons are stopped close to the sample surface forming a cloud of charge. Subsequently, this creates atmospheric ions such as N_2^-, O_2^- and OH^-. The information about the electron's kinetic energy is lost, however, the

electronic charge is conserved. These ions have much larger mean free paths than the electrons and can migrate to the detector tip if a +10 V potential is applied leading to measurable current (figure 3.5). Consequently, this allows an indirect measurement of the photoemission current.

It has been empirically shown that in most semiconductors the photoemission current increases with the cube of the photon energy above the ionisation potential [75–77]. Thus, a plot of the cube root of the photoemission current against photon energy forms a straight line which is extrapolated to the baseline signal to determine the ionisation potential of the semiconductor material.

Measurements were done using a KP Technology APS-04 instrument with the kind help of Saurav Limbu, PhD student in the Department of Physics, Imperial College London. The tip was held at an average height of 1 mm above the sample surface. The light illumination was provided by a monochromatic deuterium lamp source ($4 - 7$ eV) with a $4 - 5$ mm diameter light spot on the sample. The samples consisted of 100 nm polymer films deposited on ITO-coated glass substrates.

3.3 LED Characterisation

LEDs were characterised in a Newport Oriel Instruments integrating sphere using a purpose built sample holder with a printed circuit board which allowed each pixel of the LED to be addressed individually via a pin. The sample holder was connected to a Keithley 2636 sourcemeter controlled through a PC with a program written in LabVIEW by Dr Bernard Wenger. The sourcemeter applies a voltage to the chosen pixel and measures the corresponding current through the LED, while an Ocean Optics Maya2000 Pro spectrometer records the pixel brightness and electroluminescence spectra.

4

Arylamine Copolymerization

In this chapter the hole mobility of four fluorene-arylamine copolymers containing varying ratios of 9,9-dioctylfluorene and butyl-substituted phenylenediamine has been studied using the dark injection transient technique. The mobility of the fluorene homopolymer, PFO, is drastically reduced by the copolymerisation of 5% *of arylamine as a result of trapping at the arylamine sites. With increasing arylamine percentage the mobility rises due to the commencement of direct trap-to-trap transport that replaces the release of carriers back to the lower ionization potential fluorene transport sites as the dominant transport mechanism. This is supported by ambient pressure photoemission spectroscopy measurements showing two discrete energy levels corresponding to the two units, with the arylamine moiety's lower ionization potential acting as a hole trap. Transport in these organic copolymers is controlled over a large range by the copolymerisation of different amounts of a lower ionisation potential transporting moiety.*

4.1 Introduction

Charge carrier mobility is a key material parameter that determines device performance. Higher mobility can lead to more efficient charge extraction in solar cells, faster switching in FETs and higher space charge limited current in OLEDs. One

approach to tune material properties is through the copolymerisation of two or more monomer units in a single polymer chain. This way multiple functionalities can be combined without the unwanted phase separation common to blends. Copolymers of fluorene with a variety of hole transporting arylamine units have been previously investigated due to their promise as hole transporting materials. Two of the most widely studied copolymers are poly(9,9-dioctylfluorene-*alt*-bis-N,N'-(4-butylphenyl)-bis-N,N'-phenyl-1,4-phenylenediamine) (PFB) [78, 79] and poly(9,9-dioctylfluorene-*alt*-N-(4-butylphenyl)-diphenylamine) (TFB) [80, 81].

Here, we report a study of the hole charge carrier transport in four fluorene-arylamine copolymers comprising different ratios of 9,9-dioctylfluorene (F8) and butyl-substituted phenylenediamine (BSP). The dependence of the hole mobility on arylamine content has been investigated using dark injection transient (DIT) measurements and the results are discussed in the context of a transition from trap-controlled to trap-to-trap hopping transport. This transport model is further supported by ambient pressure photoemission spectroscopy measurements of the copolymers' molecular orbital energies. Furthermore, the materials under study have been optically characterised. It has been shown that once the β phase conformation is generated in the copolymers with long enough F8 chains, which are able to adopt a conformation change, the β phase fraction can be reduced thermally.

4.2 Materials

The chemical structure of the copolymers in this study is shown in figure 4.1 alongside the F8 homopolymer, PFO. The copolymers are denoted as x% F8: (100-x)% BSP or for short xF8:(100-x)BSP. The ratios are 95F8:5BSP, 90F8:10BSP, 80F8:20BSP and the alternating copolymer 50F8:50BSP (PFB). Their weight-average molecular weights are presented in table 4.1. The copolymers were synthesised using Suzuki coupling. The synthesis relies on the fact that BSP-BSP coupling is not possible and each BSP unit must be linked to F8 neighbours. The ratios depend on the BSP

monomer concentration. The copolymers were kindly provided by the Sumitomo Chemical Company Tsukuba Research Laboratory.

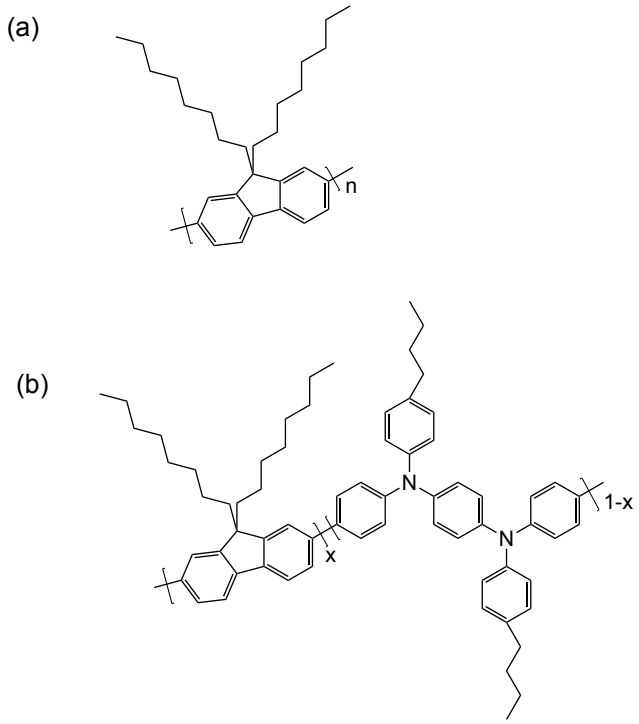


Figure 4.1: Chemical structures of (a) 100F8 (PFO) and (b) the 9,9-dioctylfluorene:butyl-substituted phenylenediamine (F8:BSP) copolymers ($x = 0.95$, 0.90, 0.80 and 0.50 for 95F8:5BSP, 90F8:10BSP, 80F8:20BSP and 50F8:50BSP).

Material	M_w ($\mathrm{g\,mol^{-1}}$)
95F8:5BSP	260×10^3
90F8:10BSP	330×10^3
80F8:20BSP	110×10^3
50F8:50BSP	300×10^3

Table 4.1: Weight-average molecular weights, M_w, of the fluorene-arylamine copolymers.

The F8 segments have desirable blue emission making such copolymers promising materials for optoelectronic applications. Furthermore, the F8 units permit the existence of multiple chain conformations with long F8 segments being able to adopt a rigid β phase conformation. On the other hand, the BSP units act as hole traps and have been shown to lower the ionization potential of the copolymer compared

to the PFO homopolymer, thus, assisting hole injection into the material [82].

Copolymer films containing both glassy phase and β phase F8 segments have been investigated. The preparation of glassy phase and β phase containing films has been described in detail in chapter 3 section 3.1.1. In short, for the fabrication of glassy phase films both solutions and substrates were placed on a hot plate at 100 °C for 5 minutes immediately prior to spin coating. Such samples are referred to as *hot spun* in the text. To generate F8 β phase chain segments postdeposition swelling of the glassy films was employed. This was done by exposing the hot spun films to toluene vapour at room temperature for 12 hours. These films are called *solvent vapour annealed (SVA)* in the text.

4.3 Optical Spectroscopy

The thin film photoluminescence (PL) spectra of the copolymers as well as a reference PFO homopolymer before and after solvent vapour treatment to generate F8 β phase chain segments are presented in figure 4.2. The measurements were performed at room temperature in ambient air using a 370 nm light excitation.

The glassy phase copolymer films show a broad, asymmetric, red shifted, featureless PL spectrum with a peak at 455 nm. The spectra are very similar to that of PFB. There is no significant PFO emission contribution, therefore, suggesting efficient energy transfer from locally excited F8 excitons to BSP-centered excitons [82, 83]. Hamilton et al. [82] have showed that the excited states responsible for the glassy phase emission have an appreciable charge transfer (CT) character similar to what has been previously observed for PFB and TFB [84]. They performed PL measurements on dilute solutions of PFO, PFB and the 95F8:5BSP copolymer in solvents of different polarities (toluene, tetrahydrofuran, and dichlorobenzene). The authors [82] reported that the PFB spectrum experienced a large red shift and broadening with increasing solvent polarity indicative of CT character while PFO

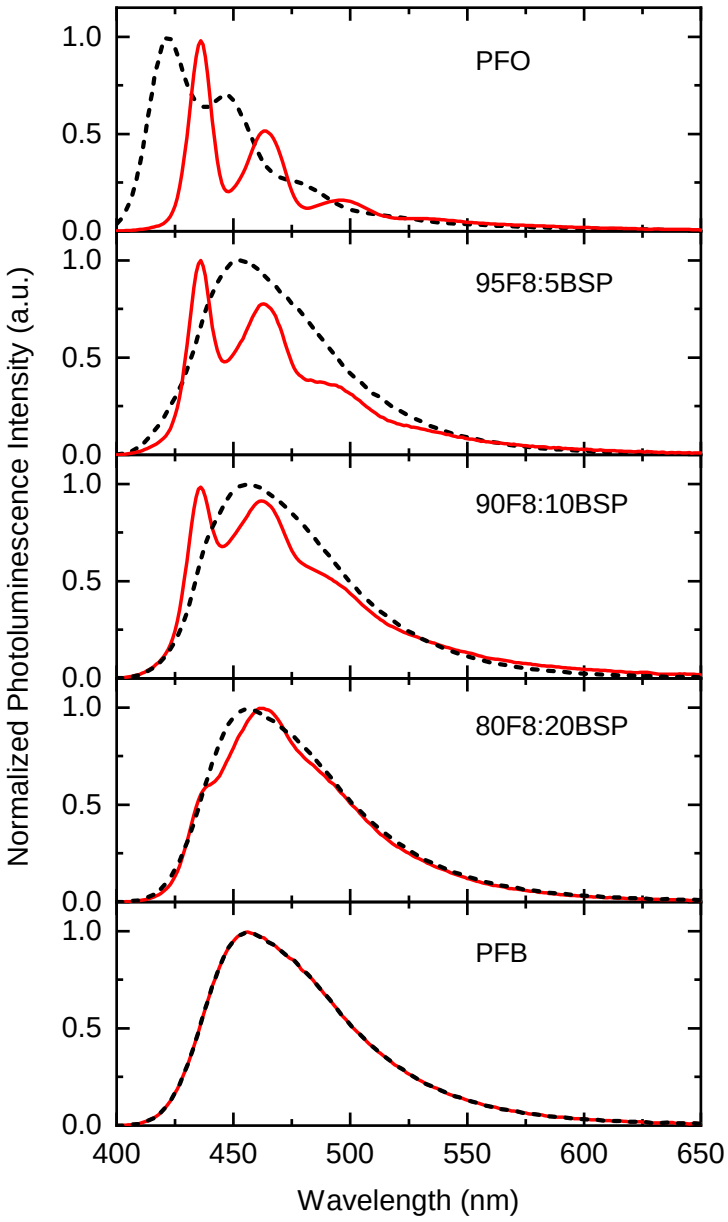


Figure 4.2: The thin film peak normalized PL spectra for hot spun (black dashed line) and solvent vapour annealed (red solid line) samples of PFO, 95F8:5BSP, 90F8:10BSP, 80F8:20BSP and PFB (50F8:50BSP).

showed little change with solvent polarity. They also observed that the 95F8:5BSP copolymer spectrum consisted of both vibronically structured F8 and broadband BSP-related contributions. The F8 features experienced no solvatochromic shift while the BSP-related features red shifted and broadened demonstrating the presence of both bound neutral exciton and CT emission states [82].

The copolymer PL spectra change significantly upon the generation of F8 β phase chain segments. The 95F8:5BSP copolymer PL spectrum shows a well-resolved vibronic structure similar to β phase PFO with the characteristic vibronic peaks at 436, 464 and 498 nm. However, the strength of the $S_1 - S_0$ 0-1 and 0-2 vibronic peaks relative to the 0-0 peak is higher for the copolymer compared to PFO suggesting that the copolymer β phase PL spectrum is a superposition of β phase PFO-like structured emission and PFB-like CT emission. Efficient energy transfer from high energy glassy phase to low energy β phase F8 chain segments leads to the dominant β phase vibronic emission in the spectrum. This is consistent with previous reports of energy transfer between the two phases of PFO [49, 85]. β phase PL components can also be seen to a lesser extent in the 90F8:10BSP and slightly as shoulders in the 80F8:20BSP copolymer film spectra. This indicates that as the BSP content increases, excitons localize at BSP units preventing migration to β phase segments, therefore, leading to a stronger residual contribution of BSP-centered emission. The BSP units do not prevent the formation of β phase chains and the small fraction of BSP units ensures that there are long enough F8 segments that can adopt this rigid conformation. This is in contrast to the alternating copolymer PFB (50F8:50BSP) where β phase features are not observed due to the lack of an extended sequence of F8 units [82]. β phase features have been reported in oligofluorenes with as few as five F8 repeat units [86].

Next, the thermodynamic stability of the β phase conformation of the 95F8:5BSP and 90F8:10BSP copolymers was investigated. This was done by thermal annealing of β phase copolymer films for 10 minutes at stepwise increasing temperatures. The

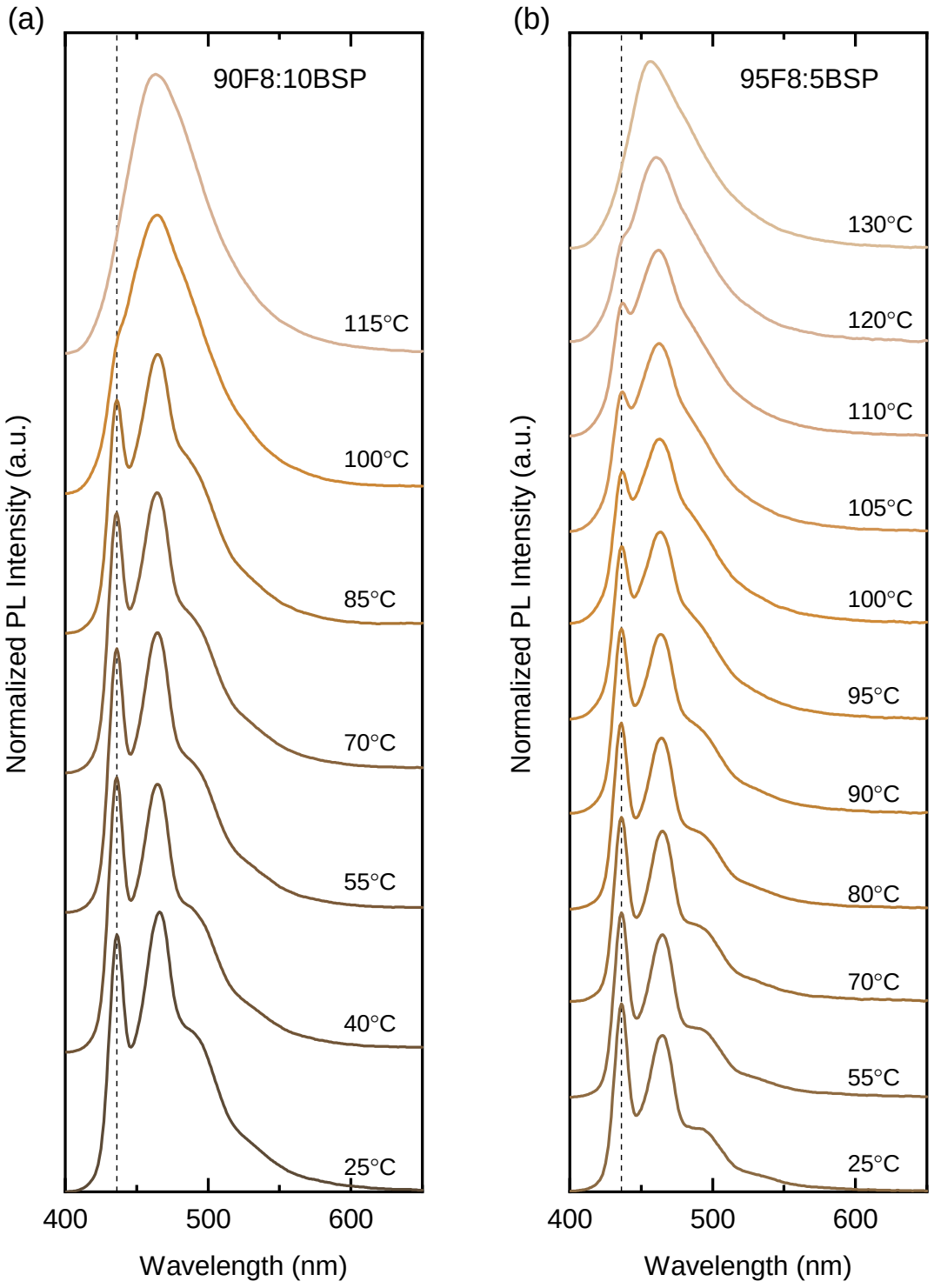


Figure 4.3: The peak normalized PL spectra for solvent vapour annealed films of (a) 90F8:10BSP following thermal annealing from 25 °C to 115 °C and (b) 95F8:5BSP following thermal annealing from 25 °C to 130 °C. The spectra have been displaced along the vertical axis for ease of comparison. The vertical dashed lines are drawn at the position of the first vibronic peak of β phase PFO (436 nm). The spectra overlaid on top of each other can be found in appendix A figure A.1.

thermal annealing was performed in a nitrogen-filled dry glovebox to avoid film degradation. After each annealing step the films were allowed to cool down to room temperature, only then the PL spectra and PLQE were measured. The PL spectra are presented in figure 4.3.

Both copolymers' spectra gradually lose their vibronic structure transitioning to the broad, asymmetric glassy phase spectrum above the crystallization temperature of PFO ($90 - 140\,^{\circ}\mathrm{C}$ depending on molecular weight [11, 61, 87]). There are no crystalline PFO emission contributions observed. As a result of the extended chain conformation of crystalline PFO, its PL emission is red shifted with characteristic vibronic peaks at 432, 459 and 484 nm [11, 88]. The absence of crystallization upon thermal annealing for the copolymer films in contrast to reports for pure PFO [42, 60, 61] implies that the bulky BSP units disrupt close chain packing into an ordered crystal. The PLQE values measured for the two copolymer films did not change as a result of thermal annealing. The PLQE of the 95F8:5BSP copolymer had a constant value of $40 \pm 5\%$ while the value for the 90F8:10BSP copolymer was $35 \pm 5\%$. This indicates that the thermal process did not significantly degrade the emission properties of the materials.

The data was further analysed by deconvolving the spectra to determine the β phase PL contribution to the emission at each temperature. Representative deconvolutions are shown in figure 4.4. The full set of deconvolutions is presented in appendix A section A.1. The PL spectra were fitted to a sum of two reference PL spectra: the PL spectrum of the respective glassy copolymer film (dashed red line in figure 4.4) and the PL spectrum of β phase PFO (dashed blue line in figure 4.4). The weightings of the reference spectra were adjusted in order for the sum (solid black line in figure 4.4) to give a good fit to the measured PL spectra (open green circles in figure 4.4). The percentage contribution of β phase emission was then calculated from the ratio of the integrated intensities. The observed small discrepancies between the experimental data and fit are likely due to the

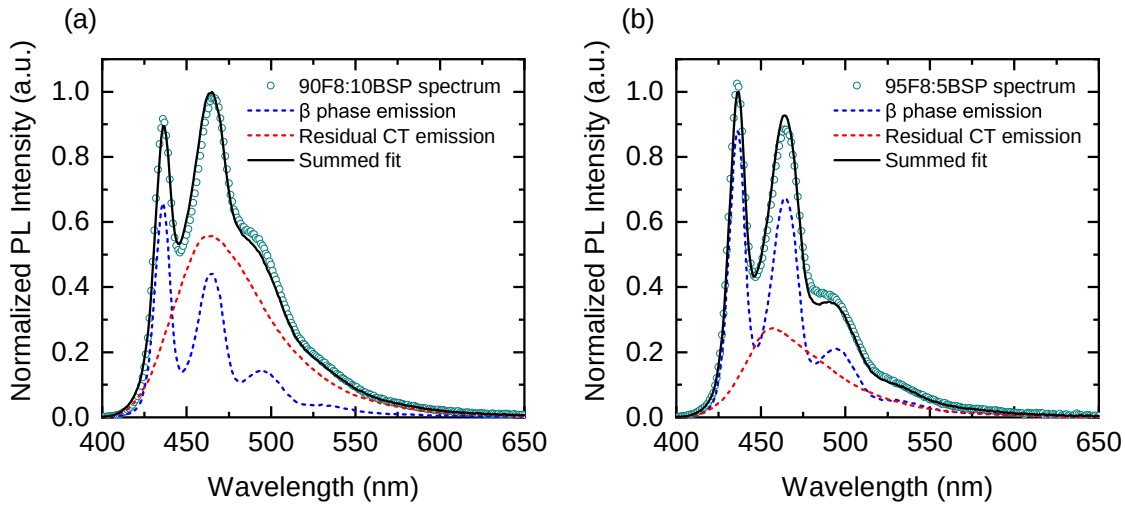


Figure 4.4: Representative deconvolution of PL spectra for (a) solvent vapour annealed film of 90F8:10BSP and (b) solvent vapour annealed film of 95F8:5BSP following thermal annealing at 55 °C for 10 minutes. The dashed red line gives the residual PFB-like CT emission while the dashed blue line shows the vibronic β phase contribution. The black solid line is the combined sum of both while the open green circles show the experimentally measured PL spectra.

oversimplified assumption that the β phase PL contribution of the copolymer can be represented by a scaled β phase PFO PL spectrum. The full set of results are plotted in figure 4.5.

Firstly, the deconvolution shows that the initial β phase PL content in the solvent vapour annealed film of the 95F8:5BSP copolymer is about 70% while for the 90F8:10BSP copolymer this value is about 40%. This confirms our earlier qualitative observation that as the BSP content increases, the β phase PL contribution decreases. Secondly, we note that as the copolymer films are annealed at higher temperatures their β phase content is progressively lowered until the films become completely glassy at $100 - 115\,^{\circ}\mathrm{C}$ for 90F8:10BSP and $120 - 130\,^{\circ}\mathrm{C}$ for 95F8:5BSP. We suspect thermal molecular vibrations tend to disrupt the ordered molecular arrangement and lead to a transition to the disordered glassy phase. The resulting broad featureless emission is a consequence of energy transfer from the glassy phase PFO segments to BSP-centered CT states as discussed earlier. Finally, we note that

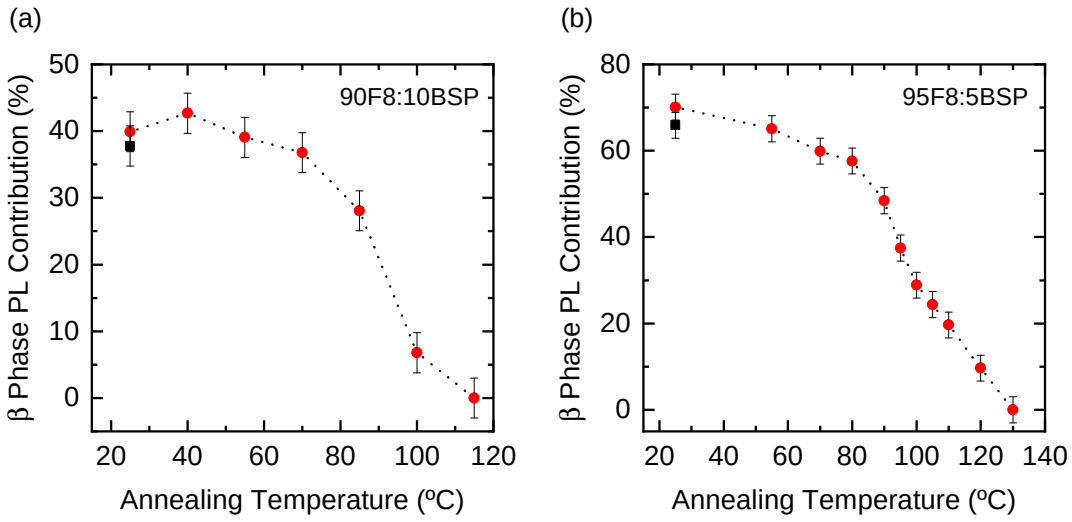


Figure 4.5: The estimated β phase contribution to the PL emission as a function of thermal annealing temperature (red circles) for solvent vapour annealed films of (a) 90F8:10BSP and (b) 95F8:5BSP. The β phase contribution upon a second solvent vapour annealing treatment is shown as a black square for both materials.

upon a second solvent vapour annealing treatment we were able to re-induce the β phase conformation (black squares in figure 4.5), thus, demonstrating that these temperature dependent transitions are substantially reversible. The change in β phase contribution was not significantly dependent on the annealing time; 5 and 10 minute intervals were both looked at.

These results are very interesting, opening new avenues for the exploration of polymer dynamics. In particular, the difference in the threshold transition temperatures for the two copolymers and its relationship to the BSP content deserve further attention. The arylamine unit is bulky, therefore, a higher arylamine concentration can lead to more free volume for the β phase to move into and transition to the glassy phase lowering the activation temperature for the transition for 90F8:10BSP compared to 95F8:5BSP. The dependence of the glass transition temperature of the copolymers on arylamine content can also give further insight into the polymer dynamics. Thus, we propose future work should include a differential scanning calorimetry (DSC) study.

4.4 Charge Transport

The dependence of hole charge carrier transport on arylamine content was studied using dark injection transient (DIT) measurements. The DIT method has been described in detail in chapter 3 section 3.2.1. To investigate hole mobility the copolymer films need to be sandwiched between a hole injecting contact and an injection blocking contact, therefore, the structure ITO/PEDOT:PSS/Copolymer/Al was employed. Theoretical calculations and experimental evidence suggest that for DIT measurements the injection barrier should not exceed $0.3 - 0.4\,\text{eV}$ for ohmic injection to sustain SCLC current flow [89]. The copolymers' HOMO levels have been estimated from cyclic voltammetry (CV) measurements to be in the range of $5.05 - 5.49\,\text{eV}$ [78, 82] while ultraviolet photoelectron spectroscopy (UPS) and electroabsorption measurements of PEDOT:PSS coated ITO have reported an ionization potential of $5.0 - 5.2\,\text{eV}$ [90–92]. Thus, the PEDOT:PSS coated ITO contact should be able to supply enough carriers per unit time to maintain SCL conditions. The devices were fabricated as described in chapter 3 section 3.2.1.1 and a schematic of the device structure is given again in figure 4.6. All measurements were performed at room temperature in ambient air. There was no evidence of sample degradation during the experiments.

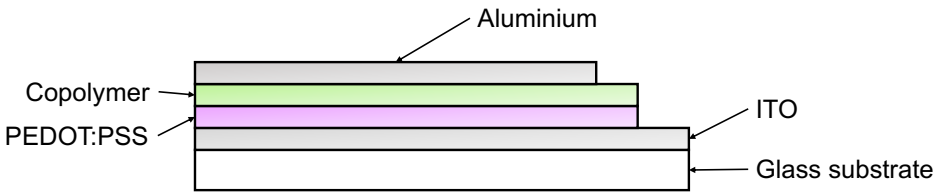


Figure 4.6: Cross section of the device structure of a hole-only copolymer DIT device.

Typical DI current transients at a variety of applied voltages for the 50F8:50BSP copolymer are shown in figure 4.7. The current response consists of an initial spike at the beginning of the voltage step due to the device capacitance (RC response

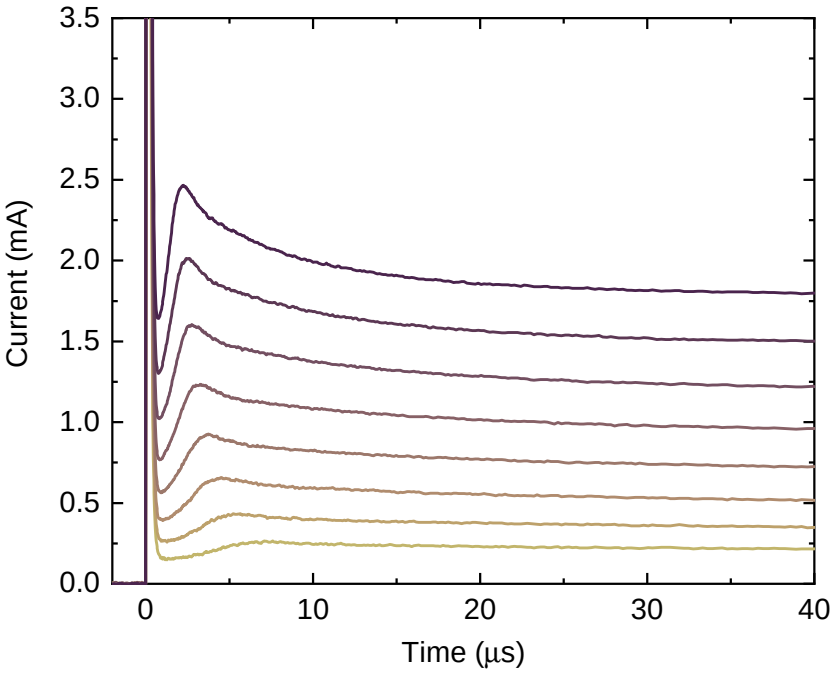


Figure 4.7: Representative hole injection transients for an 820 nm thick film of 50F8:50BSP under voltage pulses from bottom to top of 5, 6, 7, 8, 9, 10, 11 and 12 V.

time). This is followed by the DI transient with a peak at t_{DI}. Care was taken to ensure that the RC constant, τ, of the measurement is much smaller when compared with the measured t_{DI} so that t_{DI} could be correctly determined. Finally, at longer times, the charge distribution reaches dynamic equilibrium and the SCLC density is reached. Representative DI hole current transients for both the glassy and β phases of the 80F8:20BSP, 90F8:10BSP and 95F8:5BSP copolymers are presented in appendix A section A.2. DI transit times were readily identified indicating that PEDOT:PSS provides an ohmic injecting contact as expected from the ionisation potentials of the materials [93]. Representative current voltage characteristics of the hole-only DIT devices under study are presented in appendix A section A.3.

Figure 4.8 shows the hole mobilities deduced from the transit times as a function of the square root of the applied electric field for all the copolymers under study.

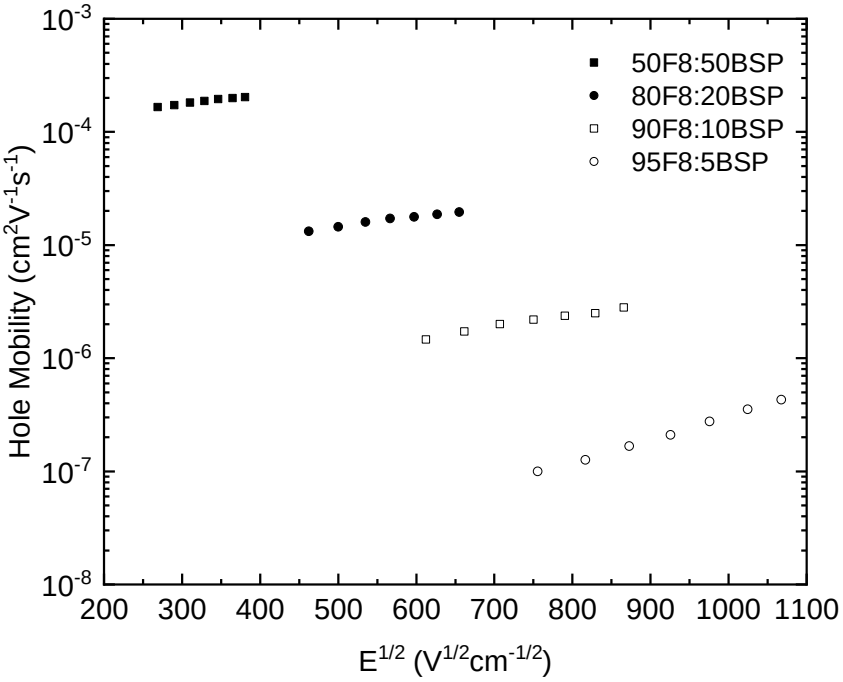


Figure 4.8: Comparison of the room temperature field dependent hole mobility values for 50F8:50BSP (filled black squares), 80F8:20BSP (filled black circles), 90F8:10BSP (open black squares) and 95F8:5BSP (open black circles).

The mobility values measured for each copolymer were independent of conformation (glassy phase or β phase). It has been shown that β phase PFO polymer chains have higher intrachain mobility than glassy chains [94]. Nevertheless, the bulk film mobility of β phase containing PFO thin films has been reported to be lower than the value for fully glassy films [95]. The extended β phase chain segments possess less deep lying HOMO energies and, thus, act as trapping sites for holes. However, the lack of such a distinction here suggests that hole transport in the copolymers is dominated by the effect of the arylamine moiety with the F8 chain conformation providing a less significant contribution. The ranges of electric field values studied for the four copolymers are different due to the limited voltage output of the DIT setup. Different sample thicknesses had to be used for the different materials since lower arylamine content copolymers required higher electric fields in order to obtain clear transients. This can be caused by charge trapping. Many and Rakavy [73]

have shown that as traps are introduced in a perfect insulator the current maximum in a DI transient gradually disappears. This happens as the characteristic trapping time becomes comparable with or smaller than the SCL transit time, t_{tr}. Since the transit time decreases as the sample thickness decreases while the trapping time remains the same this results in less trapping. Additionally, when the electric field is higher, the Fermi level rises filling deep traps, thus, reducing the influence of trapping, again resulting in clearer transient features [96].

The mobility shows a Poole-Frenkel (PF)-like behaviour [97], with a field dependence that can be described by

$$\mu(E) = \mu_0 \exp\left(\gamma\sqrt{E}\right), \tag{4.1}$$

where μ_0 is the (extrapolated) zero field mobility, γ is a parameter that characterises the strength of the field dependence for a particular material and E is the applied electric field. Such behaviour is common for organic semiconductors as a result of energetic disorder among transport sites [41, 98]. The extracted transport parameters (μ_0 and γ) are summarised in table 4.2 together with the literature values for PFO.

Material	μ_0 ($\mathrm{cm^2V^{-1}s^{-1}}$)	γ ($\mathrm{cm^{1/2}V^{-1/2}}$)	Reference
PFO	3×10^{-4}	0.2×10^{-3}	[80]
50F8:50BSP	1×10^{-4}	0.8×10^{-3}	This work
80F8:20BSP	5×10^{-6}	0.9×10^{-3}	This work
90F8:10BSP	4×10^{-7}	1.1×10^{-3}	This work
95F8:5BSP	2.8×10^{-9}	2×10^{-3}	This work

Table 4.2: Comparison of the transport parameters of the four fluorene-arylamine copolymers and PFO.

The hole mobility values of the copolymers at an electric field of $5 \times 10^5\,\mathrm{V\,cm^{-1}}$ (typical for OLED operation) are plotted against arylamine content in figure 4.9, alongside the literature value for PFO. For the 50F8:50BSP and the 80F8:20BSP copolymers the mobility values were extrapolated from the electric field dependence

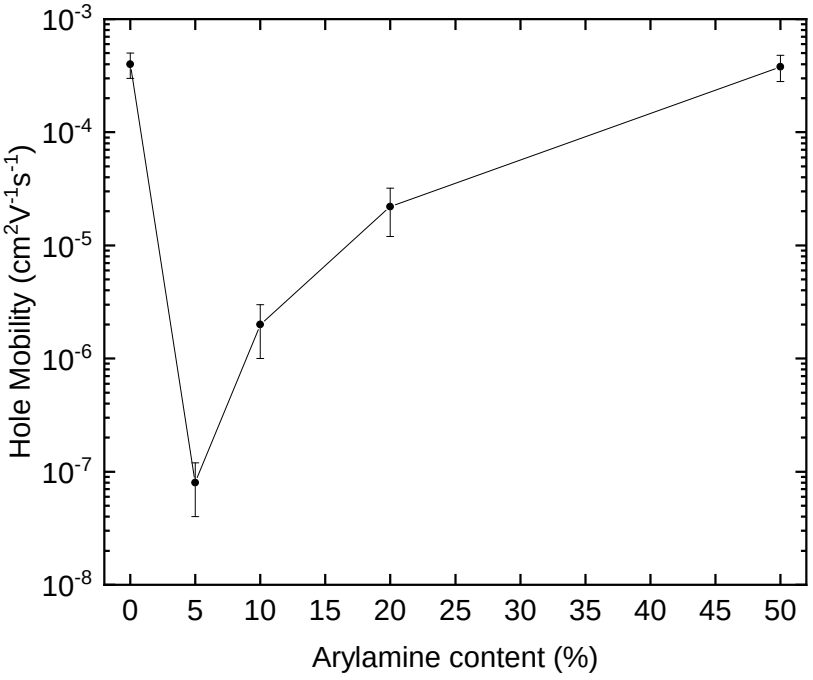


Figure 4.9: The room temperature hole mobilities of PFO, 95F8:5BSP, 90F8:10BSP, 80F8:20BSP and 50F8:50BSP at an electric field of $5 \times 10^5\,\mathrm{V\,cm^{-1}}$. The values for 50F8:50BSP and 80F8:20BSP were extrapolated using the measured electric field dependence presented in figure 4.8. The PFO value was taken from Redecker and Bradley [4].

displayed in figure 4.8. For PFO, the room temperature hole mobility at an electric field of $5 \times 10^5\,\mathrm{V\,cm^{-1}}$ is reported as $4 \times 10^{-4}\,\mathrm{cm^2V^{-1}s^{-1}}$ [4, 42, 99]. The hole mobility of the copolymer containing 5% arylamine, 95F8:5BSP, drops by roughly four orders of magnitude to $8 \times 10^{-8}\,\mathrm{cm^2V^{-1}s^{-1}}$. Subsequently, the mobility increases to $2 \times 10^{-6}\,\mathrm{cm^2V^{-1}s^{-1}}$ for the 10% arylamine copolymer, 90F8:10BSP. The hole transport improves further for the 20% arylamine copolymer, 80F8:20BSP, reaching a value of $2.2 \times 10^{-5}\,\mathrm{cm^2V^{-1}s^{-1}}$. Finally, the highest copolymer hole mobility of $3.8 \times 10^{-4}\,\mathrm{cm^2V^{-1}s^{-1}}$ is measured for the alternating copolymer 50F8:50BSP (PFB). This is in good agreement with previously reported values for PFB [78, 79].

The observed mobility change with arylamine content can be explained in the context of a transition from trap-controlled to trap-to-trap hopping transport.

Charge transport in amorphous organic semiconductors is a hopping process and occurs by charge transfer between neighbouring transport sites. In a trap free system, the distribution of energy of hopping sites is said to be narrow since similar amounts of energy are required to free charges from all the hopping sites. In a system containing traps, however, there are sites which require much more energy to release charges from them back to the majority hopping sites as illustrated in figure 4.10. Based on this, a molecule would act as a hole trap for transport via another molecule if the former has a lower ionization potential. Holes will fall into those traps and will only be released when there is sufficient activation energy, therefore, retarding hole transport. However, above a threshold trap concentration, the mobility will increase due to trap-to-trap conduction. The charge carriers will begin to percolate among the trap sites rather than making an energy consuming detrapping process to the matrix sites.

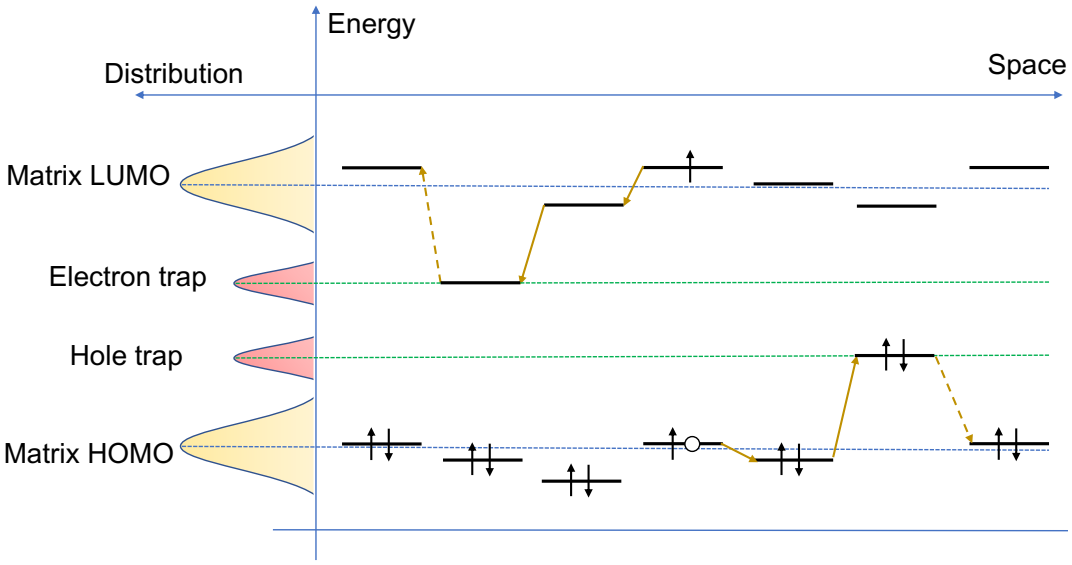


Figure 4.10: Illustration of how a higher energy filled site may act as a hole trap from which escape is retarded, therefore, reducing hole mobility. Similarly, a lower energy empty site can form a trap for electrons that lowers electron mobility. Adapted from [7].

In the copolymer structure, the arylamine moiety has a lower ionization potential compared to the deep HOMO level of PFO and can, therefore, act as a hole trap.

This is supported by ionization potential values extracted from APS measurements. The values were obtained by plotting the cube root of the photoemission current against photon energy which forms a straight line that is then extrapolated to the baseline signal. The cube root plot is used since it has been empirically shown that in most semiconductors the photoemission current increases with the cube of the photon energy above the ionisation potential [75–77]. Further details about the measurement technique can be found in chapter 3 section 3.2.2. The APS data obtained for glassy films of the copolymers and PFO is presented in figure 4.11. The extrapolated baseline intercepts for PFO and PFB are in agreement with literature values for their ionization potentials [78, 82, 100].

For the lower mobility copolymers, i.e. 95F8:5BSP, 90F8:10BSP and 80F8:20BSP, two separate straight line segments could be fitted to the data resulting in two distinct intercepts. Therefore, two distinct energy levels contribute to the measured photoemission signal. We speculate that the lower energy level corresponds to the BSP unit constituting a hole trap within the F8 matrix, which in turn we assign to the higher energy level contribution. Similar observations have been reported for CV measurements of the 95F8:5BSP copolymer. Two oxidation peaks were seen in the cyclic voltammogram of a thin film 95F8:5BSP sample [82]. The higher energy peak was assigned to F8 oxidation while the lower energy peak (situated $\sim 0.3\,\text{eV}$ below) was attributed to preferential oxidation of the BSP units. Miteva *et al.* [101] reported that end-capped polyfluorene with triarylamine groups resulted in two discrete energy levels, estimated by CV to be 5.48 eV for amine and 5.88 eV for fluorene. Thus, showing that the attached end groups act as independent electroactive units constituting hole traps within the polyfluorene matrix. Finally, copolymer samples containing β phase F8 chains showed the same behaviour and the energy values extracted were consistent (within the experimental error) with the glassy film values. The ionization potential of β phase PFO has been reported to be $\sim 120 - 140\,\text{meV}$ lower than the value for the glassy phase [95], however, the lack of an observable distinction between the two conformations suggests the

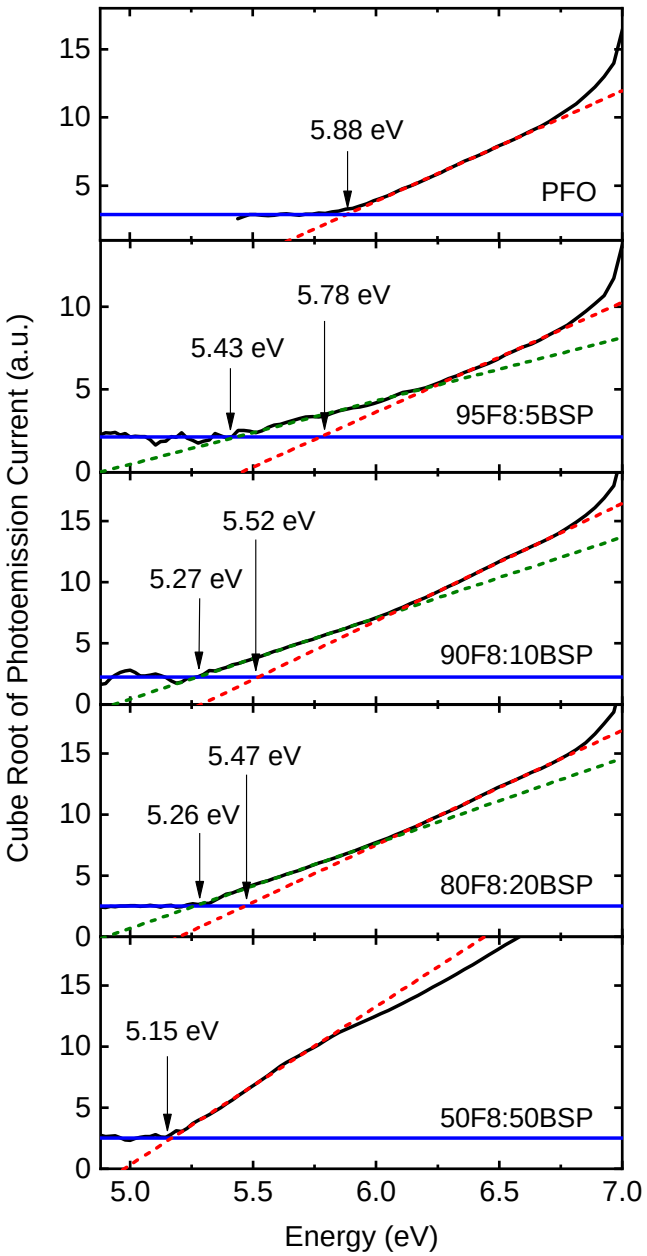


Figure 4.11: Air photoemission spectroscopy data (black line) for glassy phase PFO, 95F8:5BSP, 90F8:10BSP, 80F8:20BSP and 50F8:50BSP. The energy levels are determined by extrapolating the linear part of the curve down to the baseline signal level (blue horizontal line). The dashed lines are linear fits to the experimental data. The extrapolated baseline intercepts are labelled on the plots and the experimental error on the obtained values is $\pm 0.05\,\mathrm{eV}$.

resolution of the experiment does not allow to detect it.

The alternating copolymer, 50F8:50BSP, displays the lowest photoelectric threshold and consequently the strongest photoresponse. Its photoemission data fits well to a single straight line, thus, one energy level is derived suggesting hole transport proceeds through a single transport level. The photoemission response at higher photon energies (above 5.75 eV) was not fitted to a second straight line segment as the resulting baseline intercept would lie lower than the value obtained for the low photon energy region. This would be unphysical since as the incident photon energy increases, signal from higher energy rather than lower energy states is expected. Therefore, we assign this to a measurement artefact rather than an additional ionization potential component. Such APS photoresponses are common and have been reported previously [75, 102].

The obtained ionization potential energy values are plotted against arylamine content in figure 4.12. From this plot we observe that the two energy level contributions shift to lower energies with increasing arylamine content. Additionally, the energy difference between the two contributions decreases as the arylamine content in the copolymers increases resulting in an effectively lower trap depth, vanishing for PFB. It is unclear whether the observed energy level shifts originate from a change in the energies of the two states and/or a change in their relative contributions since it is not possible to quantify the width of the DOS distributions from the above measurement. In a disordered organic semiconductor containing traps, both the intrinsic hopping states and the traps will have inhomogeneously broadened DOS distributions. The widths of the distributions will be determined by the variations in the site energies and the distances between the sites.

Nevertheless, an interesting parallel can be drawn between our observations and an effective medium approximation (EMA) model and thermally stimulated luminescence (TSL) measurements published by Fishchuk *et al.* [103]. The EMA model

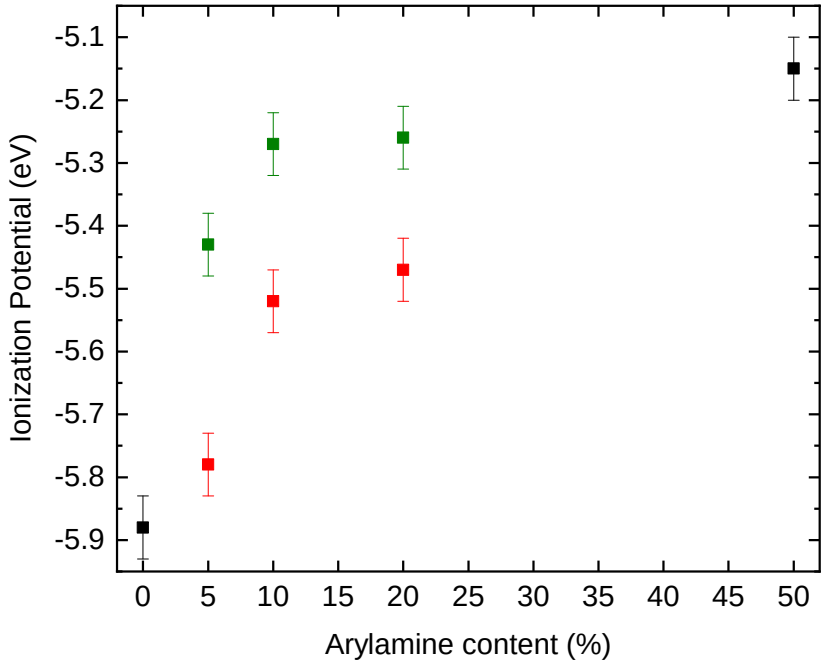


Figure 4.12: Ionization potential energies derived from air photoemission spectroscopy for PFO, 95F8:5BSP, 90F8:10BSP, 80F8:20BSP and 50F8:50BSP. For PFO and 50F8:50BSP a single ionization potential value was extracted (black squares). For 95F8:5BSP, 90F8:10BSP and 80F8:20BSP two discrete ionization potentials are obtained. The lower energy components are denoted by green squares while the higher energy contributions are represented with red squares.

they developed suggests that in a trap-containing medium the effective disorder parameter decreases at large trap concentration. They further supported this theory with TSL measurements of poly(9,9-bis(2-ethylhexyl)fluorene-2,7-diyl) (PF2/6) containing different concentrations of deliberately introduced tri-p-tolylamine traps. In TSL, trapping states are populated by photogeneration of charge carriers at low temperature to ensure trapped charges are not released immediately. The sample is then heated gradually until the trapped charges gain enough thermal energy to escape the traps. The luminescence due to radiative recombination is recorded as a function of temperature. It has further been shown that the TSL peak energy is proportional to the effective disorder parameter [104]. Fishchuk *et al.* [103] reported that the TSL peak associated with the trap states shifts to lower temperatures at larger trap concentrations. They explained this low temperature shift in terms of

percolative type motion of charge carriers within the trap manifold as the distance between traps becomes sufficiently close for transport. We observe a very similar behaviour for the extracted effective trap depth (difference between the two IP level contribution) in our copolymers under study. We see a decrease in effective trap depth with increasing trap concentration. Fishchuk *et al.* [103] concluded from their study that charge trapping experiments such as TSL do not provide an exact value for the difference between the energy levels of the trap and transport sites (true trap depth) but rather an effective value which is a function of trap depth, energetic disorder and trap concentration. Temperature and field dependent charge carrier mobility experiments have also reported disorder parameter values in agreement with this [79]. How the effective trap depth we have extracted is related to the activation energy for transport and the disorder parameter value in a material is an interesting direction for future investigation. Exploring the potential of the APS technique for studying charge trapping deserves further attention. This measurement method does not require vacuum conditions or low temperatures, therefore, significantly reducing experimental efforts compared to TSL and charge carrier mobility studies. Comparing APS data to TSL and charge mobility experiments would shed further light on its applicability for studying charge trapping.

In the context of this mobility study, the APS data shows that for the 95F8:5BSP, 90F8:10BSP and 80F8:20BSP copolymers two energy level contributions are present with the lower energy level constituting a hole trap. Further insight into the energy levels and DOS distributions of the two moieties within the copolymers can be gained through supplementary measurements and device modelling. Determining the energy levels by CV and UPS would give additional comparison data. Information about the DOS distribution can be obtained by calibrating the APS measurements using metals of similar ionization potentials as the copolymers whose density of states are known. Finally, numerical device modelling using drift diffusion simulations can be employed to extract hole trap parameters from experimentally measured current

voltage characteristics as discussed in appendix A section A.3.

In summary, below a threshold BSP concentration, the hole mobility drops sharply due to trapping, but at higher concentrations the mobility increases due to direct arylamine-arylamine transfers. The hopping rate between two sites depends on the electronic coupling between the sites due to wavefunction overlap and, thus, on the intersite distance (Miller and Abrahams model [39]). As the concentration of BSP increases both moieties start to participate in the transport since the BSP intersite distance is reduced. The mobility here is still low because the distance between BSP units is large. Finally, when large arylamine concentrations are present, the transport proceeds mainly via the BSP moieties and the F8 chains only act as a binder. This is also consistent with the values extracted for the field dependence of the mobility in table 4.2. The field dependence decreases with increasing BSP content. The correlated disorder model [41, 98, 105] describing transport in organic materials predicts that the effect of increased intersite distance is both a reduction in μ_0 and an increase in the field dependence of the mobility. This relates to the higher degree of both positional and energetic disorder for the transport active sites. Similar observations have been made for organic semiconductors deliberately doped with traps [103, 106–108].

4.5 Conclusion

In conclusion, we have investigated the optical and hole transport properties of four fluorene-arylamine copolymers comprising different ratios of 9,9-dioctylfluorene (F8) and butyl-substituted phenylenediamine (BSP). The BSP fractions explored were 50, 20, 10 and 5% (figure 4.1). PL spectroscopy measurements of solvent vapour annealed copolymer films containing 20, 10 and 5% BSP exhibited β phase formation in the F8 chain segments. It was also demonstrated that heating the solvent vapour annealed copolymer films progressively lowers the β phase content until the films become completely glassy above 115 °C for 90F8:10BSP and 130 °C

for 95F8:5BSP.

Hole mobility was studied using the dark injection transient technique. The hole mobility of PFO ($4 \times 10^{-4}\,\mathrm{cm^2V^{-1}s^{-1}}$ [4, 42, 99]) is drastically reduced by the copolymerisation of only 5% BSP and the resulting 95F8:5BSP copolymer has a mobility four orders of magnitude lower than PFO ($8 \times 10^{-8}\,\mathrm{cm^2V^{-1}s^{-1}}$). With an increasing percentage of arylamine the charge transport is improved, and the alternating copolymer PFB has a mobility ($3.8 \times 10^{-4}\,\mathrm{cm^2V^{-1}s^{-1}}$) similar to that of PFO. This behaviour is interpreted on the basis of a transition from transport via the F8 units with trapping at the BSP sites to transport via the BSP moieties as their intersite distance is reduced with increasing arylamine concentration. Thus, at high trap concentrations transport through the trap state manifold becomes possible. Air photoemission spectroscopy measurements confirmed the presence of two discrete energy states with different ionization potentials for the 95F8:5BSP, 90F8:10BSP and 80F8:20BSP copolymers. The lower ionisation potential state acts as a hole trap and was assigned to the BSP moiety. This demonstrates that the hole mobility of an organic semiconductor could be controlled over a large range by the copolymerisation of different amounts of a lower ionisation potential transporting moiety.

5 Phenoxazine Copolymerisation

This chapter presents a study of a novel alternating fluorene-phenoxazine copolymer, F8BPPOZ. Incorporation of the phenoxazine polymer into a fluorene backbone leads to a more rigid structure with less torsions compared to a similar fluorene-triarylamine copolymer poly(9,9-dioctylfluorene-alt-N-(4-butylphenyl)-diphenylamine) (TFB). Resilience to thermal fluctuations of the torsions along the polymer backbone within and between structural domains has been proposed to determine the energy landscape and lead to low energetic disorder and high mobilities in materials. Therefore, F8BPPOZ is studied to investigate whether this rigid structure improves charge hopping and increases mobility compared to TFB. The performance of F8BPPOZ as a hole transporting material in polymer light emitting diodes is also tested and compared to TFB which is a commonly used interlayer. Finally, the exciton dynamics at a semiconductor polymer heterojunction with layers comprising blends of F8BPPOZ:F8BT and TFB:F8BT are looked at.

5.1 Introduction

Conjugated polymer materials enable the fabrication of flexible solution-processed semiconductor devices at low temperatures. Over the past decades intense research and development of applications employing conjugated polymers have taken place

including light emitting diodes (LEDs), field effect transistors and solar cells [7]. For all these applications charge carrier mobility has a critical effect on device performance. One of the major benefits of conjugated polymers is a material structure that can be easily modified by chemical synthesis in order to tailor their optoelectronic properties. The flexibility of synthetic organic chemistry allows materials to be tuned for different applications, however, careful molecular design is necessary to improve the performance of organic semiconductor devices. Recent reports [109–111] have highlighted the importance of backbone rigidity and resilience to torsional fluctuations for high charge carrier mobility. Charge transport in organic semiconducting polymers depends on a combination of intrachain transport along the polymer backbone and interchain charge hops between neighbouring chains. Intrachain transport can be enhanced when the polymer backbone has the least amount of intrinsic energetic disorder and it is resilient to torsional fluctuations between adjacent units [109–111]. Venkateshvaran *et al.* [109] performed measurements of the amount of disorder in different conjugated polymer films and demonstrated that the highly disordered indacenodithiophene-*co*-benzothiadiazole (IDTBT) copolymer with near amorphous microstructure [112] displays lower energetic disorder and fewer electronic traps than semicrystalline poly(2,5-bis(3-alkylthiophen-2-yl)thieno(3,2-b)thiophene) (PBTTT). Later, Lemaur *et al.* [110] through molecular dynamics simulations and quantum-chemical electronic structure calculations showed that high crystallinity and planar conjugated backbones are not required to get materials with low energetic disorder and high mobilities. It is instead resilience to thermal fluctuations of the torsions along the polymer backbone within and between structural domains that determine the energy landscape. Additionally, reducing the number of torsions per unit length helps to ensure a long persistence length, thus, efficiently driving the charge carriers over long distances along the polymer backbone [110].

Here, we characterise a novel fluorene-phenoxazine conjugated copolymer poly(9,9-dioctylfluorene)-*co*-(10-(4-butylphenyl)phenoxazine) (F8BPPOZ), kindly provided

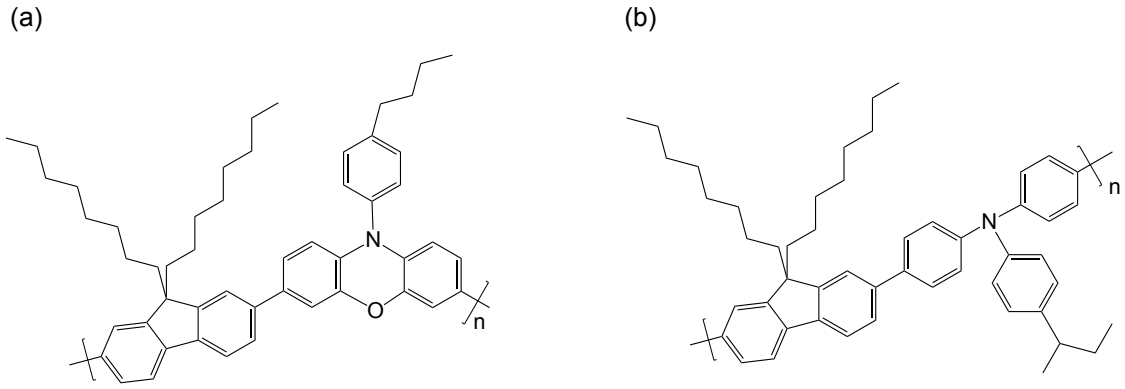


Figure 5.1: Chemical structures of (a) F8BPPOZ and (b) TFB.

by the Sumitomo Chemical Company Tsukuba Research Laboratory. Its weight-average molecular weight, M_w, is $317 \times 10^3\,\mathrm{g\,mol^{-1}}$. This copolymer's structure is similar to the well known hole transporting fluorene-triarylamine copolymer poly(9,9-dioctylfluorene-*alt*-N-(4-butylphenyl)-diphenylamine) (TFB). However, TFB possesses three free rotations around the single bonds surrounding the nitrogen atom while the introduction of the phenoxazine (POZ) ring takes two rotations out leaving only one free rotation of the pendant phenyl group (figure 5.1). Therefore, F8BPPOZ is expected to be more rigid than TFB and we explore whether this more rigid structure improves charge hopping and increases hole carrier mobility. Additionally, a more rigid structure can facilitate closer contact between chains and improved π stacking to enhance interchain mobility. Extra rotation can occupy space and make it hard for units to get close together.

TFB is a well studied hole transporter due to its low ionization potential ($\sim 5.3\,\mathrm{eV}$) [78, 113] and high hole mobility, reported in the literature to lie in the range $(5-10) \times 10^{-3}\,\mathrm{cm^2V^{-1}s^{-1}}$ [79, 80]. It has been shown that the inclusion of a $10-15\,\mathrm{nm}$ TFB interlayer between the poly(3,4-ethylenedioxythiophene):polystyrene sulphonate (PEDOT:PSS) hole injection layer and poly(9,9-dioctylfluorene-*alt*-bithiophene) (F8BT) emissive layer in polymer LEDs (PLEDs) enhances device performance due to its exciton blocking role [114, 115]. Thus, we have also compared the performance of TFB and F8BPPOZ as interlayers in PLEDs and analysed the differences in device performance.

5.2 Optical Characterisation

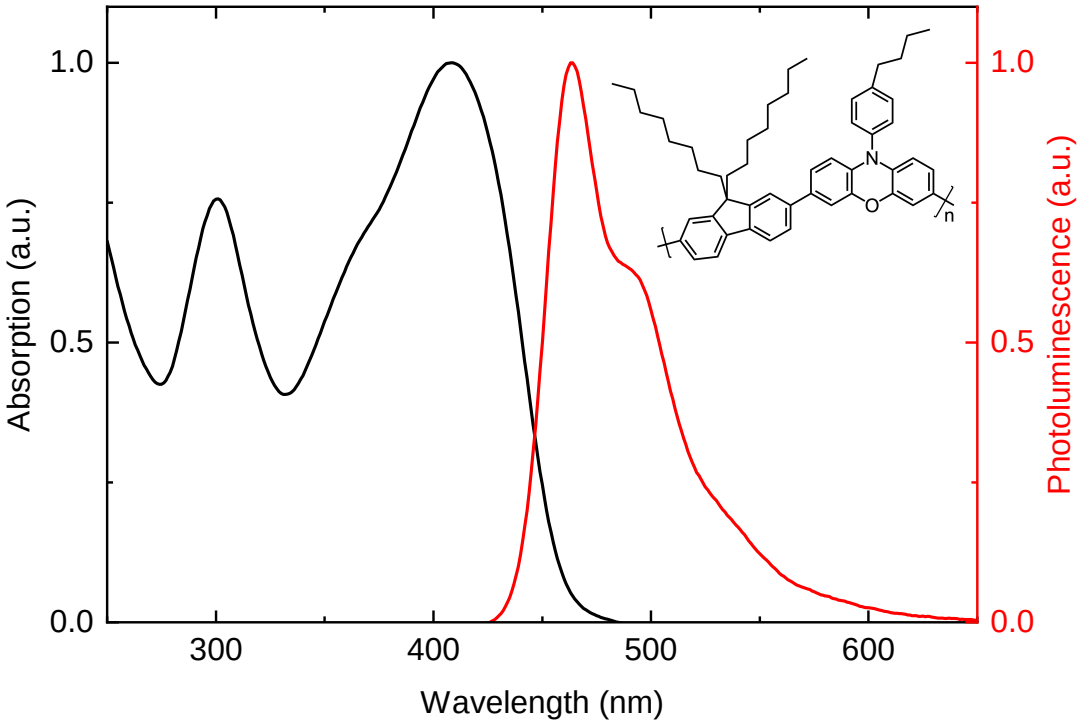


Figure 5.2: Peak normalized thin film absorption (black) and photoluminescence (red) spectra of F8BPPOZ. The PL emission spectrum was excited at 400 nm. The inset shows the chemical structure of F8BPPOZ.

The peak normalized thin film absorption and photoluminescence (PL) emission spectra of F8BPPOZ are presented in figure 5.2 alongside its chemical structure in the inset. The copolymer has a strong absorption band with a maximum at 409 nm and a shoulder around 370 nm. The absorption is red shifted compared to the polyfluorene homopolymer, PFO, whose absorption maximum is at 381 nm. It is also red shifted compared to the absorption maximum at 397 nm reported for a closely related phenoxazine homopolymer [116]. This red shift of the absorption compared to the individual homopolymers is a consequence of the charge transfer (CT) character of the copolymer. A theoretical study by Yang *et al.* [117] on a model fluorene-phenoxazine copolymer calculated that the HOMO orbitals are

mainly located on the POZ rings while the LUMO orbitals are localized on the fluorene units. Additionally, F8BPPOZ has a high energy absorption band with a peak at 301 nm. This absorption is characteristic of the POZ unit and has been observed in phenoxazine based conjugated polymers [116] as well as small molecules [118]. The PL spectrum has an emission band with a peak at 464 nm and a vibronic shoulder around 493 nm. The PLQE value measured is $7 \pm 5\%$. This is much lower than the PLQE value of PFO ($\sim 45 - 50\%$) [1] suggesting that there is indeed charge transfer and, therefore, reduced orbital overlap leading to lower optical transition rates.

5.3 Thermal Characterisation

The thermal properties of the copolymer were evaluated by differential scanning calorimetry (DSC). DSC is a thermal analysis technique where a material is heated or cooled in a controlled manner whilst the flow of energy into or out of the material is measured. This gives information about the transitions that take place within the material over the temperature range studied in combination with the temperature at which they occur. Here, power compensation DSC was used where separate furnaces heat the sample and reference pans. The power compensation necessary to maintain the set rate of temperature change for the sample and reference are measured and the difference between the signals is plotted [120]. The second heating and cooling DSC scans are presented in figure 5.3. The measurements were performed with a DSC Q2000 system from TA Instruments with a heating rate of $10\,^{\circ}\mathrm{C\,min^{-1}}$ in nitrogen. The scans show no melting or crystallization peaks up to 300 °C. A kink in the heating and cooling thermograms indicates the glass transition temperature T_g and its value is taken as the inflection point, $T_g = 196 \pm 4\,^{\circ}\mathrm{C}$. The high glass transition temperature of the F8BPPOZ copolymer indicates a rigid backbone [121]. The values of T_g for PFO and TFB are 50 °C [122] and 140 °C [123],

[1] This value was measured in chapter 6 section 6.4 and agrees well with values reported in the literature [3, 85, 119].

respectively, suggesting that incorporation of the rigid phenoxazine ring reduces segmental mobility and, therefore, improves thermal stability.

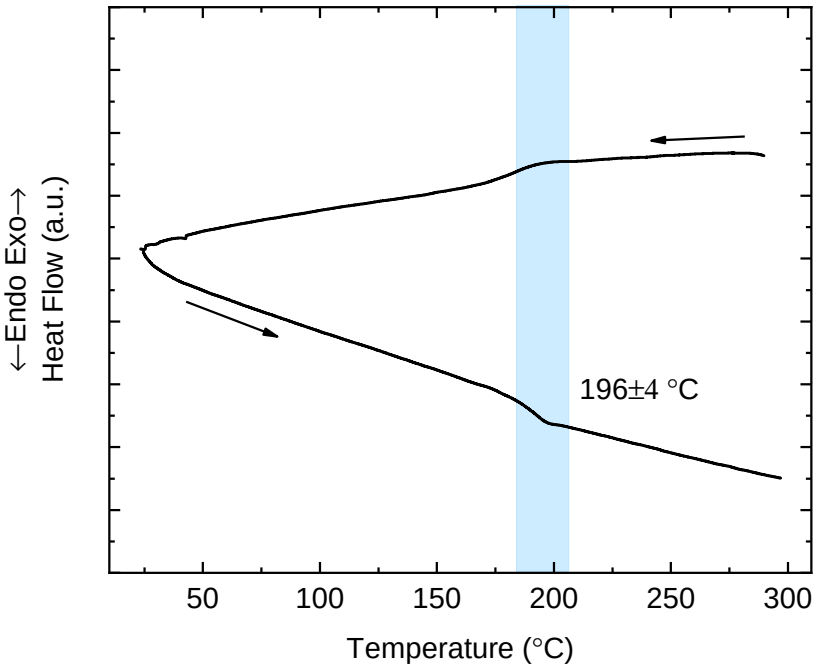


Figure 5.3: DSC second heating/cooling thermograms of F8BPPOZ recorded under nitrogen with a scan rate of $10\,^{\circ}\mathrm{C}\,\mathrm{min}^{-1}$.

5.4 Electrical Characterisation

Electrical characterisation of F8BPPOZ was performed to extract the ionization potential (IP) and electron affinity (EA) and the hole mobility of the copolymer. The IP was obtained using air photoemission spectroscopy (APS). The IP value was extracted by plotting the cube root of the photoemission current against photon energy which forms a straight line that is subsequently extrapolated to the baseline signal (figure 5.4). The cube root plot is used since it has been empirically shown that in most semiconductors the photoemission current increases with the cube of the photon energy above the ionisation potential [75–77]. The extrapolated baseline

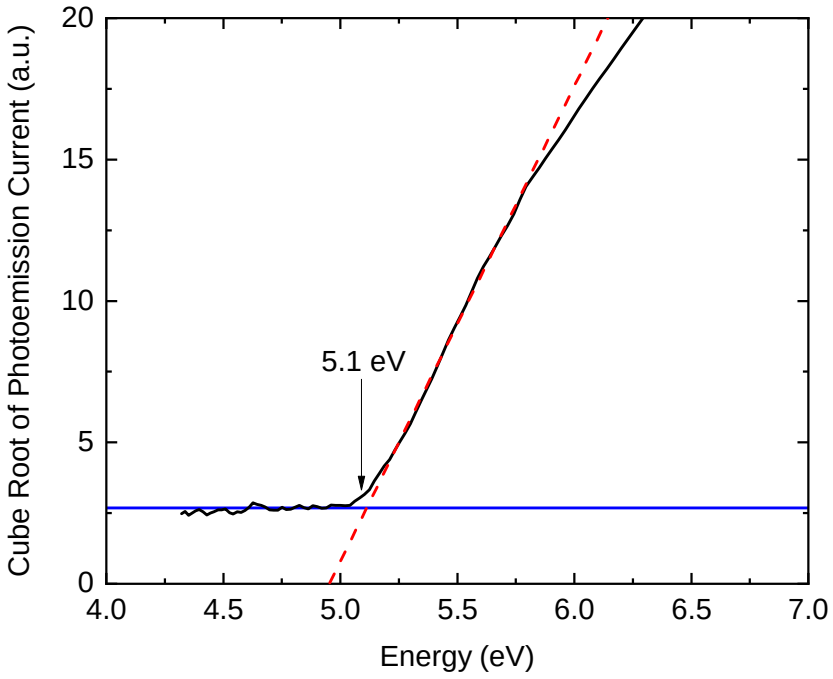


Figure 5.4: Air photoemission spectroscopy data (black line) for F8BPPOZ. The ionization potential is determined by extrapolating the linear part of the curve down to the baseline signal level (blue horizontal line). The dashed red line is a linear fit to the experimental data. The extrapolated baseline intercept is labelled on the plot and the experimental error on the obtained value is ±0.05 eV.

intercept is 5.1 ± 0.05 eV. The IP of PFO measured under the same conditions is 5.88 ± 0.05 eV [2], therefore, the phenoxazine unit does indeed lower the IP of the copolymer. The electron-donating POZ unit with its electron rich oxygen and nitrogen heteroatoms significantly improves the hole accepting properties of the copolymer compared to PFO. Further, the IP of F8BPPOZ is slightly lower than the value reported for TFB (~ 5.3 eV) [78, 113]. The optical gap of F8BPPOZ (taken as the absorption onset of the UV-Vis spectrum) is 2.7 ± 0.1 eV. Assuming an exciton binding energy of 0.3 ± 0.1 eV [124], the EA is estimated to be 2.1 ± 0.15 eV. This value coincides with the EA value reported for PFO [82, 100]. This is in agreement with the calculations by Yang *et al.* [117] of the electron distribution in a model fluorene-phenoxazine copolymer which yielded a LUMO orbital localized

[2] Measurement is presented in chapter 4 section 4.4.

on the fluorene moiety and a HOMO orbital situated mainly on the phenoxazine unit. Therefore, the LUMO level is dominated by the fluorene while the HOMO is tuned by the POZ ring.

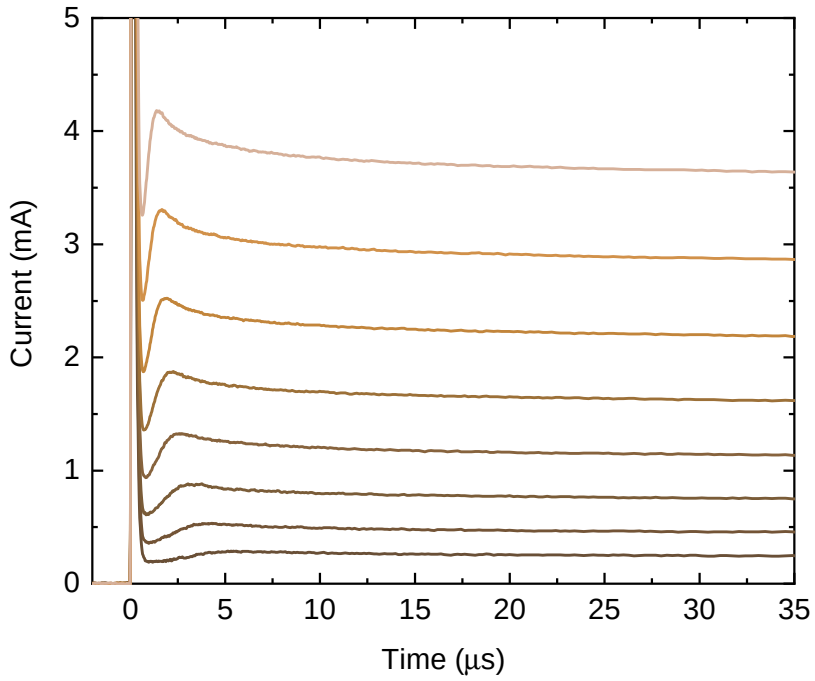


Figure 5.5: Representative hole injection transients for a 735 nm thick film of F8BPPOZ for voltage pulses from bottom to top of 5, 6, 7, 8, 9, 10, 11 and 12 V.

Finally, we study the hole charge carrier mobility of F8BPPOZ using dark injection transient (DIT) measurements. Hole-only devices with the structure ITO/PEDOT:PSS/F8BPPOZ/Al were employed. More details about the device fabrication are available in chapter 3 section 3.2.1.1. PEDOT:PSS was used to ensure that the anode can supply enough charge carriers to maintain space charge limited conditions (ohmic contact). Typical DI current transients for the copolymer at a variety of applied voltages are shown in figure 5.5. The DI transient peak times, t_{DI}, were used to extract the hole mobility as described in chapter 3 section 3.2.1. Figure 5.6 displays the calculated hole mobilities as a function of the square

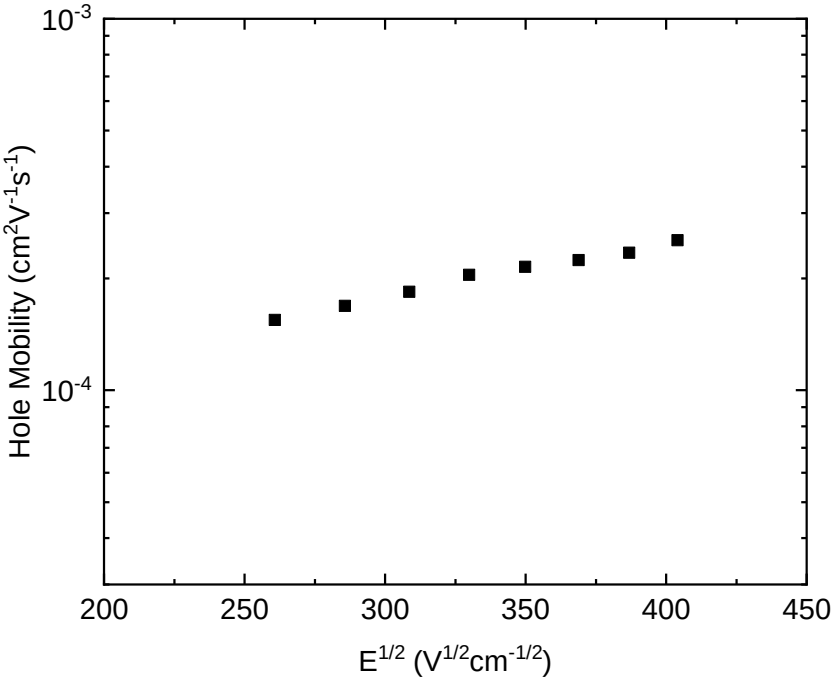


Figure 5.6: Field dependence of the hole mobility of F8BPPOZ. Each data point was determined from the peak of the DI transient as described in chapter 3 section 3.2.1.

root of the applied electric field. The mobility follows a Poole-Frenkel (PF)-like behaviour [97], with a field dependence described by

$$\mu(E) = \mu_0 \exp\left(\gamma\sqrt{E}\right), \tag{5.1}$$

where μ_0 is the (extrapolated) zero field mobility, γ is a parameter that characterises the strength of the field dependence for a particular material and E is the applied electric field. This behaviour is common for organic semiconductors as a result of energetic disorder among transport sites [41, 98]. The extracted transport parameters are $\mu_0 = 6.5 \times 10^{-5}\,\mathrm{cm^2V^{-1}s^{-1}}$ and $\gamma = 3.4 \times 10^{-3}\,\mathrm{cm^{1/2}V^{-1/2}}$. We compare these results to literature values for the fluorene homopolymer PFO ($\mu_0 = 3 \times 10^{-4}\,\mathrm{cm^2V^{-1}s^{-1}}$ and $\gamma = 0.2 \times 10^{-3}\,\mathrm{cm^{1/2}V^{-1/2}}$) [80]. The zero field mobility of F8BPPOZ is roughly an order of magnitude lower than the value for PFO while the electric field dependence is about an order of magnitude larger. Using the observed PF behaviour the hole mobility of F8BPPOZ was extrapolated

to an electric field of $5 \times 10^5\,\mathrm{V\,cm^{-1}}$ (typical for OLED operation) and a value of $7 \times 10^{-4}\,\mathrm{cm^2V^{-1}s^{-1}}$ was obtained. This is marginally higher than the corresponding hole mobility value for PFO of $4 \times 10^{-4}\,\mathrm{cm^2V^{-1}s^{-1}}$ [4, 42, 99] and at least an order of magnitude lower than the hole mobility reported for TFB ($(5-10) \times 10^{-3}\,\mathrm{cm^2V^{-1}s^{-1}}$ [79, 80]).

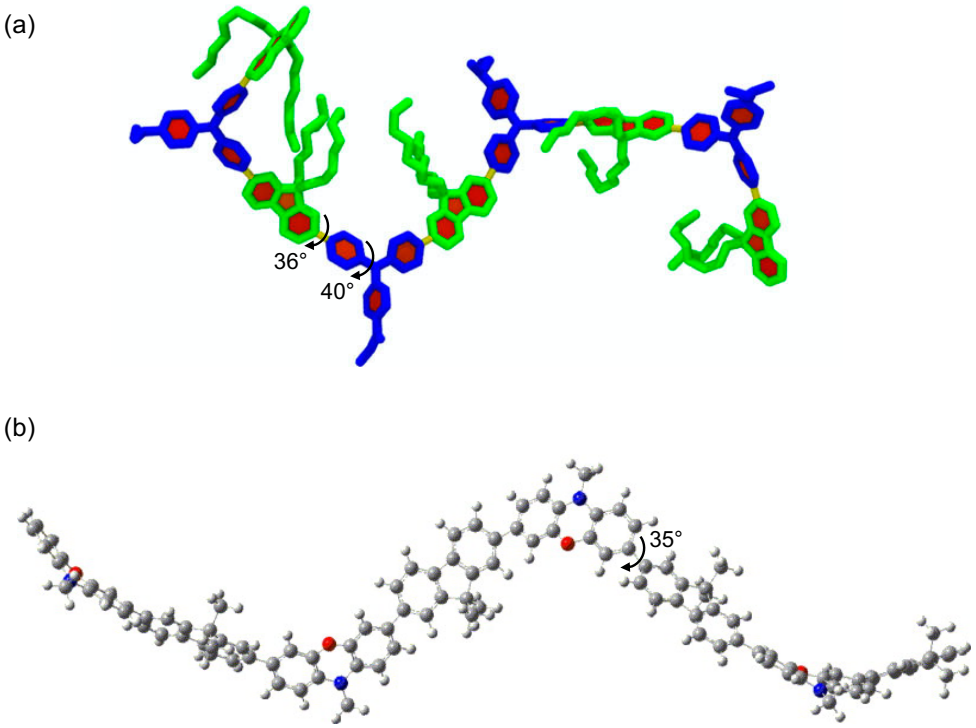


Figure 5.7: (a) Oligomer conformation of TFB. 9,9-dioctylfluorene and triphenylamine are shown in green and blue, respectively, while aromatic rings are highlighted in red. Reprinted from [125], with the permission of AIP Publishing. (b) Optimized molecular structure of poly[(10-methylphenoxazine-3,7-diyl)-*alt*-2,7-(9,9-dimethyl-fluorene)]. Oxygen and nitrogen atoms are denoted in red and blue, respectively. Reprinted from [117], with permission from Elsevier.

We conclude that the increased rigidity of F8BPPOZ compared to TFB does not improve the hole carrier mobility and other factors dominate the transport characteristics of this fluorene-phenoxazine copolymer. Among the possible determinants are polymer chain geometry, packing and magnitude of hole wavefunction overlap. Quantum chemical calculations [125, 126] have shown that the chain conformation of TFB is non-planar with a fluorene-triphenylamine dihedral angle

of 36° and a triphenylamine block which has coplanar central NCCC atoms and a propeller-like arrangement of phenyl rings with a CNCC dihedral angle of 40° (figure 5.7 (a)). Similar calculations for a model fluorene-phenoxazine copolymer [117] have also inferred non-planar chain conformation with torsional angles between adjacent fluorene and phenoxazine units of about 35° and a phenoxazine moiety bending in a butterfly-like shape across the line fixed by the oxygen and nitrogen atoms (figure 5.7 (b)). This suggests small molecular orbital overlap between the oxygen or nitrogen and the joint atoms. Based on these reported calculations we conclude that both copolymers have a non-planar chain conformations and likely poor intermolecular packing. The above referenced works [117, 125, 126] have also generated the electronic structure of the copolymers. For TFB the HOMO orbital is shown to fully delocalize over the conjugated backbone similar to PFO while the delocalization of the LUMO orbital is reduced upon the copolymerization of triphenylamine as nodes appear in the wavefunction on the nitrogen atoms [126]. In contrast, for the fluorene-phenoxazine copolymer the HOMO orbital is localized on the phenoxazine unit while the LUMO orbital is localized on the fluorene segment reducing the hole wavefunction overlap along the polymer chain [117]. Therefore, reducing the probability of hole charge carrier hopping required for transport. Lastly, we note one final potential factor affecting the observed large mobility difference between TFB and F8BPPOZ. Temperature dependent hole mobility measurements of TFB have shown that it possesses a narrow transport manifold with a width of $65.9 \pm 0.5\,\mathrm{meV}$ [80]. The polar nature of F8BPPOZ in contrast to the non-polar TFB can result in increased energetic disorder and lower mobility as a polar molecule would react more sensitively to variations in the dielectric polarization of its surrounding compared to a non-polar one. We propose that a temperature dependent mobility study of F8BPPOZ would provide useful information regarding this aspect and should constitute future work on the topic.

5.5 PLEDs

Organic light emitting diodes (OLEDs) are devices that consist of an active layer of organic semiconductor which emits light in response to an electric current. An OLED whose active layer is a conjugated polymer is termed a PLED. The simplest single-layer PLEDs are made up of a polymer active layer sandwiched between a cathode and an anode. Light is emitted when holes from the anode and electrons from the cathode combine radiatively in the light emitting polymer. For efficient PLED operation holes and electrons should be injected with as little bias as possible and each electron should recombine with a hole in the semiconductor rather than leaving at the counter electrode. Multi-layered device architectures can be employed to this end. Improved charge injection can be obtained by inserting injection layers between the emissive layer and the electrodes. Organic semiconductors with a HOMO (LUMO) in between the HOMO (LUMO) of the light emitting polymer and the work function of the anode (cathode) are commonly used. This graded energetic junction lowers the charge injection barrier and therefore leads to a lower turn-on voltage for light emission. Blocking layers are introduced to prevent the charges from leaving the light emitting polymer without recombination. For this materials with a high LUMO (low HOMO) are required between the injection layer and the emissive layer at the anode (cathode) side. A single material can combine both functions if it has suitable energy levels.

Common thin film PLEDs consist of a transparent indium tin oxide (ITO) anode which injects holes into the light emitting polymer via a hole injecting layer of PEDOT:PSS conducting polymer composite. PEDOT:PSS has been shown to improve device efficiency, lifetime and operating voltage in OLEDs [127, 128]. It does that by smoothing the rough ITO surface, therefore, preventing filamentary current injection that can cause short circuits. Additionally, PEDOT:PSS helps the adhesion of subsequent layers. It also improves hole injection by increasing the ITO work function from $\sim 4.6 - 4.8\,\text{eV}$ to $\sim 5.0 - 5.2\,\text{eV}$ [90–92]. The disadvantage of PEDOT:PSS is the acidic nature of PSS that can degrade the active layer. An

optional anodic interlayer can be inserted between PEDOT:PSS and the light emitting polymer to enhance performance. Efficiency can be significantly increased by forming a physical barrier that prevents the acidic PEDOT:PSS from degrading the light emitting polymer. The interlayer can also limit exciton quenching by the anode by moving the recombination zone away from ITO. Additionally, it can prevent electrons from travelling into PEDOT:PSS and improve hole injection. TFB has been shown to act as an effective interlayer for polyfluorene-based devices [114, 115, 129]. Finally, in PLEDs electrons are usually injected from a low work function metal cathode such as calcium.

The performance of F8BPPOZ as a hole injection layer (HIL) in fluorene-based thin film PLEDs was studied and compared to equivalent devices employing TFB and devices with no interlayer. The PLEDs' active layer consisted of an emissive blend of two conjugated fluorene polymers, namely, poly(9,9-dioctylfluorene) (PFO) and poly(9,9-dioctylfluorene-*alt*-bithiophene) (F8BT) in a blend ratio by weight of 95:5 (referred to in the text as 95PFO:5F8BT). This blend acts as a host-guest energy transfer system with efficient transfer from the PFO host to the F8BT guest [130]. Emission from F8BT peaks at 530 nm with a PLQE of 64% [131]. The electron affinities, E_a, ionization potentials, I_p, and electrical gaps, $E_g = I_p - E_a$, of F8BPPOZ, TFB, PFO and F8BT are listed in table 5.1.

5.5.1 PLED Fabrication

The following four device structures were tested:

(1) ITO/PEDOT:PSS/95PFO:5F8BT/Ca/Al

(2) ITO/PEDOT:PSS/TFB/95PFO:5F8BT/Ca/Al

(3) ITO/PEDOT:PSS/pristine F8BPPOZ/95PFO:5F8BT/Ca/Al

(4) ITO/PEDOT:PSS/annealed F8BPPOZ/95PFO:5F8BT/Ca/Al.

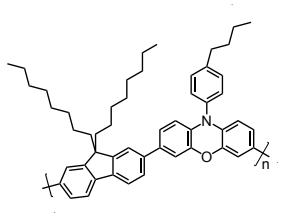
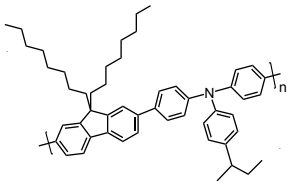
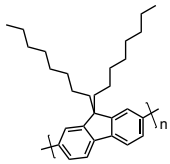
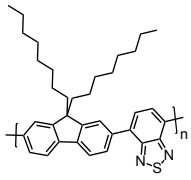
Material	Chemical structure	E_a (eV)	I_p (eV)	E_g (eV)	Reference
F8BPPOZ		2.1	5.1	3.0	This work
TFB		1.9	5.3	3.4	[78, 113, 132–134]
PFO		2.1	5.88	3.78	This work, [82, 100]
F8BT		3.3	5.9	2.6	[135–137]

Table 5.1: Material chemical structures, electronic energy levels and electrical gaps of F8BPPOZ, TFB, PFO and F8BT.

Commercial ITO-coated glass substrates with a typical resistance of $20\,\Omega\,\square^{-1}$ were employed. The substrates were cleaned using acetone and isopropyl alcohol by sequential sonication for 10 minutes. Then they were blown dry with nitrogen gas and subjected to a 10 minute UV ozone treatment. Next, a 40 nm thickness film of PEDOT:PSS (Clevios P VP AI 4083) was deposited by spin coating at 3000 rpm and then annealed in air for 20 minutes at 150 °C. All subsequent fabrication steps were performed in a dry nitrogen glovebox. For devices without an interlayer (1),

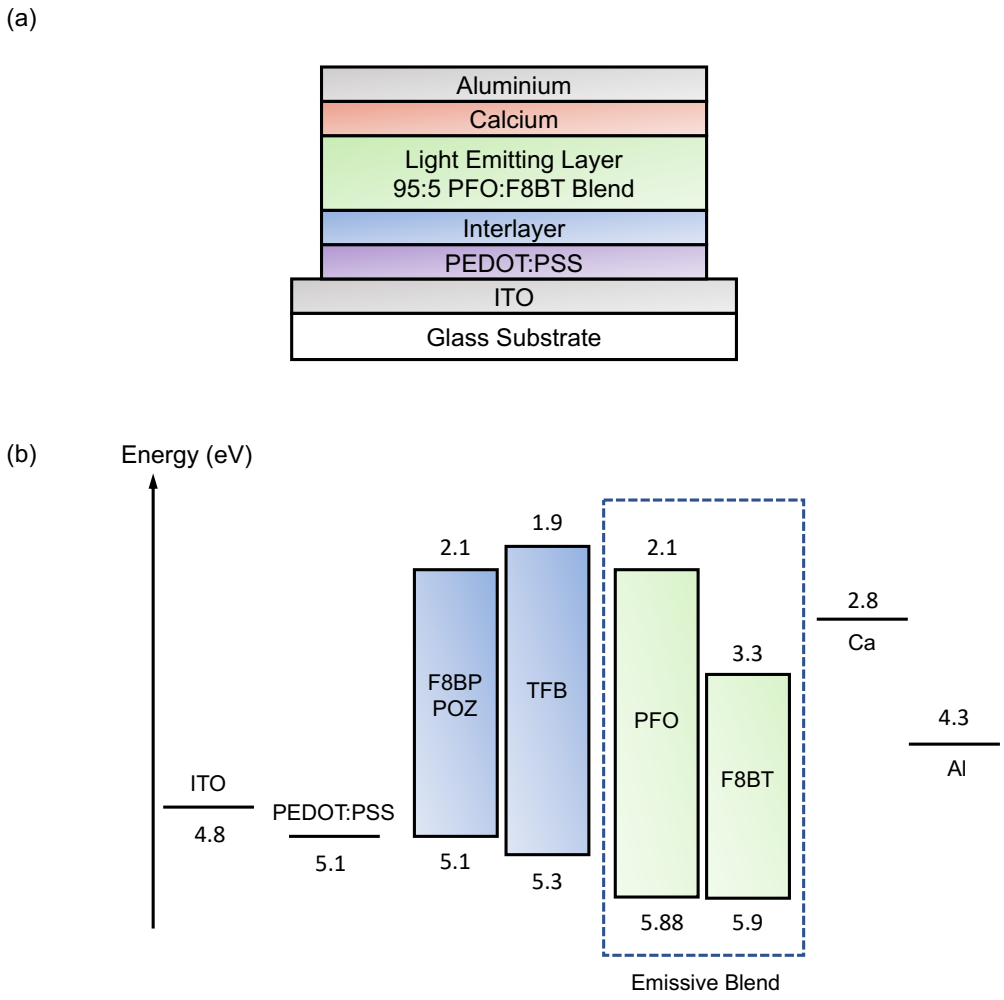


Figure 5.8: (a) PLED device structure and (b) the corresponding schematic energy level diagram. F8BPPOZ and TFB were used as interlayer materials, PLED devices without an interlayer were also fabricated.

a 80 nm layer of the emissive blend 95PFO:5F8BT was then spin coated on top of PEDOT:PSS from a toluene solution. This layer was thermally annealed at 80 °C for 10 minutes to dry off residual solvent. The devices were completed by thermally evaporating a 20 nm layer of calcium capped by 100 nm of aluminium. The evaporation took place in a thermal evaporator in a nitrogen atmosphere glovebox at pressures lower than 10^{-6} mbar. The pixels were defined by the spatial overlap of the anode and cathode and had an area of 25 mm^2. The devices were finally encapsulated using encapsulation glass with UV curable epoxy resin in the

glovebox without exposing to air. The interlayer devices (2) (3) (4) were fabricated in the same way except for a $10-15\,\text{nm}$ layer of TFB or F8BPPOZ deposited from toluene solution on top of the PEDOT:PSS. Since F8BPPOZ is a new material and its fabrication is not optimized, two different deposition approaches were tested. *Annealed F8BPPOZ* deposition followed the fabrication steps established for TFB. Annealed F8BPPOZ and TFB devices were thermally annealed in nitrogen at $180\,^{\circ}\text{C}$ for 60 minutes prior to the deposition of the emissive blend. This step is believed to prevent the interlayer material from being washed away or intermixing with the emissive layer when it is deposited on top from an organic solvent solution [138]. *Pristine F8BPPOZ* did not undergo the high temperature annealing step. The structure of the PLEDs is detailed in figure 5.8.

5.5.2 PLED Characterisation

The current-voltage-luminance (IVL) characteristics of the PLEDs with and without interlayers are shown in figure 5.9 (a). Below turn-on there is a weak leakage current due to parasitic currents between the electrodes via pinholes or other defects. PLEDs with annealed F8BPPOZ interlayers exhibit higher currents in this regime compared to the other PLEDs indicating increased shorting. The current threshold (defined as the voltage at which conduction through the semiconductor becomes more important than the short circuit currents) is $2.40\,\text{V}$ for devices without an interlayer, $2.27\,\text{V}$ for PLEDs with a TFB HIL, $2.28\,\text{V}$ for pristine F8BPPOZ HIL and $2.34\,\text{V}$ for annealed F8BPPOZ HIL (with an error of $\pm 0.15\,\text{V}$). The values were extracted from the intersection of straight line extrapolations of the IV curves around the current turn-on (figure 5.10). The onset of detectable light emission ($\sim 10\,\text{cd/m}^2$) is $2.62\,\text{V}$ for the PLEDs without a HIL, $2.48\,\text{V}$ for devices with a TFB layer, $2.58\,\text{V}$ for pristine F8BPPOZ HIL and $2.67\,\text{V}$ for annealed F8BPPOZ HIL PLEDs (with an error of $\pm 0.05\,\text{V}$).

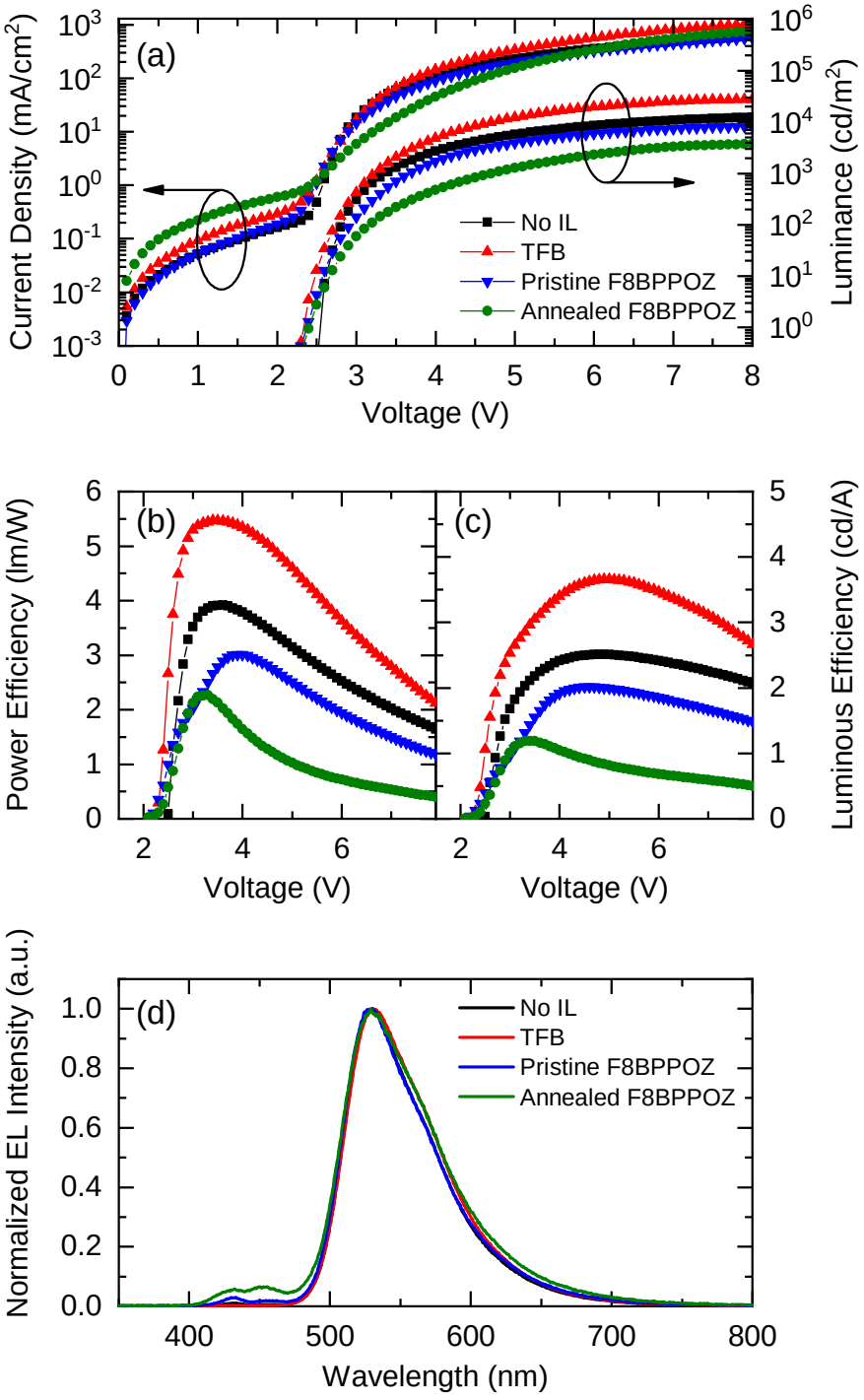


Figure 5.9: (a) Current-voltage-luminance (IVL) curves for PLEDs with no interlayer (black squares) and with TFB (red up pointing triangles), pristine F8BPPOZ (blue down pointing triangles) and annealed F8BPPOZ (green circles) interlayers. Efficiencies derived from the curves in (a) are shown in (b) lm/W and (c) cd/A. The peak normalized PLED EL spectra are presented in (d).

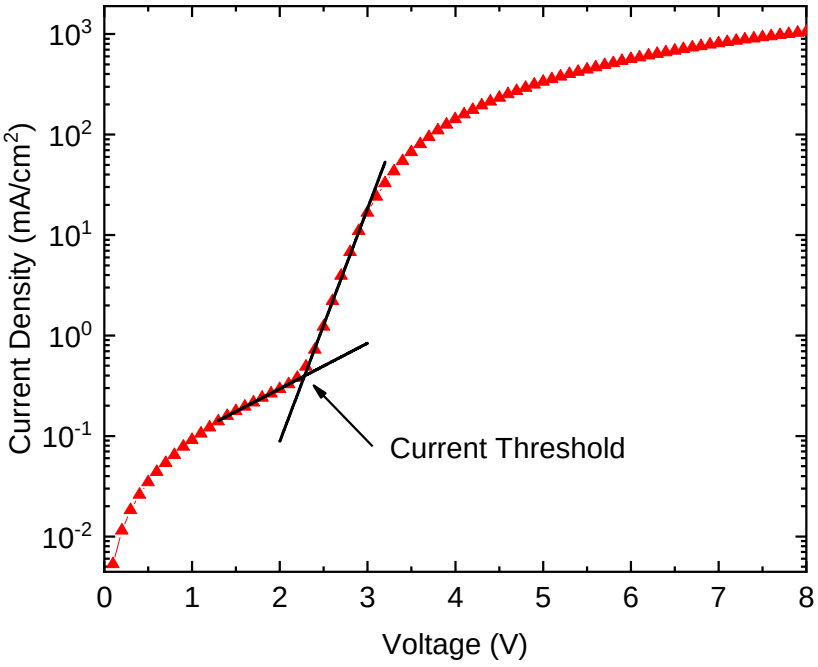


Figure 5.10: Current-voltage plot of PLED with TFB interlayer. The *current threshold* is extracted from the crossing point in voltage where the slow and fast increases of the current coincide.

The high current density regime above 100 mA/cm^2 is comparatively unaffected by changing the interlayer. In contrast the luminance varies by roughly one order of magnitude in the same voltage range. In comparison to PLEDs without an interlayer, the addition of a TFB layer raises the luminance while F8BPPOZ interlayers lead to a drop in luminance with the lowest values recorded for annealed F8BPPOZ. The power efficiencies and luminous efficiencies of the PLEDs calculated from the curves in figures 5.9 (a) are shown as a function of voltage in figures 5.9 (b) and (c), respectively. The maximum power efficiencies of the devices correlate with their maximum luminance values. The interlayer free PLED reaches 3.91 lm/W at 3.5 V. The efficiency increases considerably when a TFB interlayer is included between the PEDOT:PSS and the emissive layer, achieving 5.47 lm/W at 3.4 V. Pristine F8BPPOZ interlayer devices show a maximum efficiency of 3.02 lm/W at 3.9 V while annealed F8BPPOZ interlayer devices give 2.27 lm/W at 3.3 V, both

Hole Injection Layer	Current Threshold (V)	Luminance Threshold (V) ($L > 10\,cd/m^2$)	Maximum Power Efficiency (lm/W)	Voltage at Maximum Power Efficiency (V)
None	2.40	2.62	3.91	3.5
TFB	2.27	2.48	5.47	3.4
Pristine F8BPPOZ	2.28	2.58	3.02	3.9
Annealed F8BPPOZ	2.34	2.67	2.27	3.3

Table 5.2: Key device characteristics for PLEDs with and without interlayers.

lower than the devices without an interlayer. In all four devices the power and luminous efficiencies diminish with increasing voltage but the decline is steepest in the annealed F8BPPOZ PLEDs. Key performance characteristics for the four PLEDs are summarised in table 5.2.

The peak normalized electroluminescence spectra for the PLEDs are displayed in figure 5.9 (d). The spectra have a strong emission peak at 530 nm which originates from the F8BT moieties in the emissive blend [130, 131]. Further, there are two weak emission bands with peaks at 431 nm and 453 nm. These spectral features match the emission of PFO, therefore, we assign them to residual emission from PFO segments in the blend. The intensity of the residual PFO emission is highest for F8BPPOZ IL devices followed by the interlayer free devices. The PLEDs containing a TFB interlayer showed no residual PFO emission.

To rationalize the observed PLED device characteristics, the major interlayer parameters that determine device performance are discussed. Firstly, there is no barrier for hole injection from PEDOT:PSS to F8BPPOZ, however, there is a 0.8 eV barrier for hole transfer from F8BPPOZ to the emissive layer. In contrast, TFB provides a graded barrier which can improve hole injection into the emissive blend. Secondly, TFB provides superior electron blocking compared to F8BPPOZ with its 0.2 eV lower electron affinity, therefore, providing better suppression of electron leakage at the anode. Next, we note the difference in exciton blocking between the two interlayers. Bailey *et al.* [115] have demonstrated that the most important function of the TFB interlayer in increasing PLED efficiencies in F8BT devices is exciton blocking by means of the difference in the energy gap between the light

emitting polymer and the interlayer. F8BPPOZ should have an inferior performance in this aspect compared to TFB due to its smaller energy gap. The smaller energy gap of F8BPPOZ may favour exciton diffusion from PFO to the interlayer where excitons are likely quenched leading to a drop in luminance. We propose that this favourable exciton diffusion leads to large luminance losses due to electrode quenching of excitons near the anode and is the cause of the drop in efficiency of PLEDs with F8BPPOZ interlayers even when compared to devices without a HIL. Device simulations would be necessary to further explore these hypotheses. Finally, we note the difference in device performance between the two different fabrication protocols for F8BPPOZ - pristine and annealed. The devices with annealed F8BPPOZ interlayers exhibit higher leakage currents and lower efficiencies. The hole mobility of pristine and annealed F8BPPOZ films was measured using the DIT technique and the value did not change upon annealing, thus, excluding the possibility of a mobility drop leading to the differences in PLED performance. We suspect that this may be due to changes in the thin film morphology of the material upon thermal annealing such as increased roughness which can lead to pinholes and other defects. Further studies including atomic force microscopy (AFM) measurements of the films following varying deposition approaches would be required to confirm this.

In conclusion, when the PLED HIL was varied minimal changes in current densities were observed, however, there were large variations in luminance. Devices with a F8BPPOZ HIL showed inferior performance compared to PLEDs with a TFB HIL and devices without an interlayer. A combination of unfavourable hole injection barriers, electron blocking characteristics and exciton blocking properties likely lead to the observed poor performance of PLEDs with a F8BPPOZ HIL. Device improvements are strongly dependent on finding a compatible combination of interlayer material and light-emitting material. Therefore, we suggest that F8BPPOZ may be a good interlayer material in combination with different emissive layers. Poly(*p*-phenylene vinylenes) (PPV) materials such as Super Yellow may

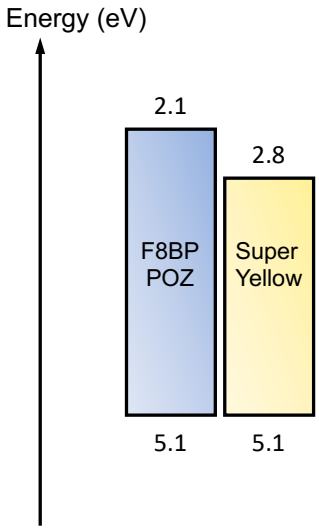


Figure 5.11: Schematic energy level diagram for F8BPPOZ and Super Yellow.

be good candidates due to their favourable energy levels relative to F8BPPOZ [3] (figure 5.11).

5.6 Polymeric Semiconductor Heterojunctions

The heterojunction formed in blends of F8BPPOZ and F8BT is studied and compared to the heterojunction in blends of TFB and F8BT. Both blends form type II heterojunctions where both the electron affinity and ionization potential are higher in one material than in the other (figure 5.12). This configuration is commonly used as the active semiconducting layer in light emitting diodes and photovoltaic devices [140–143]. Blends of TFB:F8BT have demonstrated excellent LED performance and have been used as emissive layers in PLEDs [144–146]. In contrast, for efficient photovoltaic behaviour semiconductors with larger band-edge offsets leading to charge separation at the interface are required.

[3] The energy levels of Super Yellow are reported at −5.1 eV and −2.8 eV for the HOMO and LUMO, respectively [139].

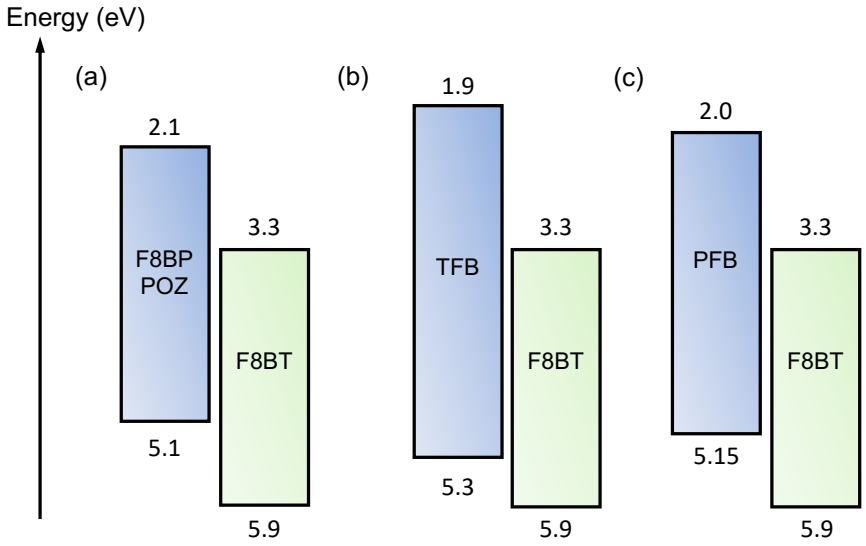


Figure 5.12: Schematic energy level diagram for heterojunction formed between (a) F8BPPOZ and F8BT, (b) TFB and F8BT and (c) PFB and F8BT.

In this work, polymer blends (mass ratio 1:1) were spin coated from a common toluene solution onto quartz substrates to form 70 nm films. The peak normalized PL spectra of the two blends as well as a reference F8BT film are displayed in figure 5.13. The PLQE values measured for the films are presented in table 5.3. The measurements were performed at room temperature in ambient air using a 457 nm excitation. This wavelength was chosen as it is near the peak of the F8BT absorption [147] while F8BPPOZ and TFB [148] absorb weakly at this value. The TFB:F8BT blend spectrum closely matches the pure F8BT PL, therefore, we conclude that the blend emission originates primarily from F8BT excitons. Yet, the F8BPPOZ:F8BT spectrum exhibits a broad red shifted emission with a peak at 620 nm. The PLQE values for the two blends are also significantly different with a value of 39% for the TFB:F8BT blend compared to only 4% for F8BPPOZ:F8BT.

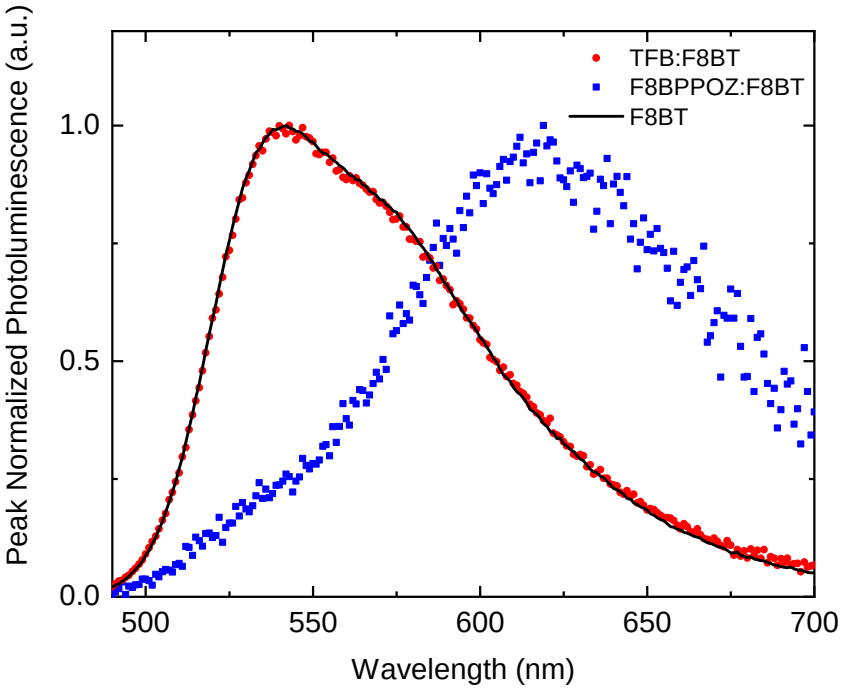


Figure 5.13: Thin film peak normalized photoluminescence spectra for TFB:F8BT (red circles) and F8BPPOZ:F8BT (blue squares) blends as well as a reference F8BT film (black line) excited using a 457 nm excitation.

Material	PLQE (%)
F8BT	63
TFB:F8BT	39
F8BPPOZ:F8BT	4

Table 5.3: Photoluminescence quantum efficiencies in thin films of F8BT, TFB:F8BT and F8BPPOZ:F8BT. The experimental error on the values is ±5%.

Studies of excitation dynamics at type II polymeric semiconductor heterojunctions [145, 146] have shown that in all blends excitons initially dissociate at the heterojunction and form an interfacial geminate charge pair. However, geminate pair recombination via an intermediate exciplex can regenerate the bulk exciton and lead to high photoluminescence yield. Morteani *et al.* [146] proposed that when the system is photoexcited an exciton is generated some distance away from the interface. It can subsequently diffuse and encounter the heterojunction where it would dissociate into an interfacial geminate electron-hole pair. The geminate

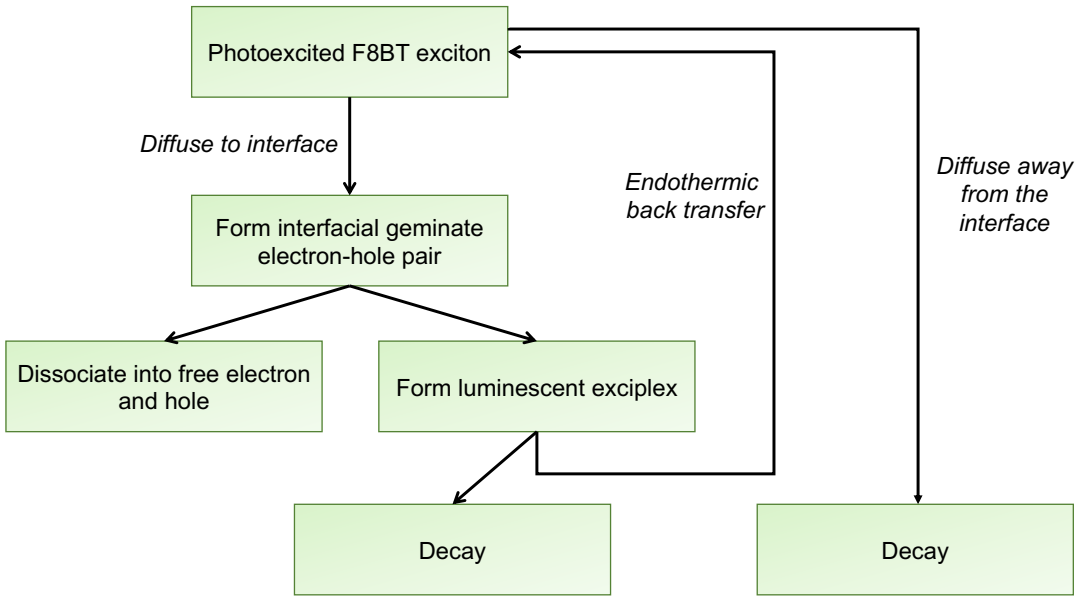


Figure 5.14: Schematic illustration of exciton quenching and regeneration at TFB:F8BT and F8BPPOZ:F8BT heterojunctions.

pair can then either dissociate into a free electron and hole or form a luminescent exciplex. The ratio of these two processes determines the luminescence quenching. If an exciplex is formed, it can either decay or back transfer to a bulk exciton. The regenerated bulk exciton can subsequently either enter the cycle again or diffuse away from the interface and decay. This sequence is schematically illustrated in figure 5.14. Therefore, the steady state blend PL consists of three components: (i) "primary" excitons generated in the bulk by the laser excitation; (ii) exciplexes generated by energy transfer from bulk excitons at the interface; and (iii) "secondary" excitons formed by endothermic back transfer from the exciplexes. Despite charge transfer taking place at the interface, the excitation can still decay via bulk exciton luminescence. In TFB:F8BT blends it has been found that the contribution of "primary excitons" is less than 2% with more than 98% of excitons undergoing charge transfer at the heterojunction [145]. However, due to efficient exciton regeneration the PL yield of the blend is still high. The critical factors determining the transitions between the different excited states at the heterojunctions have been proposed to be the geminate pair separation and the back transfer activation energy of the

blend. Both are expected to increase for larger band-edge offsets between the two polymers [146]. Therefore, we would anticipate that for the case of F8BPPOZ:F8BT the regeneration mechanism would be much less efficient due to higher geminate pair separation and back transfer activation energy compared to TFB:F8BT. To measure the geminate pair separation and the back transfer activation energy of the blend electric field dependent PL spectroscopy and its temperature dependence would need to be investigated. We speculate that in the F8BPPOZ:F8BT blend most of the interfacial geminate electron-hole pairs dissociate with few forming emissive exciplexes that decay radiatively leading to the observed PL spectrum. This situation is potentially desirable for photovoltaic operation.

The results for F8BPPOZ:F8BT are strikingly similar to observations made for blends of poly(9,9-dioctylfluorene-*alt*-bis-N,N'-(4-butylphenyl)-bis-N,N'-phenyl-1,4-phenylenediamine) (PFB) and F8BT where a PLQE value of 4% has been reported and ascribed to low regeneration efficiency due to large geminate pair dissociation and low back transfer efficiency. Also, an exciplex state at the PFB:F8BT heterojunction has been identified $\sim 625\,\text{nm}$ in the blend's PL emission [146]. PFB has an ionization potential of $5.15\,\text{eV}$ [4] and electron affinity of $2.0\,\text{eV}$ [82], these values are very similar to the values obtained for F8BPPOZ and, thus, similar heterojunction dynamics are likely to be at work. PFB:F8BT blends have been employed in photovoltaic diodes [149, 150]. Additionally, the effect of blend morphology and phase separation on the emission properties of F8BPPOZ:F8BT blends would be an interesting avenue for future work.

Finally, we note that charge separation at the heterojunction between F8BPPOZ and F8BT in the PLED devices studied earlier is not expected. The ionization potential of F8BT is lower than the ionization potential of F8BPPOZ and the electron-hole pair would have its hole situated on the interlayer and its electron located on F8BT, therefore, exciton dissociation would be energetically unfavourable

[4] This value was measured in chapter 4 section 4.4 and is in agreement with literature [78].

as the holes would need to move towards the anode and the electrons towards the cathode. Nevertheless, the heterojunction dynamics can still reduce the luminescence efficiency of the PLEDs by blocking energy transfer from PFO to F8BT in the light emitting blend if F8BT excitons at the interface between the emissive layer and the F8BPPOZ interlayer form stable geminate electron-hole pairs. This would result in increased residual PFO emission as observed for devices with a F8BPPOZ IL. Therefore, the formation of stable interfacial electron-hole pairs can quench the F8BT emission and be among the factors leading to the poor device performance of PLEDs employing a F8BPPOZ IL.

5.7 Conclusions

In summary, a new polyfluorene-phenoxazine alternating copolymer, F8BPPOZ, has been characterised. This copolymer has a similar structure to the widely used hole transporting polymer, TFB, however, it is expected to have a more rigid backbone due to the POZ ring reducing the number of torsions of the polymer chain. This is supported by DSC measurements showing a glass transition temperature of $196 \pm 4\,^{\circ}\mathrm{C}$, which is higher than both TFB ($140\,^{\circ}\mathrm{C}$ [123]) and the fluorene homopolymer PFO ($50\,^{\circ}\mathrm{C}$ [122]). F8BPPOZ has a red shifted emission compared to PFO with low PLQE suggesting charge transfer character. Further, the incorporation of the phenoxazine polymer into a polyfluorene backbone lowers the ionization potential of the copolymer to $5.1 \pm 0.05\,\mathrm{eV}$ via the electron rich oxygen and nitrogen heteroatoms. Therefore, the POZ unit significantly improves the hole accepting properties of the copolymer compared to the homopolymer, PFO ($5.88 \pm 0.05\,\mathrm{eV}$). Finally, despite increased rigidity being advantageous for charge transport, the hole mobility value for F8BPPOZ extracted from DIT measurements is $7 \times 10^{-4}\,\mathrm{cm^2V^{-1}s^{-1}}$ at an electric field of $5 \times 10^5\,\mathrm{V\,cm^{-1}}$ which is only slightly higher than PFO ($4 \times 10^{-4}\,\mathrm{cm^2V^{-1}s^{-1}}$ [4, 42, 99]) and at least an order of magnitude lower than values reported for TFB ($(5-10) \times 10^{-3}\,\mathrm{cm^2V^{-1}s^{-1}}$ [79, 80]). Therefore, we conclude that in the case of F8BPPOZ, the incorporation of the more rigid

POZ molecule does not improve hole transport compared to TFB and other factors must be dominating. Quantum chemical calculations have shown that in a model fluorene-phenoxazine copolymer the HOMO orbital is localized on the phenoxazine unit while the LUMO orbital is situated on the fluorene moiety [117], therefore, reducing the hole wavefunction overlap along the polymer chain. This would lower the probability of hole charge carrier hopping required for transport. Additionally, the polar nature of F8BPPOZ can lead to increased energetic disorder of the transport sites and lower mobility. In contrast, for the non-polar TFB a narrow transport manifold has been inferred from temperature dependent hole mobility measurements [80]. Further studies including an investigation of the temperature dependence of hole transport would be necessary to explore the critical material characteristics that influence the hole mobility of F8BPPOZ.

Subsequently, the F8BPPOZ copolymer's performance as HIL in thin film 95PFO:5F8BT blend PLEDs was evaluated and compared to devices with a TFB interlayer and no interlayer. When the PLED HIL was varied minimal changes in current densities were observed, however, there were large variations in luminance. Devices with a F8BPPOZ HIL showed inferior performance compared to PLEDs with a TFB HIL and even devices without an interlayer. A combination of unfavourable hole injection barriers, electron blocking characteristics and exciton blocking properties likely lead to the observed poor performance of PLEDs with a F8BPPOZ HIL.

Also, the emission characteristics of semiconductor heterojunctions formed for 1:1 blends of F8BPPOZ:F8BT and TFB:F8BT were compared. PL and PLQE measurements of a F8BPPOZ:F8BT blend demonstrated strong photoluminescence quenching in the blend compared to TFB:F8BT blends and pure F8BT. The F8BPPOZ:F8BT blend emission centered $\sim 620\,\mathrm{nm}$ was assigned to an interfacial exciplex state due to its broad red shifted spectrum compared to both blend materials. Studies in the literature [145, 146] have proposed that in all type II heterojunction

blends, the exciton first dissociates at the interface and forms a geminate charge pair yet geminate pair recombination via an intermediate exciplex can regenerate the bulk excitons. In TFB:F8BT blends effective F8BT exciton regeneration leads to high PLQE (39%). The quenching in F8BPPOZ:F8BT blends (PLQE 4%) was proposed to result from efficient geminate pair dissociation at the interface between the two polymers. High charge separation yields are advantageous in solar cell applications and, therefore, this material combination may be better suited for photovoltaic devices. Despite charge separation at the heterojunction between F8BPPOZ and F8BT in the PLED devices studied being energetically unfavourable due to the anode being situated on the F8BPPOZ side, the heterojunction can still quench the F8BT emission by blocking energy transfer from PFO to F8BT in the light emitting blend if F8BT excitons at the interface between the emissive layer and the F8BPPOZ interlayer form stable geminate electron-hole pairs. Therefore, we suggest that the formation of stable interfacial electron-hole pairs at the heterojunction between F8BT and F8BPPOZ can be among the factors leading to the poor device performance of PLEDs employing a F8BPPOZ IL.

6

Platinum-complex Copolymerisation

This chapter presents the spectroscopic characterisation of a series of Pt-containing polyfluorene copolymers within which the platinum atom is introduced through a cyclometalated PyTPAPt(acac) complex embedded into the backbone of the light emitting polymer PFO. The content of this complex has been varied from 0.5% *to* 5%*. The heavy platinum atom increases the spin-orbit coupling in these compounds leading to the radiative decay of the triplet state. For reference the corresponding organic PyTPA ligand copolymers are studied alongside. It is found that the copolymers are able to adopt both the glassy and* β *phase chain conformations characteristic of PFO. The phosphorescence spectral diffusion in the two phases of the* 5% *platinum copolymer is compared to give information about the triplet exciton transfer in disordered polymer films with different conjugation lengths.*

6.1 Introduction

Triplet states play a vital role in the operation of organic semiconductor devices and can strongly affect their performance. For example, LED efficiency is determined by the fraction of injected electrons and holes that recombine to form an emissive state. Since the triplet state in conjugated polymers is weakly emissive due to its spin-forbidden transition to the ground singlet state, this places a limit on device efficiency.

In recent years, LEDs harvesting triplet emission using organometallic complexes in combination with organic molecules as emitting semiconductors have gained scientific interest [151–153]. However, triplet diffusion leading to triplet-charge annihilation (TCA) and triplet-triplet annihilation (TTA) can lead to efficiency roll-off at high current densities in such phosphorescent LEDs [154–156]. Triplet diffusion is also critical for devices based on TTA-induced delayed fluorescence for non-resonant upconversion of low energy incident red light into high energy blue emission [157–159]. Therefore, a thorough understanding of the material parameters that govern triplet diffusion is needed for the advancement of such devices.

The study of triplet states is particularly difficult due to their nonemissive nature. To detect emission directly from the triplet state it is necessary to make use of spin-orbit coupling. Phosphorescence does occur in almost all conjugated polymers due to intrinsic spin-orbit coupling but the emission intensity is extremely weak and very sensitive detection is needed to observe it. However, using heavy atom induced spin-orbit coupling triplet emission can be detected with conventional spectroscopic measurements. The incorporation of a heavy atom such as platinum into the carbon backbone of a polymer can provide enough spin-orbit coupling leading to enhanced triplet emission.

6.2 Materials

The materials investigated in this study are a series of copolymers based on the light emitting polymer PFO. These comprise varying amounts (0.5, 1, 2.5 and 5%) of cyclometalated PyTPAPt(acac) complex or the corresponding organic PyTPA ligand embedded into a PFO backbone. The chemical structures of the copolymers are shown in figure 6.1. Further material details including average molecular weight, polydispersity index and synthetic routes are presented in appendix B section B.1. Interest in such compounds stems from the large enhancement in spin-orbit coupling induced by the heavy platinum atoms making triplet emission partially allowed.

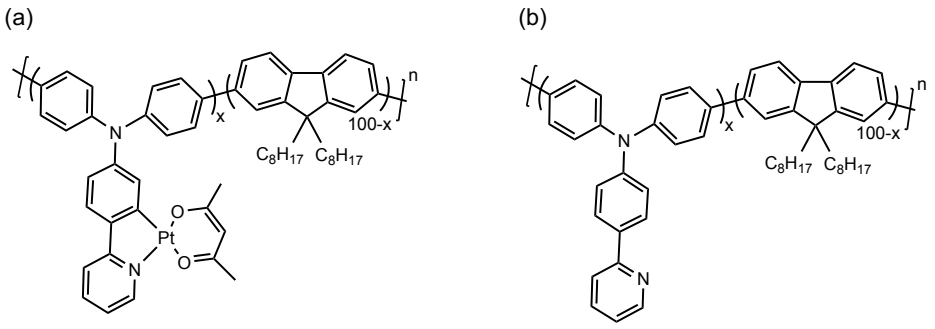


Figure 6.1: Chemical structures of the investigated polyfluorene copolymers with (a) cyclometalated PyTPAPt(acac) complex and (b) organic PyTPA ligand ($x = 0.5$, 1, 2.5 and 5%).

Meanwhile, the distinct glassy and β phases of PFO enable the study of triplet transport as a function of energetic disorder and conjugation length using the same compound without the need for chemical modification. The materials have been kindly provided by the research group of Professor Youtian Tao at Nanjing Tech University. Xuyu Gao from Professor Youtian Tao's group has provided us with the absorption and photoluminescence spectra of the cyclometalated PyTPAPt(acac) complex and organic PyTPA ligand monomers. The spectra are displayed in appendix B section B.2.

Throughout the rest of this chapter the copolymers are referred to as $n\%$ *Pt* or $n\%$ *ligand*, where $n\%$ stands for the percentage of the incorporated unit, *Pt* refers to the platinum metal-ligand (PyTPAPt(acac)) complex containing copolymers and *ligand* is used for the copolymers containing the organic ligand (PyTPA) only. Also, PFO purchased from 1-Material has been measured alongside for reference. Thin films of the materials were investigated and all solution preparation and film fabrication took place in a dry nitrogen glovebox. The preparation of glassy phase and β phase containing films has been described in detail in chapter 3 section 3.1.1. In short, for the fabrication of glassy phase films both solutions and substrates were placed on a hot plate at 100 °C for 5 minutes immediately prior to spin coating. Such samples are referred to as *hot spun* in the text. For fabricating β phase

containing films postdeposition swelling of the glassy films was employed. This was done by exposing the hot spun films to toluene vapour at room temperature for 12 hours. These films are called *solvent vapour annealed* in the text.

6.3 Absorption

The peak normalized thin film absorption spectra of all the copolymers under study as well as a reference PFO homopolymer are presented in figure 6.2 (a) for the hot spun films and in figure 6.2 (b) for the solvent vapour annealed films. The copolymer absorption spectra closely resemble the PFO spectrum and, therefore, are assigned primarily to absorption of the polyfluorene chromophore. Furthermore, the ligands and metal-ligand complexes do not inhibit the planarisation of the PFO chains and all copolymers are able to form the β phase as evident by the additional absorption peak at 2.86 eV appearing in all the spectra in figure 6.2 (b).

In the Pt copolymers' spectra an additional low intensity absorption feature appears around 2.8 eV which is not present in the ligand copolymers and PFO homopolymer spectra. This is more clearly visible in the hot spun films since in the solvent vapour annealed films it is obscured by the β phase absorption peak. This feature correlates with platinum content and it is most pronounced for the 5% Pt copolymer. Therefore, we assign it to absorption of the metal-ligand complex. In order to examine this spectral contribution further we have subtracted the peak normalized hot spun 0.5% Pt copolymer film absorption from the peak normalized hot spun 5% Pt spectrum. The result is displayed in figure 6.3. This difference spectrum coincides with the low energy absorption peak of the metal-ligand complex as seen from the thin film absorption spectrum of the PyTPAPt(acac) monomer presented in figure B.4 of appendix B. We suspect the origin of this absorption is a metal-to-ligand charge transfer (MLCT) transition. MLCT transitions take place from an orbital centred on the metal, typically a metal *d*-orbital, to a LUMO orbital centered on the ligand, usually a π^* orbital [7]. The reduced overlap between

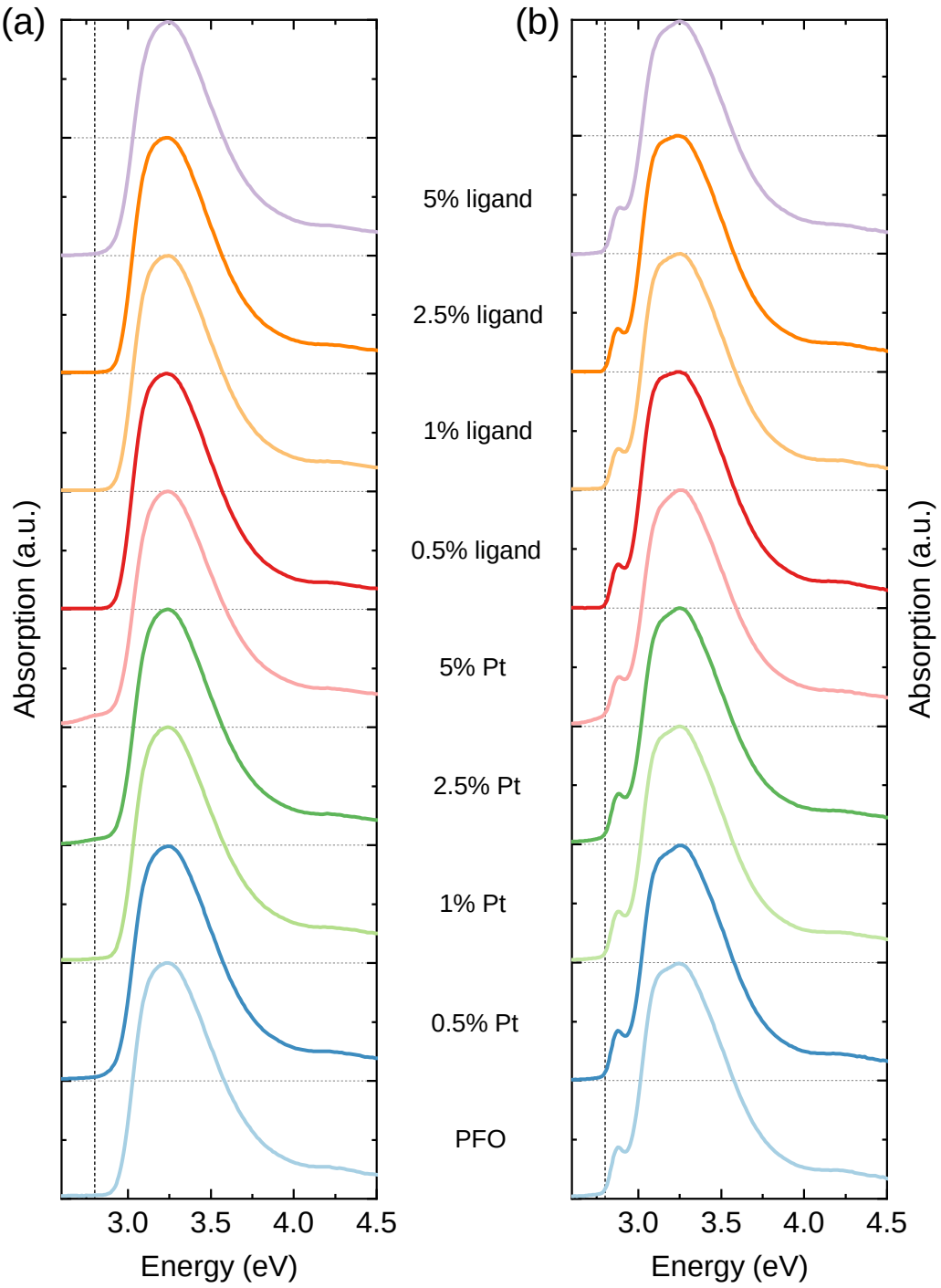


Figure 6.2: The thin film absorption spectra of (a) hot spun films and (b) solvent vapour annealed films of the copolymers and PFO. The spectra have been peak normalized and displaced along the vertical axis for ease of comparison. The vertical dashed lines are drawn at 2.8 eV.

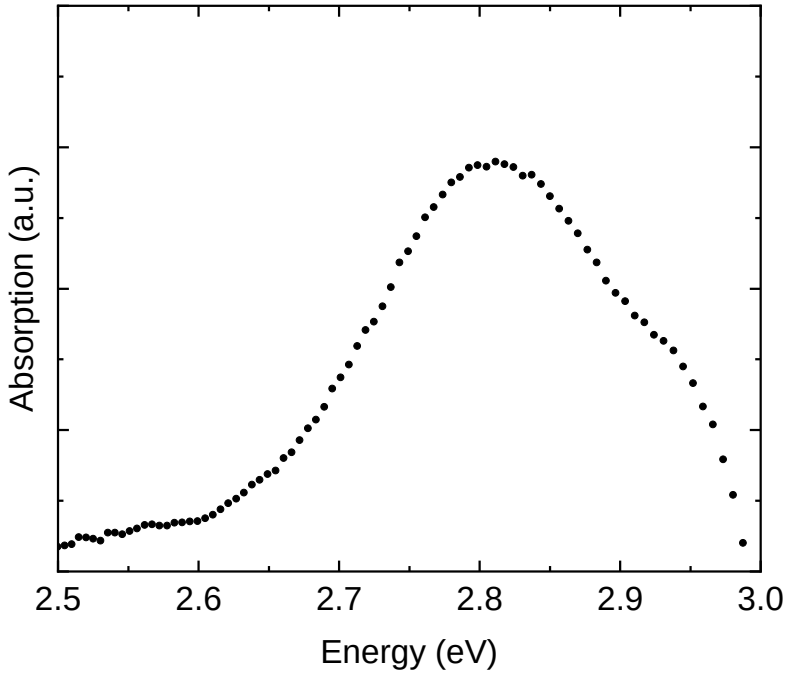


Figure 6.3: The absorption contribution of the PyTPAPt(acac) complex in the Pt copolymer absorption spectrum (as derived from a numerical subtraction of the peak normalized hot spun 5% and 0.5% Pt copolymers absorption spectra).

the initial and final state wavefunctions due to the occupied d-orbital and LUMO being located on different regions of the molecule result in the lower intensity of such transitions compared to $\pi - \pi^*$ transitions. Similar absorption features have been reported for other heavy metal containing polyfluorenes [160, 161].

In conclusion, we have shown that the incorporation of as much as 5% of a platinum containing metal-ligand complex into the backbone of PFO does not impede the formation of the β phase chain conformation of PFO. We have also characterised the spectral features related to the cyclometalated platinum complex.

6.4 Photoluminescence Spectroscopy

The thin film photoluminescence (PL) spectra of the copolymers were measured at various temperatures. First, the room temperature PL and photoluminescence quantum efficiency (PLQE) were assessed in ambient air using a 3.2 eV light excitation. The same films as for the absorption measurements were studied. The PL spectra for both the hot spun and solvent vapour annealed films are shown in figure 6.4. The spectra are area-normalized for better comparison of the redistribution of emission intensity in the various copolymers. The corresponding PLQE values are given in table 6.1.

Two spectral contributions can be distinguished in the PL of the copolymers: the structured blue PFO emission band between 3.0 and 2.5 eV and a broad featureless yellow band between 2.5 and 2.0 eV. In all emission spectra, the characteristic spectral features of the respective PFO conformations are observed. The only discrepancy in the emission peak positions between PFO and the copolymers occurs for the hot spun films of the 0.5% Pt and the 5% ligand copolymers. There the emission peaks are red shifted relative to the PFO glassy emission suggesting the presence of small fractions of β phase chain segments. Since the formation of glassy films requires rapid solvent evaporation during film deposition we suspect that the formation of β phase has resulted from either the solution or substrate not being hot enough just before spin coating allowing a slowing down of the kinetics of film formation.

The low energy yellow band increases with increasing platinum and ligand content while the polyfluorene fluorescence decreases. We suspect that there are several emission contributions here that overlap spectrally. Firstly, we speculate that the origin of part of this low energy yellow emission are charge transfer (CT) transitions on the ligand and metal-ligand units. MLCT transitions on the metal-ligand complex have already been touched upon in section 6.3. The ligand structure itself also favours CT states due to the combination of the electron rich

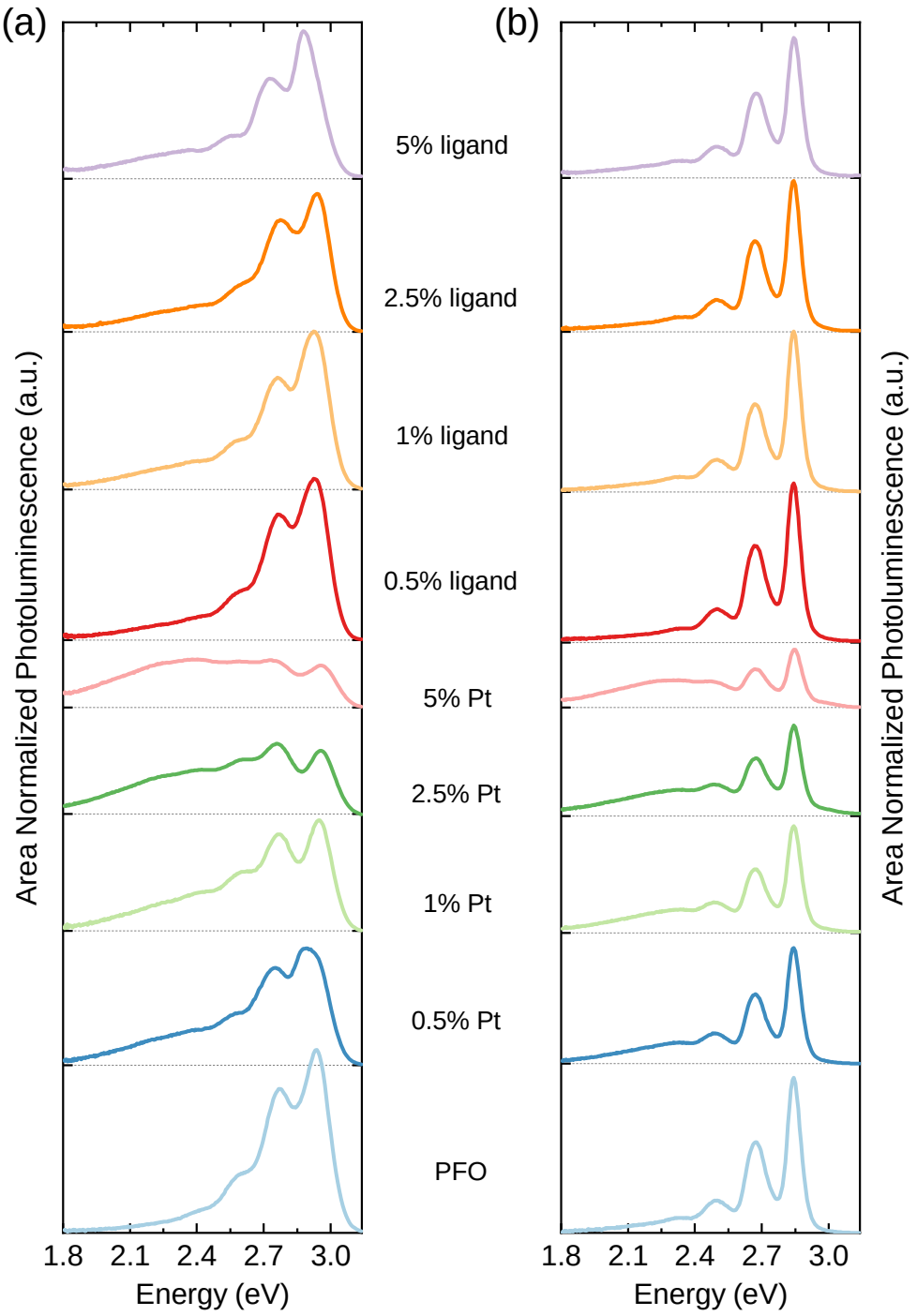


Figure 6.4: The thin film area-normalized PL spectra of (a) hot spun films and (b) solvent vapour annealed films of the copolymers and PFO. The spectra have been offset along the vertical axis for clarity.

arylamine on one end and the electron deficient pyridine on the other. This is futher supported by the observation of emission centred $\sim 2.3\,\text{eV}$ for thin films of both the cyclometalated PyTPAPt(acac) complex and the organic PyTPA ligand monomers (appendix B figure B.5). Secondly, this emission is also consistent with keto defects being populated by polyfluorene singlets via thermally activated exciton migration, therefore, quenching the PFO fluorescence [31]. Keto defects are often found in polyfluorenes where the covalent C9 bridge is vulnerable to photooxidation and can result in the formation of a fluorenone unit in the place of a fluorene. The prolonged optical characterisation in air could have led to partial photooxidation of the films. Nevertheless, over a period of hours no significant changes were observed.

We also note the lack of phosphorescence in the room temperature PL spectra of the Pt copolymers despite the increased spin-orbit coupling induced by the presence of the heavy metal atoms. This is consistent with the fact that at higher temperatures thermally activated triplet motion leads to nonradiative decay at quenching sites [162]. One particular quencher that could strongly affect the triplet emission in these measurements is molecular oxygen since the spectral characterisation was performed in ambient air. Molecular oxygen can interact with the triplet state resulting in quenching and the formation of singlet oxygen as discussed in chapter 2 section 2.10. Singlet oxygen is chemically aggressive and may attack the π-bonds in organic semiconductors leading to a reduction of the luminescence efficiency.

Finally, we comment on the measured PLQE values presented in table 6.1. The values obtained for the reference PFO films are in good agreement with previously reported measurements [3, 85, 119]. The β phase PFO film has a slightly higher PLQE which has been understood on the basis of changes in the nonradiative decay paths rather than the radiative decay rate for the different microstructures [119]. Emission quenching of the copolymer luminescence is observed with increasing platinum and ligand content. A number of factors are expected to be at play. Firstly, transition rates between orbitals that are centred on the same part of a molecule

Material	PLQE (%)	
	Hot Spun	Solvent Vapour Annealed
PFO	45	50
Pt 0.5%	4	9
Pt 1%	2	6
Pt 2.5%	1	2
Pt 5%	1	1
Ligand 0.5%	17	37
Ligand 1%	11	26
Ligand 2.5%	9	25
Ligand 5%	7	16

Table 6.1: Photoluminescence quantum efficiency in thin films at room temperature of the copolymers under study and PFO.

(such as $\pi - \pi^*$ transitions) are larger than transition rates between orbitals that occupy different spaces such as CT transitions [7]. Therefore, the copolymerisation of the ligand and metal-ligand units with their associated CT transitions into the PFO backbone can lead to a decrease of PLQE as a result of exciton trapping and decay at the cyclometalated complex or organic ligand sites. Secondly, keto defect formation is also expected to lead to a decrease of the PL yield [163]. Additionally, we note that the formation of β phase chain segments in both copolymers leads to more efficient emission. We propose this is due to β phase chain segments acting as radiative exciton traps, therefore, limiting excited state migration to nonradiative decay sites. Finally, we suggest the dramatic quenching observed for the Pt copolymers implies that there is indeed enhanced spin-orbit coupling thanks to the incorporation of the heavy platinum atoms. Increased spin-orbit coupling will decrease the fluorescence quantum yield due to the improved intersystem crossing rate competing with the radiative transition rate for singlet excited states. At high temperatures and in air the triplet excitons formed as result of intersystem crossing will be nonemissive, therefore, leading to a reduction in PL efficiency.

In conclusion, the dramatic drop in PLQE upon the copolymerisation of the metal-ligand complexes implies enhanced intersystem crossing leading to the formation of triplet excitons at the expense of singlets. No triplet emission is

detected at room temperature due to efficient triplet migration to quenching sites.

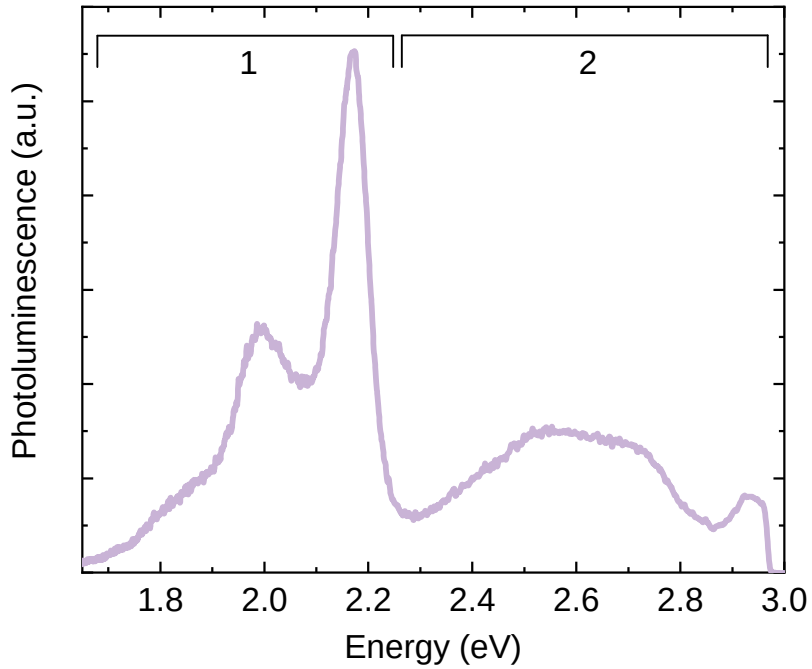


Figure 6.5: The photoluminescence spectrum of a hot spun film of the 5% Pt copolymer at 5 K.

Next, the 5 K photoluminescence spectra of a selection of the copolymers are discussed. Fresh samples were fabricated for this investigation. The samples were only in brief contact with air when being placed in the cryostat. A 3.15 eV laser excitation was used for all subsequent measurements. The photoluminescence spectrum of a hot spun film of the 5% Pt copolymer is shown in figure 6.5. In this spectrum a new low energy emission band is observed (labelled 1 in figure 6.5). This band exhibits a vibronic structure with two clearly resolved peaks and a shoulder on the red end of the emission. We attribute this emission to glassy PFO phosphorescence. The dominant vibronic peak is located at 2.17 eV. This lies ~ 0.7 eV below the 0-0 emission of the glassy PFO fluorescence in agreement with studies of the $S_1 - T_1$ gap in conjugated polymers [15, 164]. Furthermore, the spectrum is consistent with data reported for the phosphorescence of a similar

polyfluorene, namely PF2/6 [31, 165–167]. We identify the two emission peaks in the phosphorescence as the 0-0 and 0-1 $T_1 \rightarrow S_0$ transitions (since their spacing (170 meV) is consistent with the separation of vibronic transitions in fluorescence). We note that the 0-0 fluorescence emission ~ 2.93 eV is partially obscured by the long-pass edge filter (50% edge at 2.97 eV) included to remove residual excitation light from the collection path as described in chapter 3 section 3.1.5. We were unable to measure the low temperature glassy phase spectra of the remainder of the copolymers as all hot spun films showed significant β phase formation. We suspect that this is a result of thermal stress generating β phase segments in the hot spun films. Cadby *et al.* have shown that thermal cycling of spin-cast PFO films leads to the fomation of the β phase [85]. The 5% Pt copolymer has the highest fraction of the comonomer, therefore, we expect that it would be the most resilient to formation of the β phase under thermal stress.

We now compare the low temperature PL spectra of the solvent vapour annealed Pt copolymer films. The spectra measured at 5 K are displayed in figure 6.6 (a) alongside the spectrum of the 5% ligand copolymer and the PFO homopolymer for reference. The room temperature spectra of these samples measured at 10^{-6} mbar pressure inside the cryostat are shown in figure 6.6 (b) for comparison. With increasing platinum content a new low energy emission feature (labelled 1 in figure 6.6 (a)) appears at low temperature with a peak at 2.09 eV. The position of this emission once again lies about 0.7 eV below the 0-0 emission in fluorescence and coincides with previous reports of the triplet state position of β phase PFO [166]. Therefore, we assign this emission to radiative decay of the β phase PFO triplet. The appearance of this phosphorescence emission is in accord with the strong spin-orbit coupling of the heavy platinum atoms making the formally forbidden radiative relaxation of the triplet state partially allowed. This is also in agreement with the absence of phosphorescence emission from the PFO homopolymer and the 5% ligand samples where no heavy atoms are present.

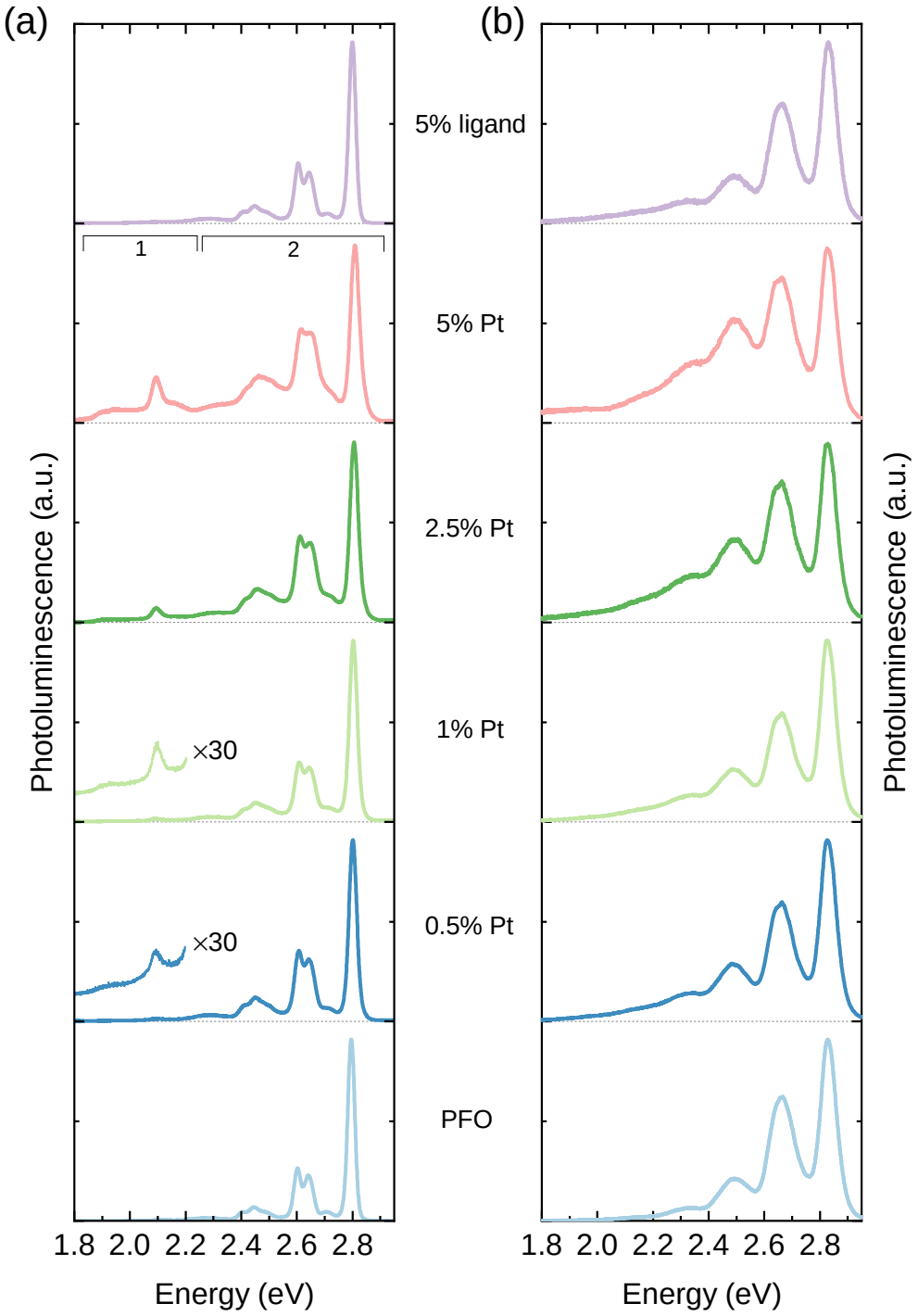


Figure 6.6: The photoluminescence spectra of solvent vapour annealed films of the Pt copolymers, the 5% ligand copolymer and PFO at (a) 5 K and (b) 300 K. The spectra have been normalized and displaced along the vertical axis for ease of comparison.

Additionally, the β phase fluorescence emission (labelled 2 in figure 6.6 (a)) gains vibrational resolution (reduced vibrations of surrounding medium reduce the inhomogeneous broadening of transitions) at low temperature. The peaks at 2.66 eV and 2.49 eV each split into (at least) three peaks in good agreement with literature [5, 49, 166]. Upon cooling the fluorescence is red shifted. The redshift is strongest for PFO and weakest for the 5% Pt copolymer. This phenomenon will be discussed in section 6.5 in terms of the temperature dependence of the electronic relaxation process and the exciton lifetime. Also, we note that from the room temperature PL spectra shown in figure 6.6 (b), it can be seen that the low energy yellow emission band ~ 2.3 eV is reduced significantly compared to the initial measurements performed in air (figure 6.4) which we attribute to the suppression of keto defect formation by performing the characterisation in vacuum. At low temperatures this spectral contribution is further decreased due to the reduced migration of excitations to CT states and keto defects.

Comparing the spectra of the two phases of the 5% Pt copolymer, we observe a decreased intensity of the triplet emission relative to the singlet emission for the β phase compared to the glassy phase copolymer films. We expect the spin-orbit coupling in both phases to be the same since it is determined by the heavy atom. Also, the $S_1 - T_1$ gap in both conformation is constant (0.7 eV). Therefore, we conclude that the difference in phosphorescence intensity is not caused by a difference in intersystem crossing rate in the two phases. Nevertheless, heavy atom spin-orbit coupling is not a long range effect. Migration is important as it determines the ability of an exciton to find a site where spin-orbit coupling takes place. This is different for the glassy and β phases. Improved migration of glassy excitations allows them to get close enough to Pt-complexes and results in better overall intersystem crossing. In the β phase the lower energy exciton tends to stay on the β phase segment as transfer to higher energy glassy phase segments is energetically unfavourable. Therefore, it is less likely to encounter a Pt-complex resulting in overall lower intersystem crossing. This would explain the difference

in the PL spectra of the two conformations. High intersystem crossing leads to strongly quenched fluorescence and intense phosphorescence as seen for the glassy phase while for the β phase the reduced migration of the exciton leads to less intersystem crossing and the observed strong well resolved fluorescence but weak phosphorescence. Additionally, the nonradiative decay rate is very sensitive to the triplet energy, increasing exponentially as triplet energy decreases according to the energy gap law [27, 168]. Hence, we would expect the lower lying β phase triplet state to experience more nonradiative decay leading to a lower emission intensity.

In the phosphorescence spectra of the β phase Pt copolymer samples, alongside the main 0-0 emission peak of the β phase triplet, there is a high energy shoulder located at the position of the glassy phase triplet state (figure 6.7). However, there is no evidence for the presence of glassy phase in the singlet emission. It has been previously shown that β phase emission dominates the fluorescence spectrum of PFO even in films containing small fractions of β phase chains due to efficient transfer with a large Förster radius [49]. We rationalize the observed phosphorescence spectrum in terms of the short range Dexter transfer for triplets. After photoexcitation, triplets are generated from singlets via intersystem crossing. It has been shown that energy transfer between the two phases of PFO occurs on a picosecond time scale [49] while intersystem crossing in aromatic hydrocarbons is expected to be slower taking place on a nanosecond time scale [169]. Thus, we would expect that by the time intersystem crossing takes place most singlets would be located on β phase chain segments, nevertheless, a small fraction of singlet excitons could still be located on the glassy phase. If some intersystem crossing takes place on glassy phase chromophores neighbouring Pt-complexes, those triplets may not be efficiently converted to β phase triplets due to the limited energy transfer of triplets. In the absence of thermal activation we suspect the glassy phase triplets remain in close proximity to their parent chromophore due to inefficient energy transfer migration. The energy transfer of triplet excitons will be discussed in detail in section 6.5. The comparable emission intensity of the glassy triplet to the β phase triplet could

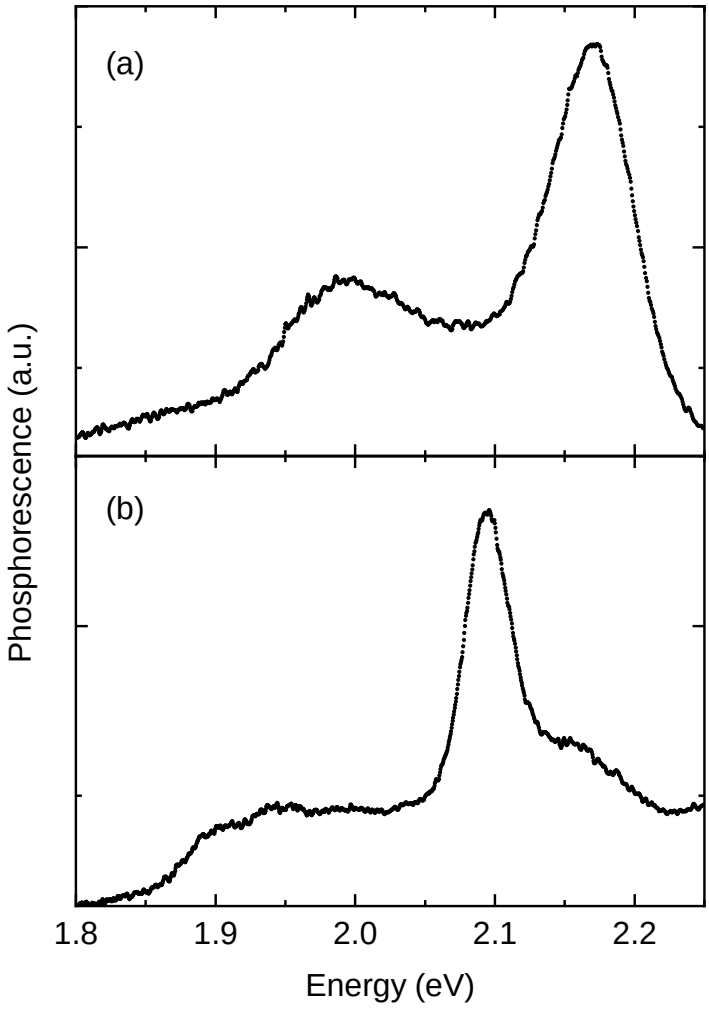


Figure 6.7: The phosphorescence spectrum of (a) glassy phase and (b) β phase 5% Pt copolymer at 5 K depicted on an extended energy scale.

result from the lower nonradiative recombination of the higher lying glassy triplet state. Finally we note, that similar to the fluorescence, at the energetic position where the 0-1 transition of the β phase phosphorescence is expected, ~ 1.95 eV, there are three weak emission bands just about visible. Thus, at low temperature reduced inhomogeneous broadening reveals three different vibrational modes.

The increase in non-radiative decay with temperature for triplets is associated

with thermally activated diffusion leading to enhanced triplet-triplet annihilation and increased sampling of non-radiative sites and dissociation sites. The strong temperature dependence of the triplet is believed to be due to its long lifetime, as a result it is much more sensitive to thermally activated non-radiative decay mechanisms.

In conclusion, we demonstrate that the incorporation of a platinum containing metal-ligand complex into the backbone of PFO leads to the radiative decay of PFO triplet excitons at low temperatures. This is a result of increased spin-orbit coupling from the heavy metal atom. Both glassy phase and β phase triplet emission was successfully detected by using relevant sample fabrication conditions for the formation of the two chain conformations. The assignment of the triplet emission is based on the fact that it has similar vibrational spacing as the fluorescence, it is separated by 0.7 eV from the PFO fluorescence and it resembles the phosphorescence spectra of closely related compounds [31, 165, 166] and the triplet-triplet photoinduced absorption spectrum of PFO [85].

6.5 Triplet Energy Transfer

In disordered organic semiconductors, the transport of excitations proceeds by hopping from one localized site to the next within an inhomogeneously broadened density of states (DOS). The electronic coupling can be provided by either long range coulomb interactions termed Förster transfer [28] typical for singlet excitations or short range exchange interactions called Dexter transfer [29] for triplet excitons.

Hopping theory predicts that an exciton generated within a Gaussian density of states distribution will relax towards the tail of the distribution by hopping along neighbouring sites. Initially, the exciton path will be dominated by energetically downhill hops until a quasi-equilibrium is obtained when there is a balance between downhill jumps and thermally activated uphill jumps. This

occurs since the exciton may take an energy consuming upward jump in order to avoid a long-distance exothermic hop. The quasi-equilibrium energy is given by the long time limit of the statistically weighted average using the Gaussian $g(\varepsilon) = \left(1/\sqrt{2\pi\sigma}\right) \exp\left(-\left(\varepsilon - \varepsilon_0\right)^2 / 2\sigma^2\right)$ where ε is the energy of an individual molecule, ε_0 is the energy of the centre of the distribution and the standard deviation σ, also known as the disorder parameter, describes the width of the distribution. This result yields quasi-equilibrium at an energy $-\sigma^2/kT$ below the center of the DOS and is independent of the mode of coupling [170]. Therefore, upon lowering the temperature, the emission is expected to redshift and eventually become constant when the time needed to reach the quasi-equilibrium energy exceeds the exciton lifetime [162, 171–173].

At low temperatures three phenomena become important. Firstly, as the temperature decreases the time taken to reach quasi-equilibrium increases. This is due to the fact that as the relaxation proceeds there are less available target sites since the excitation moves towards the tail of the DOS. Therefore, below a certain temperature, the spectral diffusion will be terminated by the exciton lifetime and will decay at an energy above quasi-equilibrium leading to a saturation of the spectral shift. Secondly, kinetic frustration of the diffusion could lead to a hypsochromic shift at low temperatures. This has been observed for excitations that couple by short range interactions such as triplets. It happens because during the relaxation process an exciton executes a diffusive random walk towards the quasi-equilibrium energy and sometimes in the course of these incoherent transfer events it has to overcome an intermediate energy barrier via thermal activation. However, as the temperature is lowered this becomes increasingly difficult and activated jumps away from some intermediate sites are no longer possible. The exciton decays at an energy above the quasi-equilibrium energy. Finally, contrary to this singlet excitations couple by long range Förster transfer which allows them to reach lower energy sites further away [7]. Spectral diffusion is depicted schematically

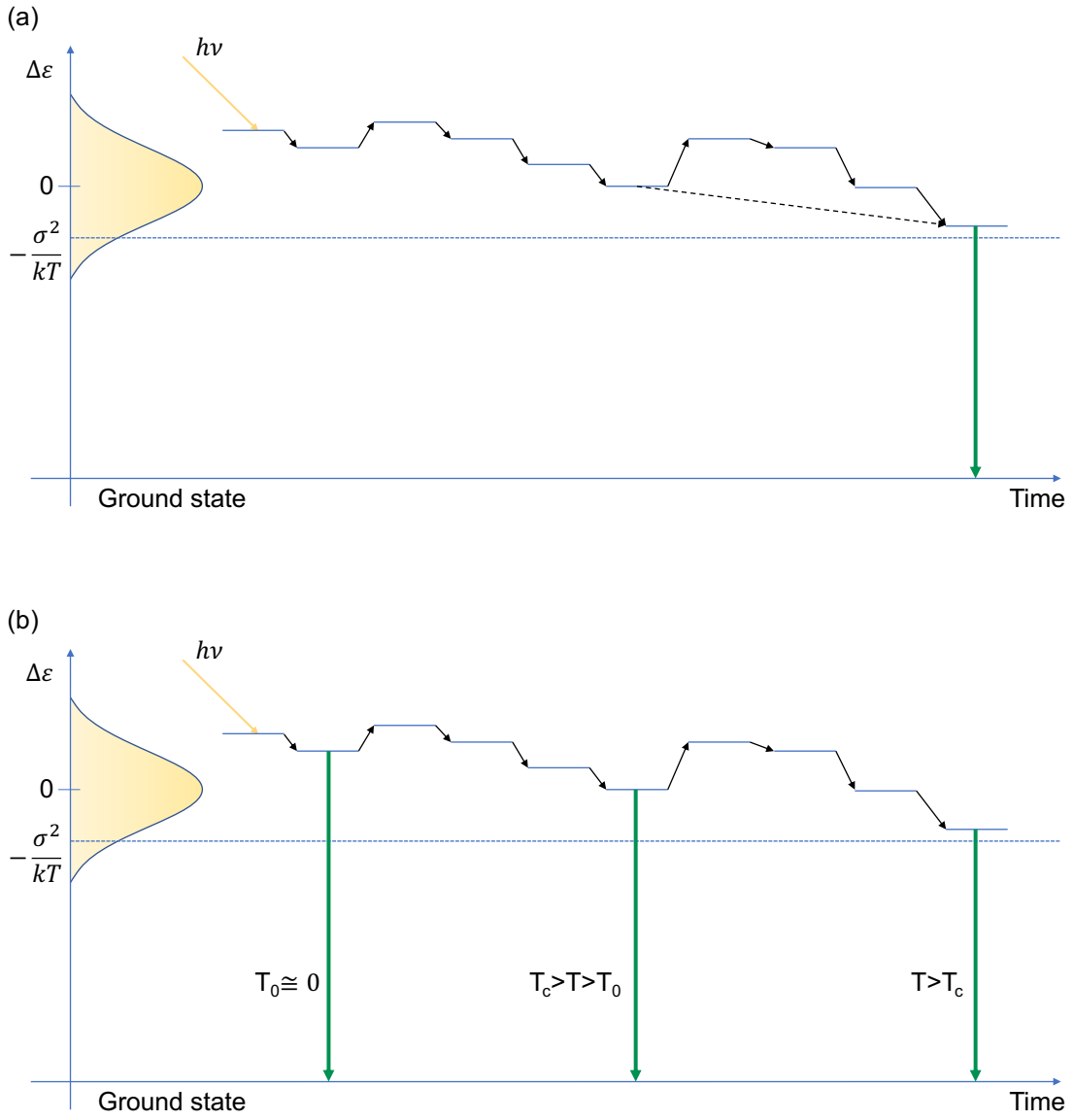


Figure 6.8: Schematic illustration of spectral diffusion. Gaussian DOS drawn with $\varepsilon_0 = 0$. (a) Photoexcited singlet excitons hop from site to site (solid black arrows), sometimes requiring thermal activation energy. At sufficiently high temperatures, the quasi-equilibrium energy is reached from where emission takes place. At low temperatures, activated jumps away from some intermediate sites are no longer possible, however, the long range Förster transfer makes jumps to lower energy sites further away feasible (dotted black arrow) so that the quasi-equilibrium energy can still usually be reached. (b) Triplet excitons, created by intersystem crossing following photoexcitation, hop from site to site (solid black arrows), sometimes requiring thermal activation energy. At sufficiently high temperatures, $T > T_c$, the quasi-equilibrium energy is reached from where emission takes place. At insufficient temperatures, $T < T_c$, activated jumps away from some intermediate sites are no longer possible and the excitation decays before it has reached quasi-equilibrium. After reference [7].

in figure 6.8.

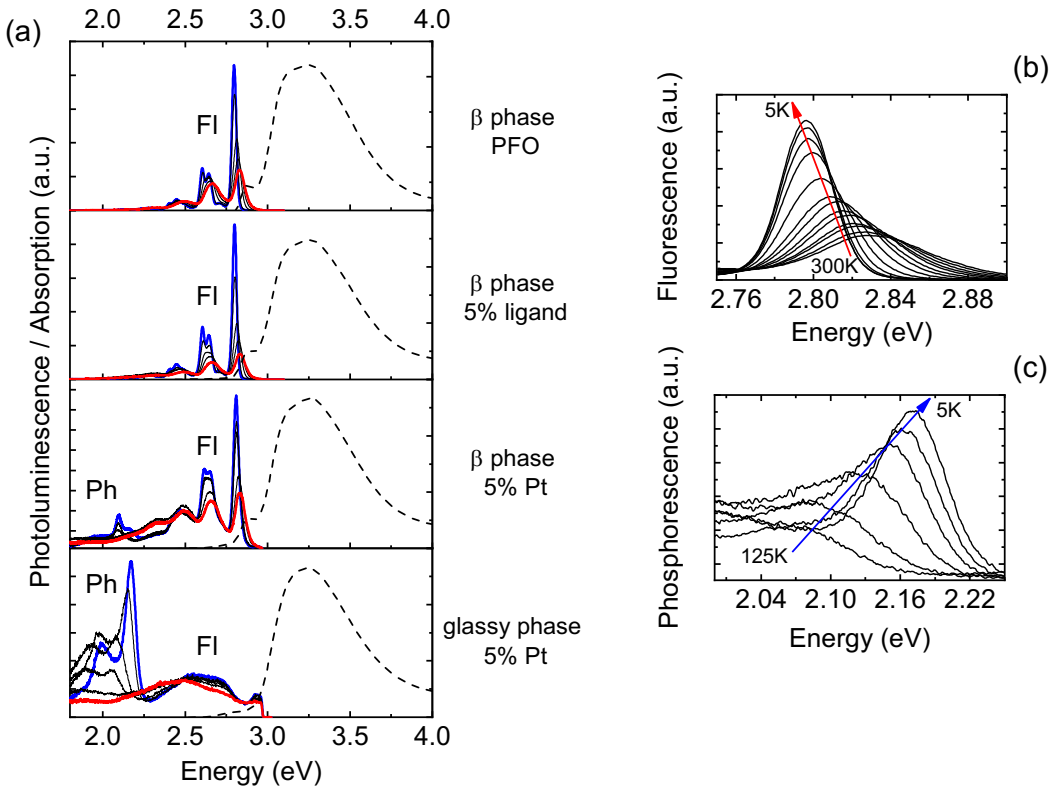


Figure 6.9: (a) Fluorescence (Fl) and phosphorescence (Ph) spectra (solid lines) at selected temperatures for β phase PFO, 5% ligand, 5% Pt copolymers and glassy phase 5% Pt copolymer (top to bottom) alongside the absorption spectra at 300 K (dashed line). The emission spectra are shown from 10 K (blue upper thick line) to 300 K (red lower thick line). (b) Fluorescence spectra of β phase PFO between 5 K and 300 K. (c) Phosphorescence spectra of glassy phase 5% Pt copolymer between 5 K and 125 K.

Figure 6.9 shows the photoluminescence spectra of β phase PFO, 5% Pt, 5% ligand copolymers and glassy phase 5% Pt copolymer in the temperature range between 5 and 300 K. Their room temperature absorption spectra are presented alongside. For clarity, the photoluminescence spectra are only shown for a few selected temperatures. The full set of temperature dependent PL spectra are presented in appendix B section B.3. In figure 6.9 (b) and (c) representative fluorescence spectra of β phase PFO and phosphorescence spectra of the glassy phase 5% Pt copolymer are depicted on an extended energy scale. The fluorescence spectra of the copolymers and PFO experience a bathochromic shift with decreasing

temperature until the spectral diffusion saturates at a characteristic temperature T_c irrespective of chain conformation. In contrast, the phosphorescence spectra of the 5% Pt copolymer show two very different behaviours depending on the phase. The glassy phase triplet emission exhibits a hypsochromic shift while the β phase phosphorescence remains stationary. Unfortunately, the phosphorescence spectra could only be measured at low temperatures as a result of triplet quenching and their behaviour above T_c could not be studied.

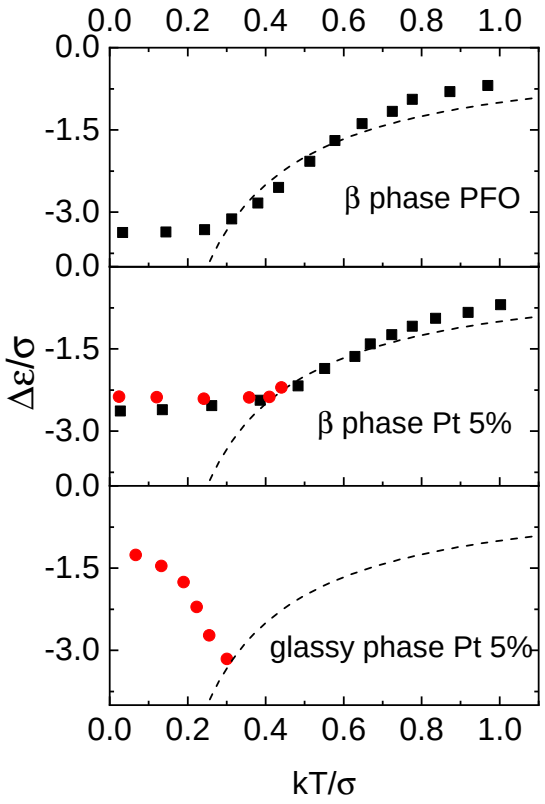


Figure 6.10: Energy difference $\Delta\varepsilon$ between the center of the DOS and the center of the $S_1 \rightarrow S_0$ 0-0 fluorescence band (black squares) or the center of $T_1 \rightarrow S_0$ 0-0 phosphorescence band (red circles) normalized to σ versus kT/σ. The dashed curve is the theoretically predicted $\Delta\varepsilon/\sigma(T) = -\sigma(T)/kT$ dependence.

We now discuss the spectral diffusion observed in figure 6.9 in terms of the theory of a random walk within a Gaussian DOS. We begin our analysis with the spectral diffusion of singlet excitons. To do this we determine the center of the DOS

from the peak of the room temperature $S_1 \leftarrow S_0$ 0-0 absorption and we deduce its width, $\sigma(T)$, from the linewidth of the 0-0 vibrational transition of the fluorescence at different temperatures. The linewidth was estimated by performing a Gaussian fitting to the emission. The spectral shift, $\Delta\varepsilon(T)$, is then calculated from the energy difference between the center of the DOS and the centre of the $S_1 \rightarrow S_0$ 0-0 fluorescence emission. In figure 6.10 the energy difference, $\Delta\varepsilon(T)$, normalized to $\sigma(T)$ is plotted against $kT/\sigma(T)$. The dashed curve is the theoretically predicted $\Delta\varepsilon(T)/\sigma(T) = -\sigma(T)/kT$ relation.

From figure 6.10 we observe that the fluorescence is in good agreement with the predicted dependence for $kT/\sigma > 0.3 - 0.4$. At lower temperatures $\Delta\varepsilon(T)/\sigma(T)$ saturates. This is a sign of the termination of spectral diffusion due to the limited exciton lifetime and occurs when the longer transfer time needed to reach quasi-equilibrium exceeds the exciton lifetime. The PFO spectrum saturates at a lower value of $\Delta\varepsilon(T)/\sigma(T)$ than the Pt copolymer. This is suggested to be due to the potentially shorter lifetime of the singlet of the Pt copolymer due to efficient intersystem crossing to the triplet manifold resulting from strong spin-orbit coupling of the heavy metal atom. We expect the singlet lifetime in the copolymers to decrease with increasing platinum content and suspect this is the cause of the observed difference in figure 6.6 (a) in the red shift of the low temperature fluorescence for the different Pt copolymers. The observed spectral diffusion of the singlet excitons is in agreement with previous studies on related compounds [162, 171, 174].

The same analysis is performed on the phosphorescence spectra of the two phases of the 5% Pt copolymer and is shown as red circles in figure 6.10. In this case the center of the DOS of the triplet states was selected by considering the mirror symmetry between absorption and emission and the disorder parameter, σ, was deduced from the linewidth of the $T_1 \rightarrow S_0$ 0-0 emission. Due to triplet quenching we were unable to collect data above 125 K and, therefore, were able to study the triplet exciton behaviour only in the low temperature regime. The two phases of

the copolymer show very different behaviour. While the β phase behaves similar to the singlet excitations, for the glassy phase a hypsochromic shift upon cooling is observed. This is related to kinetic freezing out of the energetic relaxation. This result is very interesting since it allows us to explore the role of microstructure in triplet exciton transfer using the same material. But before we discuss the features of the two phases that result in the difference in transport, let us first consider the transfer mechanisms for singlet and triplet excitations.

The motion of triplet states proceeds by short range exchange interactions which have an exponential dependence on the coupling distance (e^{-R}). Exchange interactions require orbital overlap, thus, restricting the number of target sites for transfer. Frustration can then occur when all nearest neighbours have a higher energy which cannot be overcome with the available thermal energy and the triplet becomes trapped in a local energy minimum from which emission occurs. This happens at increasingly higher energies with lowering temperature resulting in the hypsochromic shift observed. Singlets, on the other hand, diffuse by Förster transfer which has an algebraic dependence on the coupling distance (R^{-6}) and so enables transfer between sites that are located further apart. Therefore, for singlets there is a large number of available target sites for transfer allowing diffusion over large distances to take place without the need for thermal activation since the probability that there will be a site at an accessible energy increases when hops further away are possible.

The hypsochromic shift seen for triplets in the glassy phase is in good agreement with theory and experiments for exciton transfer via short range exchange interactions [162, 172, 173]. Yet, the spectra of the β phase samples have a low temperature behaviour similar to the trends for singlets. The glassy and the β phases differ in their variance, σ, of the DOS which is reflected in the difference of the emission linewidth and is caused by the increased disorder in the glassy phase compared to the β phase. The lack of frustration in the more ordered β phase cannot be due to the

smaller disorder parameter since this is taken care of by normalizing the data to units of σ. Instead, we suggest that the difference stems from an aspect related to the weak disorder, namely, the increased conjugation length in the β phase allows the triplet to migrate along the chain raising the number of available neighbours. Monte Carlo simulations have been previously employed to demonstrate that the appearance of frustration is caused by a restricted number of target sites [171]. In the case of the β phase samples the longer conjugation length increases the accessible target space and frustration is lifted. Thus, we have shown that triplet diffusion in PFO can be greatly affected by the film microstructure and while frustration is observed for the glassy phase, it can be suspended by changing the sample conformation to the more extended β phase where triplet excitons can sample a larger number of acceptor sites.

6.6 Excitation Power Dependence

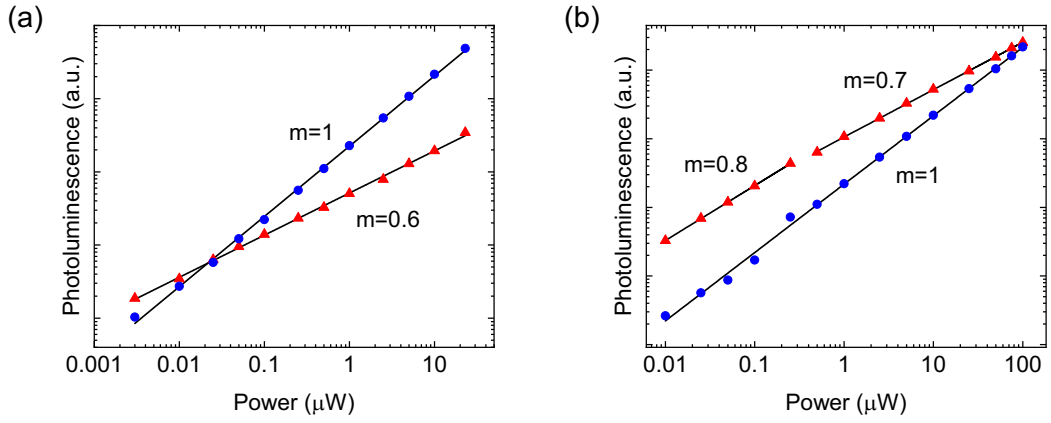


Figure 6.11: Dependence of fluorescence (blue circles) and phosphorescence (red triangles) on excitation power at 5 K for the (a) β and (b) glassy phases of the 5% Pt copolymer. The solid lines correspond to linear fits with slope m on a double logarithmic scale.

In order to further study the differences between the two conformations of the copolymers in the excited state decay, we measured the dependence of fluorescence and phosphorescence on the incident laser power at 5 K, the collected data plotted

in double logarithmic presentation is shown in figure 6.11. The excitation power range explored for the β phase conformation is slightly lower due to saturation of the detector at higher excitation intensities resulting from the stronger emission observed from the β phase compared to the glassy phase.

We observe a linear dependence on excitation power for the fluorescence of both conformations of the Pt copolymer. A linear dependence on excitation power indicates monomolecular recombination dynamics [9]. In contrast, the phosphorescence dependence on incident laser power is sublinear with a slope of 0.6 for the β phase and 0.8 at lower powers and 0.7 at higher powers for the glassy phase. This sublinearity is an evidence for the occurrence of a nonlinear quenching process for triplet excitons such as triplet-triplet annihilation (TTA). We speculate that the lower slope seen for the β phase reflects more efficient triplet-triplet annihilation compared to the glassy phase. This is consistent with our findings that the triplet state in the β phase conformation can migrate more effectively in the copolymer. TTA can result in the formation of singlet excitons leading to the observation of delayed fluorescence. We were unable to measure decisively any delayed fluorescence since the setup did not have the capacity for time gated detection. It is not possible to distinguish prompt and delayed fluorescence from continuous measurements due to their spectral overlap. The linear dependence on excitation power of the measured singlet emission suggests that any delayed fluorescence contribution must be very weak since a superlinear dependence would be expected for delayed fluorescence emission.

The observed bimolecular recombination is further evidence for triplet migration at low temperatures. Triplet diffusion can enhance TTA which is otherwise limited by the rate of long range interactions.

6.7 Conclusion

In summary, we have investigated the photophysical properties of a series of platinum containing polyfluorene copolymers. It was demonstrated that the incorporation of a heavy platinum atom into the PFO backbone allows triplet state emission to be studied directly due to increased spin-orbit coupling making the $T_1 \rightarrow S_0$ transition partially allowed. Meanwhile, the copolymer luminescence was shown to originate mainly from the PFO unit via comparison of homopolymer and copolymer spectra. Additionally, following the fabrication protocols used for PFO, both the glassy and β phase conformations were successfully induced in films of the copolymers as reflected by absorption and photoluminescence. This enabled the study of triplet transport as a function of energetic disorder and conjugation length without the need for additional chemical modification.

From the temperature dependent shift of the fluorescence and phosphorescence spectra of the copolymer with the highest platinum content (5% Pt), the spectral diffusion of singlet and triplet excitons was analysed. The temperature dependence was evaluated in the context of random walk theory with a focus on the material characteristics leading to kinetic frustration for triplet excitons. A hypsochromic shift was observed for the phosphorescence of the glassy phase of the copolymer as a result of frustrated relaxation. This is due to the thermally activated jumps necessary to advance spectral diffusion becoming progressively frozen out with decreasing temperature. The frustration effect is characteristic for excitations that migrate via short range transfer such as triplets which couple by orbital overlap interactions. Frustration is lifted in the β phase of the copolymer as a result of increased conjugation of the planarised conformation making more hopping sites available. Consequently, the triplet can explore a larger number of acceptor sites, therefore, increasing the probability for nonactivated triplet exciton transfer. Comparing copolymer films that differ only in their microstructure allows to eliminate the influence of chemical composition.

This investigation demonstrates that triplets can diffuse more effectively along highly conjugated polymer chains than along materials with short conjugation segments. This has important implications for material design. Polymers with long conjugation lengths are, therefore, well suited for triplet transporting materials for energy transfer purposes such as solar cells and triplet upconversion applications. Meanwhile highly disordered materials are appropriate for use where triplet diffusion is detrimental and should be suppressed such as phosphorescent OLEDs where the diffusion of triplets to quenching sites can reduce the device efficiency.

7
Conclusions and Future Work

Understanding the structure-property relationship of organic semiconducting polymers is critical for their future development for technological applications. To this end, studying suitable model systems is needed to expand our knowledge of how to modify the chemical structure of materials to get the desirable performance necessary for commercialization.

One approach to tailor the optoelectronic properties of conjugated polymers consists in the copolymerisation of different amounts of functional moieties into the polymer backbone. In this thesis we have explored the effect of polyfluorene copolymerisation for improved material design. The materials investigated are based on the well known polyfluorene poly(9,9-dioctylfluorene) (PFO). PFO constitutes a fascinating system in itself due to its ability to adopt several different chain conformations, therefore, enabling the study of film microstructure on fundamental photophysical properties. In this body of work we have investigated the copolymerisation of PFO with three different functional moieties. Their effect on the optical and electrical characteristics of PFO was examined in order to establish the structure-property relationships that govern the observed modifications. We hope that this will provide valuable insight for future targeted material design.

The first modification studied was the copolymerisation of different amounts (5, 10, 20 and 50%) of a hole transporting arylamine moiety into a PFO backbone. PL spectroscopy measurements of solvent vapour annealed copolymer films containing 5, 10 and 20% arylamine exhibited β phase formation in the F8 chain segments. It was also demonstrated that heating the solvent vapour annealed copolymer films progressively lowers the β phase content until the films become completely glassy above 115 °C for 90F8:10BSP and 130 °C for 95F8:5BSP. The difference in threshold transition temperatures for the copolymers and its relationship to arylamine content deserve further attention and should be the focus of future work. The dependence of the glass transition temperature of the copolymers on arylamine content can also give further insight into the polymer dynamics and differential scanning calorimetry measurements would be required to investigate this.

We showed that the hole charge carrier mobility of the fluorene homopolymer PFO ($4\times10^{-4}\,\mathrm{cm^2V^{-1}s^{-1}}$ [4, 42, 99]) is drastically reduced by the copolymerisation of 5% of arylamine to $8\times10^{-8}\,\mathrm{cm^2V^{-1}s^{-1}}$ as a result of trapping at the arylamine sites. With increasing arylamine percentage the mobility rises due to the commencement of direct trap-to-trap transport that replaces the release of carriers back to the lower ionization potential fluorene transport sites as the dominant transport mechanism. The alternating copolymer PFB (50% arylamine) has a mobility ($3.8\times10^{-4}\,\mathrm{cm^2V^{-1}s^{-1}}$) similar to that of PFO. Thus, at high trap concentrations transport through the trap state manifold becomes possible. Air photoemission spectroscopy (APS) measurements confirmed the presence of two discrete energy states with different ionization potentials for the 5, 10 and 20% arylamine copolymers with the lower ionisation potential state acting as a hole trap. This demonstrates that the hole mobility of an organic semiconductor may be controlled over a large range by the copolymerisation of different amounts of a lower ionisation potential transporting moiety.

An interesting future direction for the work described would be an investigation of the energy levels and DOS distributions of the two moieties within the copolymers. APS data for the copolymers showed that there are two energy level contributions that evolve with arylamine content. The two energy level contributions shift to lower energies with increasing arylamine content. Additionally, the energy difference between the two contributions decreases as the arylamine content in the copolymers increases resulting in an effectively lower trap depth, vanishing for PFB. This bears resemblance to reports suggesting that in a trap-containing medium the effective disorder parameter decreases at large trap concentrations [79, 103]. This has been interpreted as evidence of percolative type motion of charge carriers within the trap manifold as the distance between traps becomes sufficiently close for transport [103]. How the measured effective trap depth in our study is related to the activation energy for transport and the disorder parameter value in a material is an interesting direction for future investigation. Exploring the potential of the APS technique for studying charge trapping deserves further attention. This measurement method does not require vacuum conditions or low temperatures, therefore, significantly reducing experimental efforts compared to thermally stimulated luminescence (TSL) and charge carrier mobility studies. Comparing APS data to TSL and charge mobility experiments would shed further light on its applicability for studying charge trapping.

Insight can be gained through supplementary measurements and device modelling. Determining the energy levels by cyclic voltammetry (CV) and ultraviolet photoemission spectroscopy (UPS) would give additional comparison data. Information about the DOS distribution can be obtained by calibrating the APS measurements using metals of similar ionization potentials as the copolymers whose density of states are known. Also, numerical device modelling using drift diffusion simulations can be employed to extract hole trap parameters from experimentally measured current voltage characteristics. Finally, we suggest the dependence of the hole mobility on temperature deserves investigation. The results of such a study can

then be analysed using the correlated disorder model [41] and values for the energetic and spatial disorder values as well as intersite hopping distance can be deduced. This would allow to examine how the arylamine content impacts these parameters.

The second modification investigated involved the copolymerisation of polyfluorene with phenoxazine resulting in the alternating copolymer F8BPPOZ. The incorporation of the phenoxazine polymer into a PFO backbone increases the rigidity of the copolymer compared to the chemically similar hole transporting copolymer TFB by reducing the number of torsions in the polymer chain. This is supported by DSC measurements showing a high glass transition temperature for F8BPPOZ of $196 \pm 4\,^{\circ}\mathrm{C}$ which indicates a rigid backbone. This value is higher than both TFB ($140\,^{\circ}\mathrm{C}$ [123]) and the fluorene homopolymer PFO ($50\,^{\circ}\mathrm{C}$ [122]). The phenoxazine copolymerisation was demonstrated to lower the ionization potential, I_p, of polyfluorene ($I_p = 5.88 \pm 0.05\,\mathrm{eV}$) to $5.1 \pm 0.05\,\mathrm{eV}$ for F8BPPOZ due to the electron donating properties of the phenoxazine ring leading to enhanced hole accepting characteristics. Resilience to thermal fluctuations of the torsions along the polymer backbone within and between structural domains has been proposed to determine the energy landscape and lead to low energetic disorder and high mobilities in materials [109, 110]. Nevertheless, the hole mobility of F8BPPOZ as deduced from DIT measurements is $7 \times 10^{-4}\,\mathrm{cm^2V^{-1}s^{-1}}$ at an electric field of $5 \times 10^5\,\mathrm{V\,cm^{-1}}$ which is only slightly higher than PFO ($4 \times 10^{-4}\,\mathrm{cm^2V^{-1}s^{-1}}$ [4, 42, 99]) and at least an order of magnitude lower than values reported for TFB ($(5 - 10) \times 10^{-3}\,\mathrm{cm^2V^{-1}s^{-1}}$ [79, 80]). Therefore, we conclude that in the case of F8BPPOZ, the incorporation of the more rigid POZ molecule does not improve hole transport compared to TFB and other factors must be dominating. Quantum chemical calculations have shown that in a model fluorene-phenoxazine copolymer the HOMO orbital is localized on the phenoxazine unit while the LUMO orbital is situated on the fluorene moiety [117], therefore, reducing the hole wavefunction overlap along the polymer chain. This would lower the probability of hole charge carrier hopping required for transport. Additionally, the polar nature of F8BPPOZ

can lead to increased energetic disorder of the transport sites and lower mobility. In contrast, for the non-polar TFB a narrow transport manifold has been inferred from temperature dependent hole mobility measurements [80]. Further studies including an investigation of the temperature dependence of hole transport would be necessary to shed light on the critical material characteristics that influence the hole mobility of F8BPPOZ.

Subsequently, F8BPPOZ was tested as a hole transporting interlayer in thin film 95PFO:5F8BT blend polymer light emitting diodes. The performance of devices with a F8BPPOZ interlayer was inferior to reference devices with a TFB interlayer and even with no interlayer. This was attributed to a combination of unfavourable hole injection barriers, electron blocking characteristics and exciton blocking properties. We stress that device improvements are strongly dependent on finding a compatible combination of interlayer material and light-emitting material. Therefore, we suggest that F8BPPOZ may be a good interlayer material in combination with different emissive layers. Poly(*p*-phenylene vinylenes) (PPV) materials such as Super Yellow may be good candidates due to their favourable energy levels relative to F8BPPOZ.

Finally, the emission characteristics of semiconductor heterojunctions formed for 1:1 blends of F8BPPOZ:F8BT and TFB:F8BT were compared. PL and PLQE measurements of a F8BPPOZ:F8BT blend demonstrated strong photoluminescence quenching in the blend compared to TFB:F8BT blends and pure F8BT. The F8BPPOZ:F8BT blend emission centered $\sim 620\,\text{nm}$ was assigned to an interfacial exciplex state due to its broad red shifted spectrum compared to both blend materials. Studies in the literature [145, 146] have proposed that in all type II heterojunction blends, the exciton first dissociates at the interface and forms a geminate charge pair yet geminate pair recombination via an intermediate exciplex can regenerate the bulk excitons. In TFB:F8BT blends effective F8BT exciton regeneration leads to high PLQE (39%). The quenching in F8BPPOZ:F8BT blends (PLQE 4%) was proposed to result from efficient geminate pair dissociation at the

interface between the two polymers. The geminate pair separation and the back transfer activation energy of the blend have been identified as critical parameters determining the photoluminescence quenching [145, 146]. To measure those electric field dependent PL spectroscopy and its dependence on temperature are necessary and should be included in future work. Additionally, the effect of blend morphology and phase separation on the emission properties of F8BPPOZ:F8BT blends would be an interesting avenue for future investigation. Also, despite charge separation at the heterojunction between F8BPPOZ and F8BT in the PLED devices studied being energetically unfavourable due to the anode being situated on the F8BPPOZ side, the heterojunction can still quench the F8BT emission by blocking energy transfer from PFO to F8BT in the light emitting blend if F8BT excitons at the interface between the emissive layer and the F8BPPOZ interlayer form stable geminate electron-hole pairs. Therefore, we suggest that the formation of stable interfacial electron-hole pairs at the heterojunction between F8BT and F8BPPOZ can be among the factors leading to the poor device performance of PLEDs employing a F8BPPOZ IL. A thermal experiment may be of interest in order to investigate this hypothesis further. This could consist of electrically generating the geminate electron-hole pairs in the PLED structure at low temperature, switching off the voltage and then warming up to see if emission occurs as the pairs thermally dissociate. This may give rise to a distinct emission spectrum.

The final modification studied was the copolymerisation of PFO with various amounts (0.5, 1, 2.5 and 5%) of a cyclometalated platinum complex (PyTPAPt(acac)). It was demonstrated that the incorporation of a heavy platinum atom into the PFO backbone allows triplet state emission to be studied directly due to increased spin-orbit coupling making the $T_1 \rightarrow S_0$ transition partially allowed. Additionally, following the fabrication protocols used for PFO, both the glassy and β phase conformations were successfully induced in films of the copolymers which enabled the study of triplet transport as a function of energetic disorder and conjugation length.

From the temperature dependent shift ($300 - 5\,\mathrm{K}$) of the fluorescence and phosphorescence spectra of the copolymer with the highest platinum content (5% Pt), the spectral diffusion of singlet and triplet excitons was analysed. The temperature dependence was evaluated in the context of random walk theory with a focus on the material characteristics leading to kinetic frustration for triplet excitons. A hypsochromic shift was observed for the phosphorescence of the glassy phase of the copolymer as a result of frustrated relaxation. This is due to the thermally activated jumps necessary to advance spectral diffusion becoming progressively frozen out with decreasing temperature. The frustration effect is characteristic for excitations that migrate via short range transfer such as triplets which couple by orbital overlap interactions. Frustration is lifted in the β phase of the copolymer as a result of increased conjugation of the planarised conformation making more hopping sites available. Consequently, the triplet can explore a larger number of acceptor sites, therefore, increasing the probability for nonactivated triplet exciton transfer.

This investigation demonstrates that triplets can diffuse more effectively along highly conjugated polymer chains than along materials with short conjugation segments. This has important implications for material design. Polymers with long conjugation lengths are, therefore, well suited for triplet transporting materials for energy transfer purposes such as solar cells and triplet upconversion applications. Meanwhile highly disordered materials are appropriate for use where triplet diffusion is detrimental and should be suppressed such as phosphorescent OLEDs where the diffusion of triplets to quenching sites can reduce the device efficiency. We propose that future steps in this investigation will involve testing the above conclusions in a real application and exploring how the polyfluorene chain conformation affects the device performance.

Appendices

A

Arylamine Copolymerisation

A.1 Spectral Deconvolution for Determination of β Phase PL Contribution

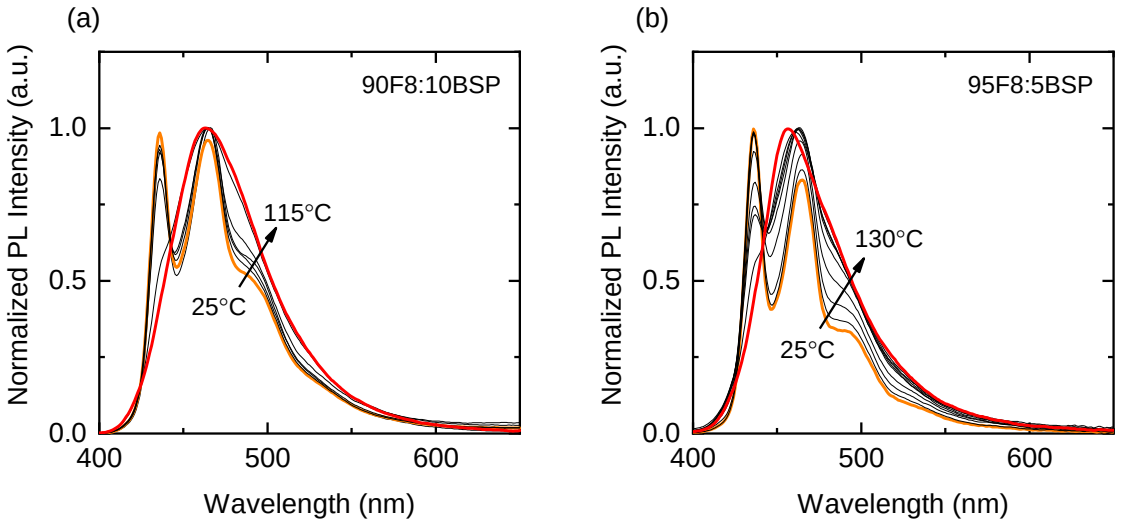


Figure A.1: The peak normalized PL spectra for solvent vapour annealed films of (a) 90F8:10BSP following thermal annealing from 25 °C (orange thick line) to 115 °C (red thick line) and (b) 95F8:5BSP following thermal annealing from 25 °C (orange thick line) to 130 °C (red thick line).

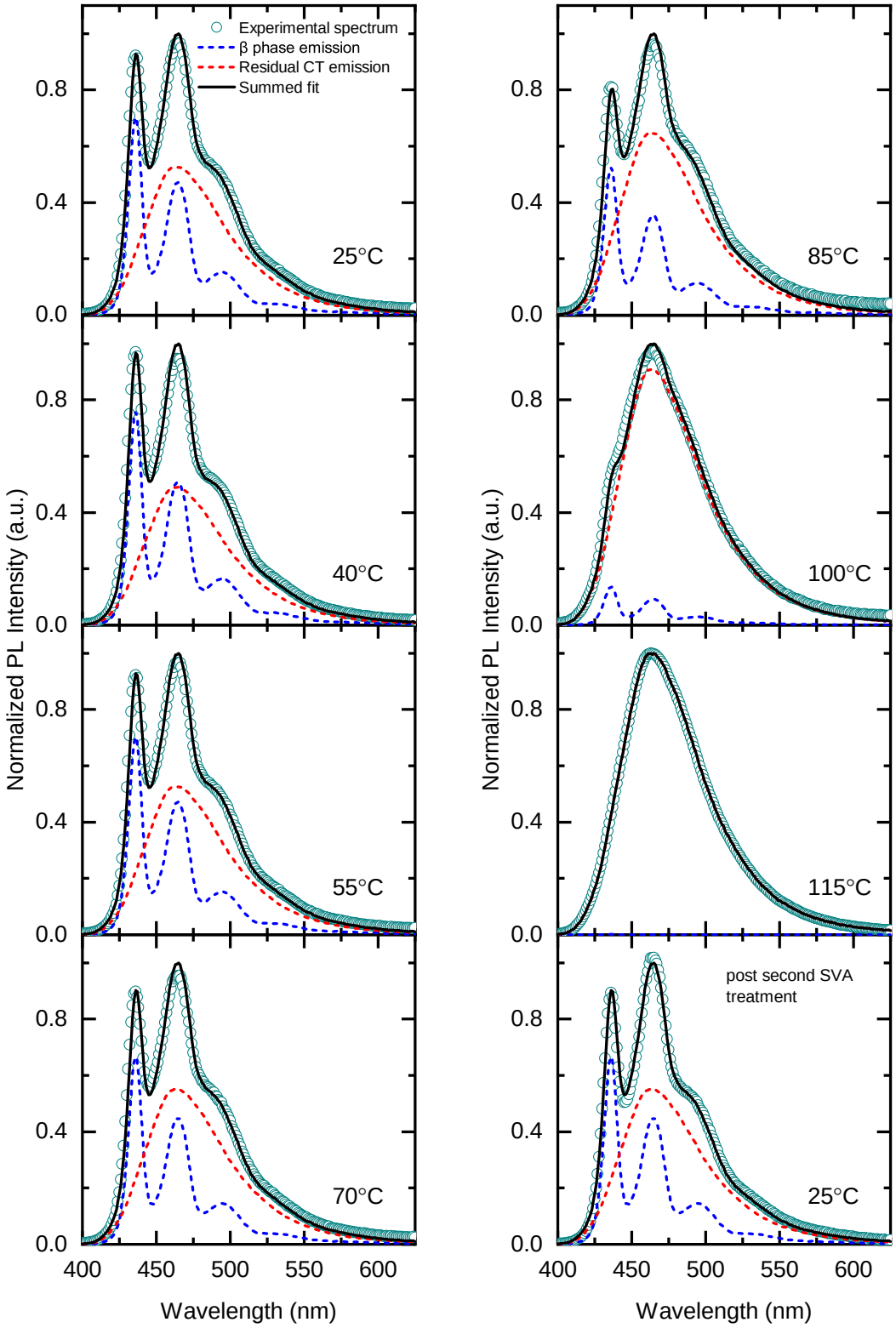


Figure A.2: PL spectra deconvolutions for 90F8:10BSP solvent vapour annealed (SVA) film before and after thermal annealing for 10 minutes at $40, 55, 70, 85, 100$ and $115\,^{\circ}\mathrm{C}$. The spectrum following a second solvent vapour annealing treatment is also presented. The dashed red line gives the residual PFB-like CT emission while the dashed blue line shows the vibronic β phase contribution. The black solid line is the combined sum of both while the open green circles show the experimentally measured PL spectra.

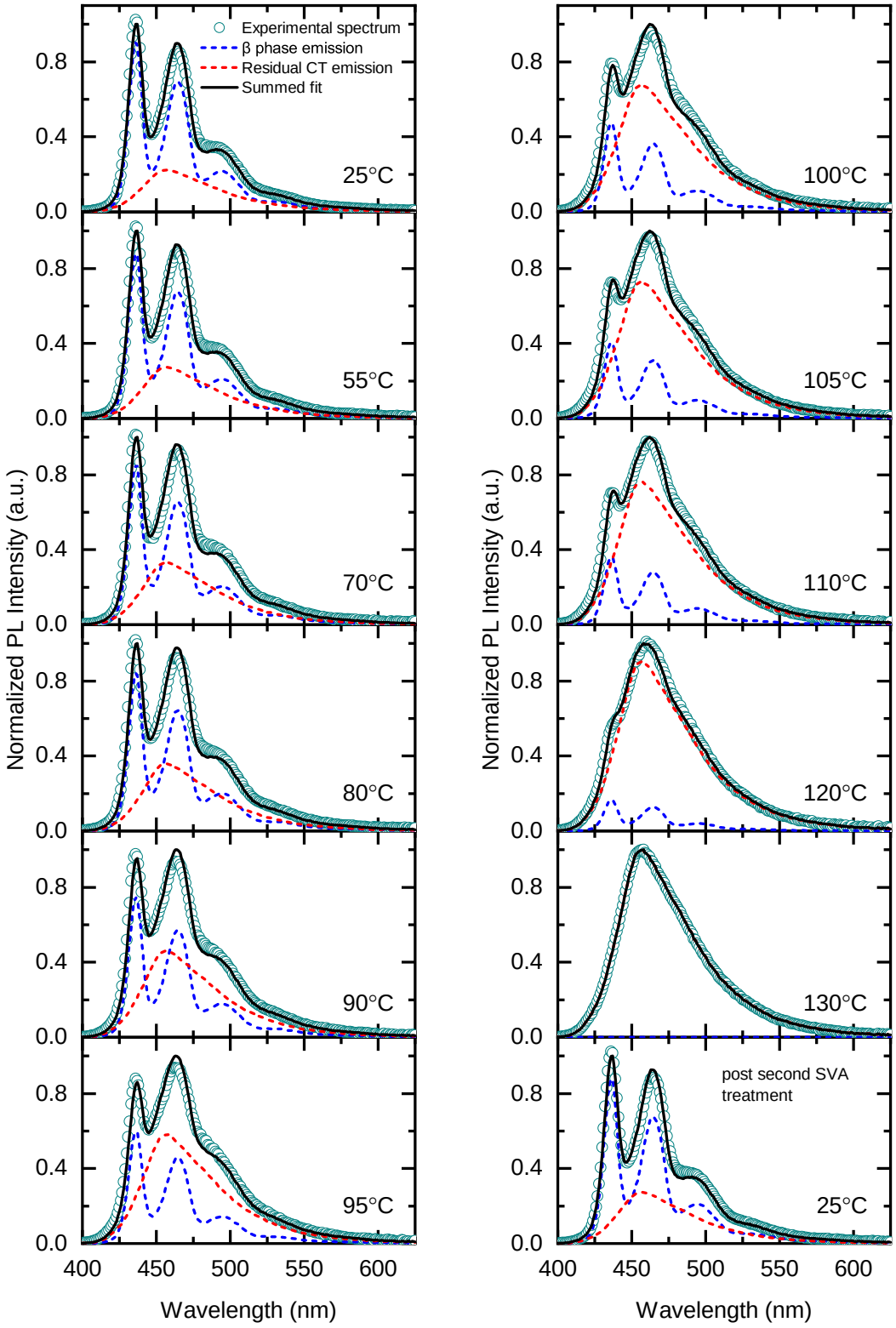


Figure A.3: PL spectra deconvolutions for 95F8:5BSP solvent vapour annealed (SVA) film before and after thermal annealing for 10 minutes at 55, 70, 80, 90, 95, 100, 105, 110, 120 and 130 °C. The spectrum following a second solvent vapour annealing treatment is also presented. The dashed red line gives the residual PFB-like CT emission while the dashed blue line shows the vibronic β phase contribution. The black solid line is the combined sum of both while the open green circles show the experimentally measured PL spectra.

A.2 Dark Injection Transient Measurements

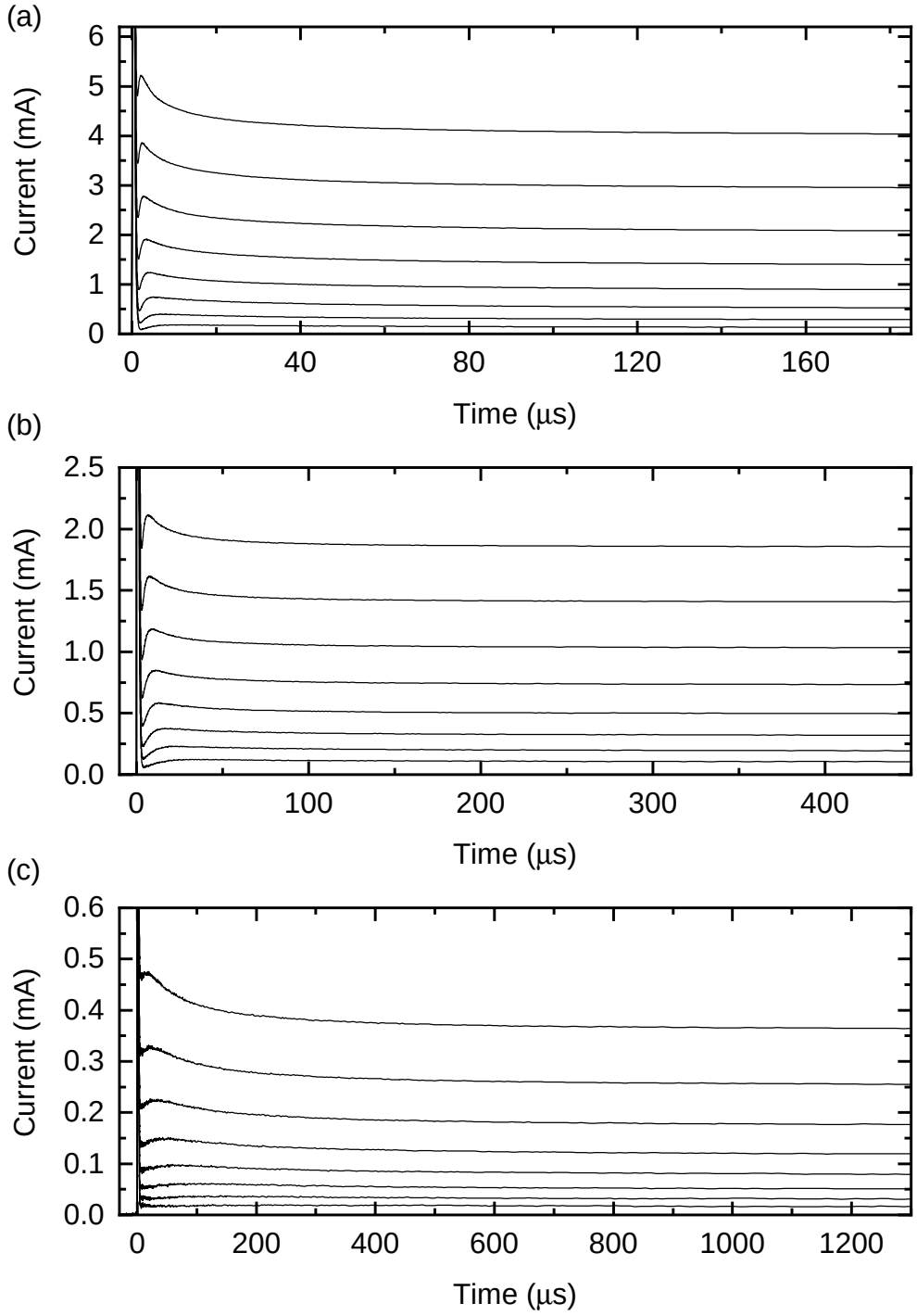


Figure A.4: Representative hole injection transients for glassy phase (a) 280 nm thick film of 80F8:20BSP, (b) 160 nm thick film of 90F8:10BSP and (c) 105 nm thick film of 95F8:5BSP under voltage pulses from bottom to top of 5, 6, 7, 8, 9, 10, 11 and 12 V.

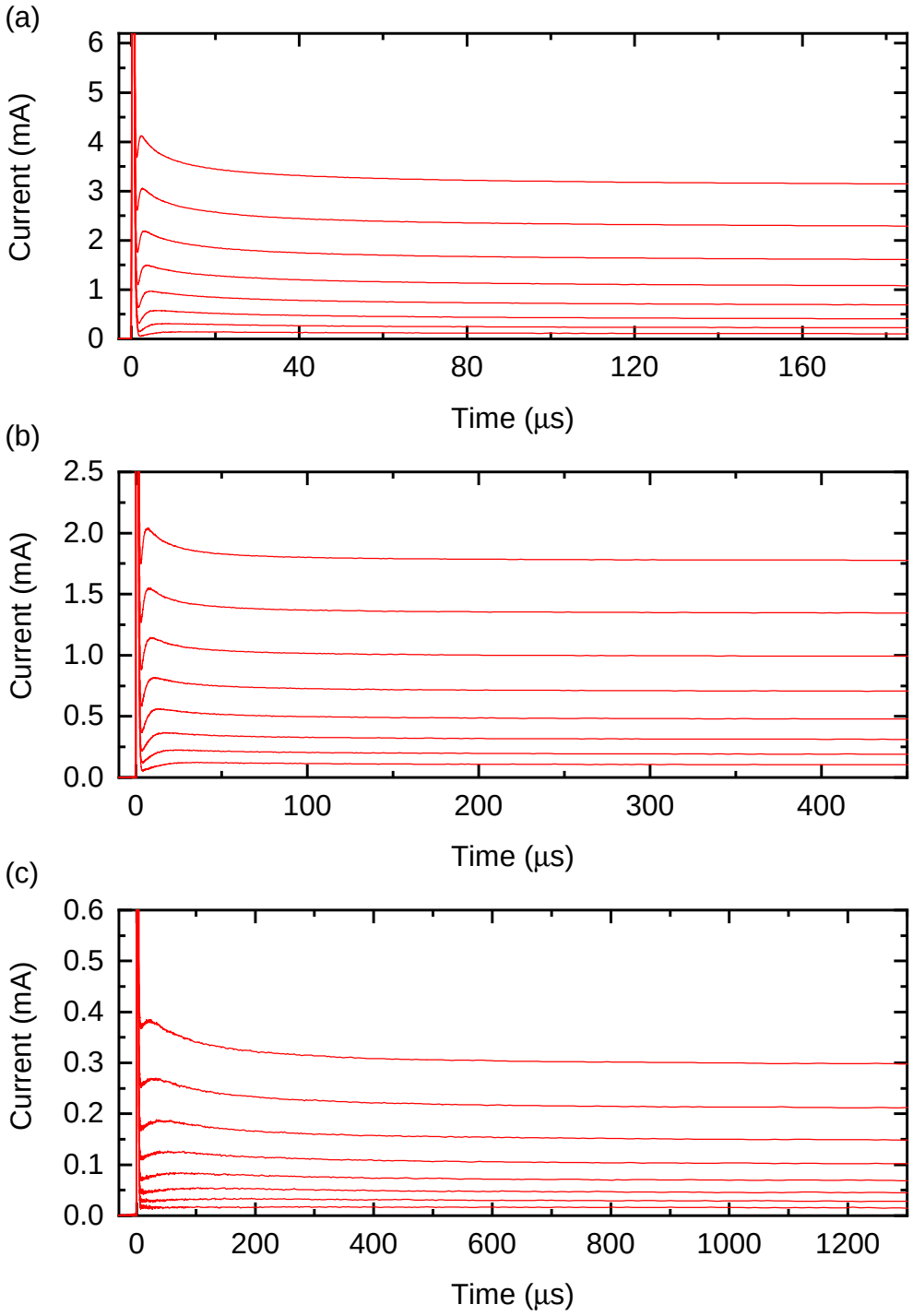


Figure A.5: Representative hole injection transients for β phase (a) 280 nm thick film of 80F8:20BSP, (b) 160 nm thick film of 90F8:10BSP and (c) 105 nm thick film of 95F8:5BSP under voltage pulses from bottom to top of 5, 6, 7, 8, 9, 10, 11 and 12 V.

A.3 Current-Voltage Characteristics

Commonly current-voltage (IV) characteristics of single carrier devices are used to deduce charge carrier mobility via fitting to a space-charge-limited current (SCLC) model. It is based on the concept of unipolar injection of charge carriers from an ohmic contact into the bulk of a semiconductor. When a high density of charge carriers is injected from the contact into the semiconductor, a space charge region is formed which alters the subsequent flow of charge carriers [175]. The idealized expression which assumes diffusion free currents, ohmic contacts and unipolar charge carriers is called *Child's law for unipolar SCL current*, also known as the *Mott-Gurney equation* [9]. The expression is given by

$$j = \frac{9}{8}\varepsilon_r\varepsilon_0\mu\frac{V^2}{d^3}, \tag{A.1}$$

where j denotes the current density, $\varepsilon_r\varepsilon_0$ is the dielectric constant, μ is the charge carrier mobility, V is the applied voltage and d is the sample thickness. Therefore, the mobility can be obtained by fitting equation A.1 to the measured IV curve in the region where $j \propto V^2$ (slope of double logarithmic IV plot (log(I)-log(V)), m, is equal to 2). However, this expression is strictly valid only if the charge carrier mobility is field independent because a field dependence would have a feedback effect on the spatial distribution of space charge. Additionally, equation A.1 assumes an undoped trap free semiconductor. Alternative models to fit SCLC data have been developed to account for non-ideal behaviour such as Rose's [176] and Lampert's [177] equation for a single discrete trap level and the Mark-Helfrich equation for an exponential trap density distribution. Rose's and Lampert's current voltage relation is given by

$$j = \frac{9}{8}\varepsilon_r\varepsilon_0\mu\theta\frac{V^2}{d^3}. \tag{A.2}$$

It is essentially the Mott-Gurney equation scaled with a factor θ ($\theta \leq 1$). This reflects the reduction in the current as injected carriers are captured by traps and do not participate in charge transport (the slope $m = 2$ is preserved). Mark

and Helfrich [178] developed an analytic expression for the case of an exponential trap density distribution of the form

$$n(E_t) = \frac{N_t}{kT_c} \exp\left(-\frac{E_t}{kT_c}\right), \tag{A.3}$$

with $\frac{T_C}{T} = l > 1$. T_c is a measure of the steepness of the distribution and N_t is the total density of traps. E_t is the energetic depth of the trap, defined as the energy difference between the energy level of the trap and the electron affinity (for electron traps) or ionization potential (for hole traps). For such a trap distribution $j(V) \propto \frac{V^{l+1}}{d^{2l+1}}$. This is observed as a steeper slope on the log(I)-log(V) plot ($m > 2$). For a Gaussian trap distribution an exact analytic expression for the SCL current does not exist and the Poisson and continuity equations need to be evaluated numerically [179]. Numerical calculations [179] and drift diffusion models [180] have shown that the SCL current in this case is not linear on a log(I)-log(V) plot. It depends on both the width of the distribution as well as the trap depth. The slope m depends on the part of the Gaussian trap DOS (for example tail or peak) being filled during a voltage sweep. Finally, we note that if the charge carrier concentration in the diode exceeds the number of traps, there is transition from trap-limited SCL transport to trap-free transport. At this point all traps are filled and all additional charge carriers contribute to the transport leading to a rapid increase of the current towards the trap-free SCLC. For a Gaussian distribution, this change is more gradual due to the broadness of the trap distribution and for broad trap distributions this transition can become indistinguishable from the rest of the IV curve.

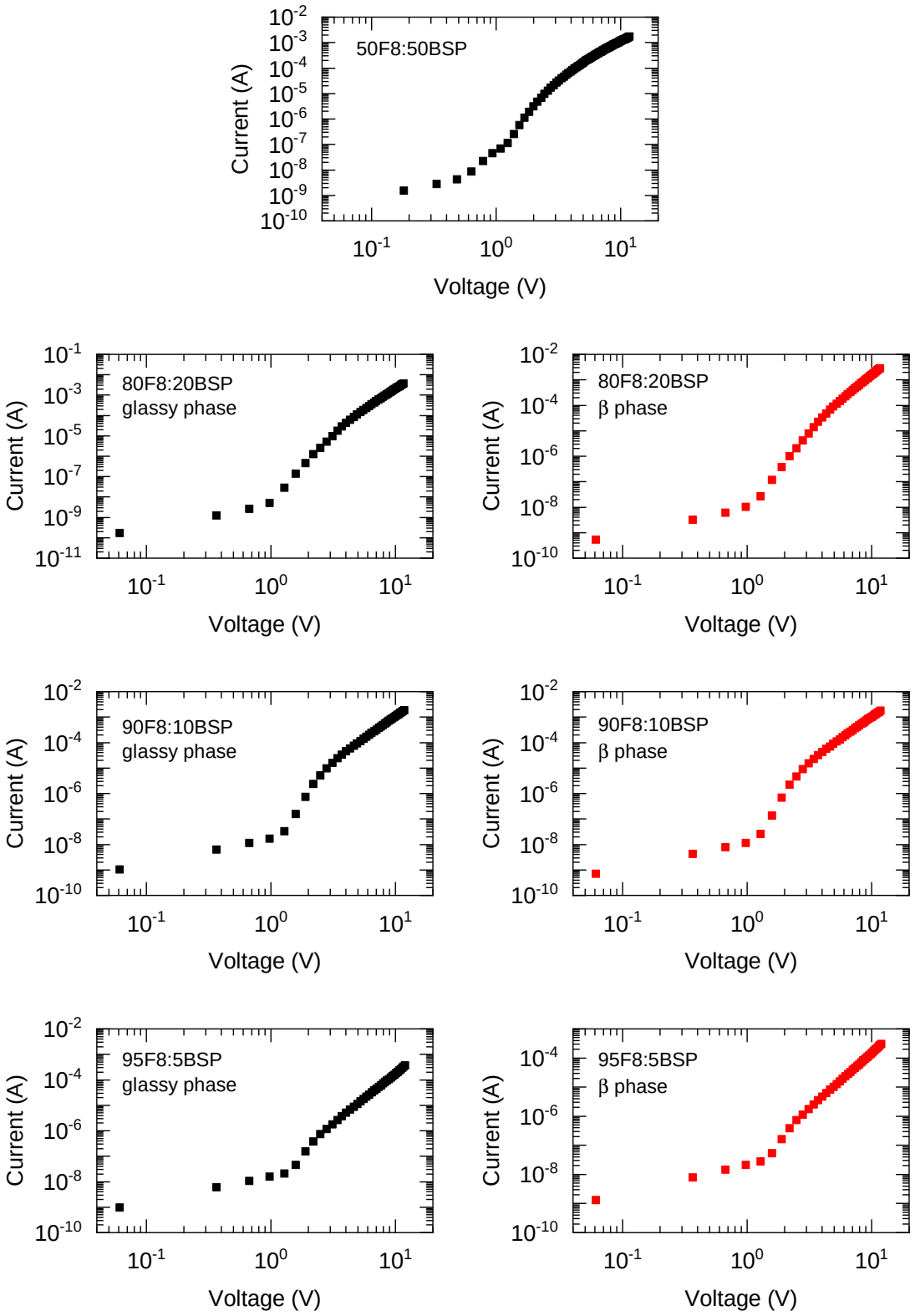


Figure A.6: Current-voltage curves for hole-only devices made in a sandwich structure of ITO/PEDOT:PSS/Copolymer/Al with 820 nm thick film of 50F8:50BSP, 280 nm thick film of 80F8:20BSP, 160 nm thick film of 90F8:10BSP and 105 nm thick film of 95F8:5BSP. Black squares correspond to hot spun films while red squares are used for solvent vapour annealed copolymer films.

Figure A.6 shows representative current-voltage curves on a double logarithmic scale for the hole-only copolymer DIT devices. An S-shaped dependence is seen in all plots. Below 1 V the slope of the curves is $m \sim 1$ while above that it increases steeply with $m > 2$. This suggests that the observed transport is trap-limited by a Gaussian trap distribution. While $m > 2$ is attributed to charge trapping, the $m \sim 1$ slope at low voltages is due to leakage current caused by parasitic currents between the electrodes. For the accurate determination of both hole carrier mobility and trap parameters a numerical device model is necessary and careful analysis using drift diffusion simulations would be required. Such investigations can constitute future work on this topic and reveal more about the trapping process in these copolymers.

B

Platinum-complex Copolymerisation

B.1 Materials

The material details presented in this section have been kindly provided by Xuyu Gao and Professor Youtian Tao from Nanjing Tech University.

Material	M_w ($\mathrm{g\,mol^{-1}}$)	PDI
Pt 0.5%	68×10^3	2.0
Pt 1%	78×10^3	1.9
Pt 2.5%	73×10^3	1.9
Pt 5%	74×10^3	2.3
Ligand 0.5%	130×10^3	1.9
Ligand 1%	137×10^3	2.1
Ligand 2.5%	171×10^3	1.7
Ligand 5%	66×10^3	1.9

Table B.1: Weight-average molecular weight, M_w, and polydispersity index, PDI, of the Pt-containing fluorene copolymers and corresponding organic ligand copolymers.

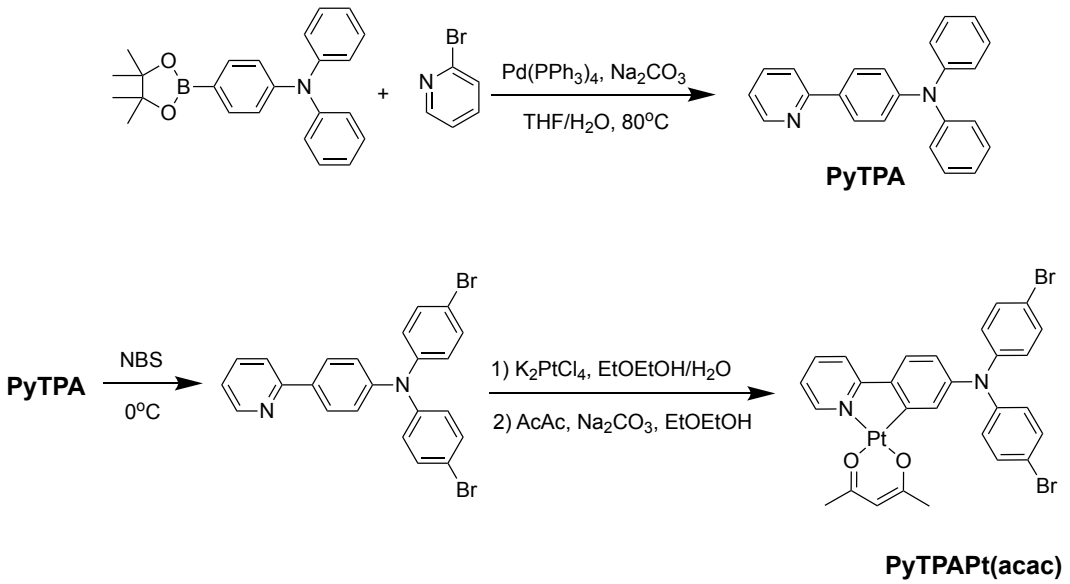


Figure B.1: Synthetic route to PyTPA ligand and PyTPAPt(acac) complex.

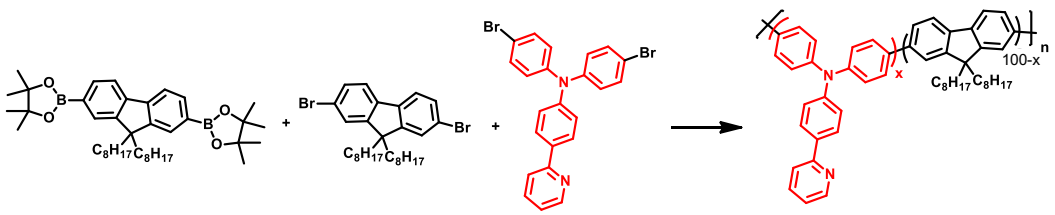


Figure B.2: Synthetic route to polyfluorene copolymer with organic PyTPA ligand ($x = 0.5$, 1, 2.5 and 5%).

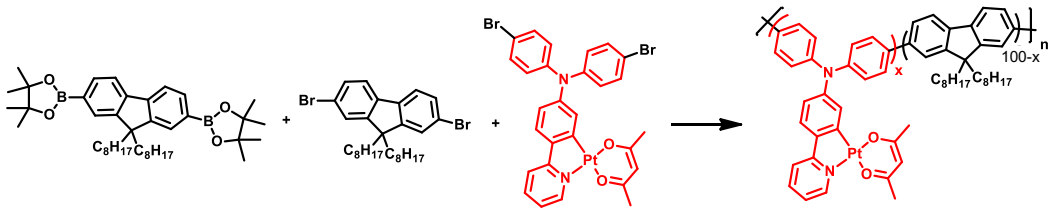


Figure B.3: Synthetic route to polyfluorene copolymer with cyclometalated PyTPAPt(acac) complex ($x = 0.5$, 1, 2.5 and 5%).

B.2 Cyclometalated PyTPAPt(acac) Complex and Organic PyTPA Ligand

Absorption and Photoluminescence Spectra

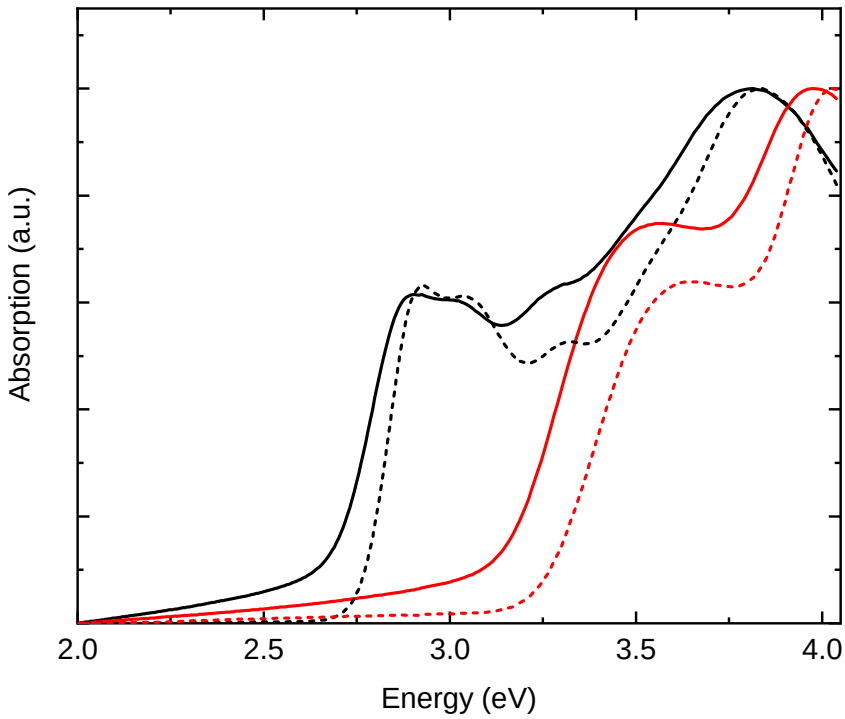


Figure B.4: The absorption spectra of the cyclometalated PyTPAPt(acac) complex (black lines) and organic PyTPA ligand (red lines) monomers in thin films (solid lines) and chloroform solutions (dashed lines).

The absorption spectra of the cyclometalated PyTPAPt(acac) complex and organic PyTPA ligand monomers in thin films and chloroform solutions (concentration $1.67 \times 10^{-8}\,\mathrm{mol\,L^{-1}}$) are presented in figure B.4 while their photoluminescence spectra are displayed in figure B.5. The PL spectra were excited at 3.26 eV for the cyclometalated PyTPAPt(acac) complex and 3.54 eV for the organic PyTPA ligand. The spectra have been measured by Xuyu Gao from Professor Youtian Tao's group in Nanjing Tech University.

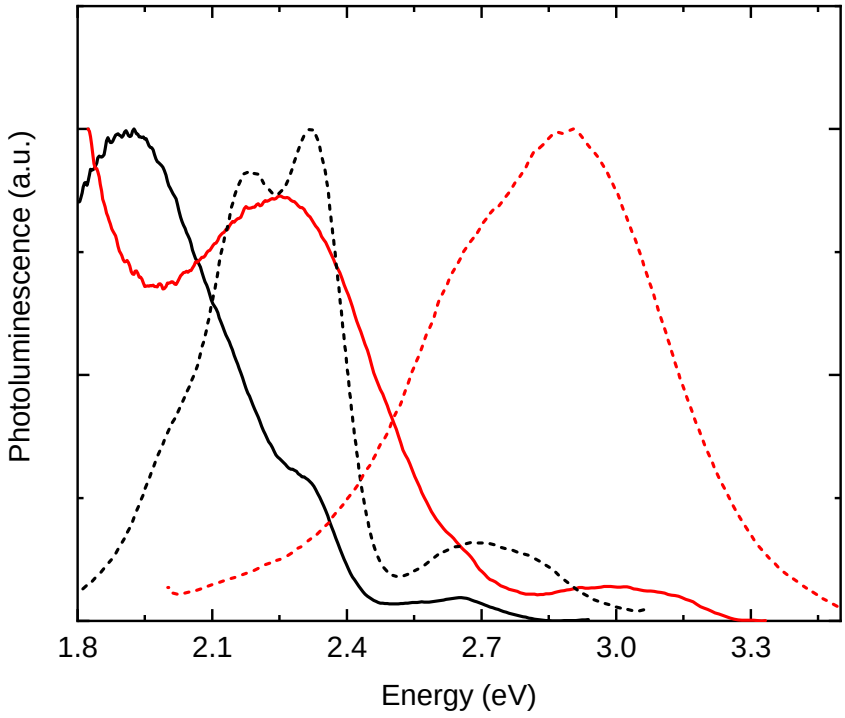


Figure B.5: The photoluminescence spectra of the cyclometalated PyTPAPt(acac) complex (black lines) and organic PyTPA ligand (red lines) monomers in thin films (solid lines) and chloroform solutions (dashed lines).

B.3 Temperature Dependence of Copolymer Photoluminescence Spectra

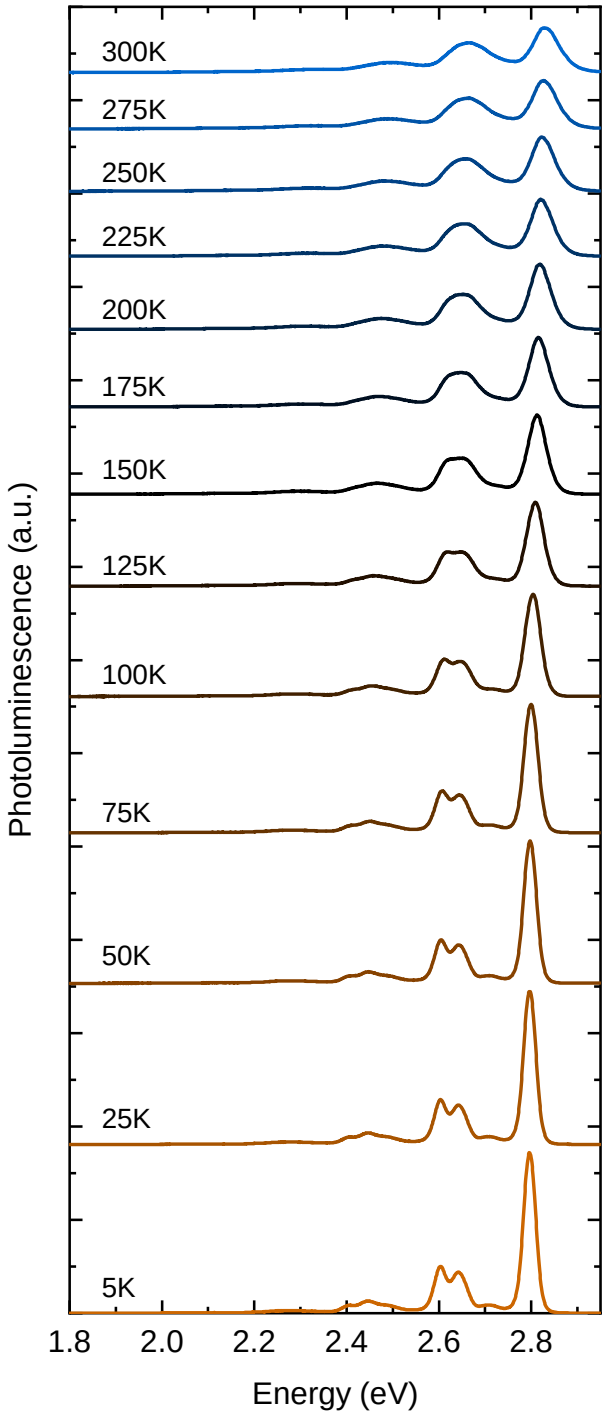


Figure B.6: The temperature dependence of the thin film photoluminescence of β phase PFO. The spectra have been displaced along the vertical axis for ease of comparison.

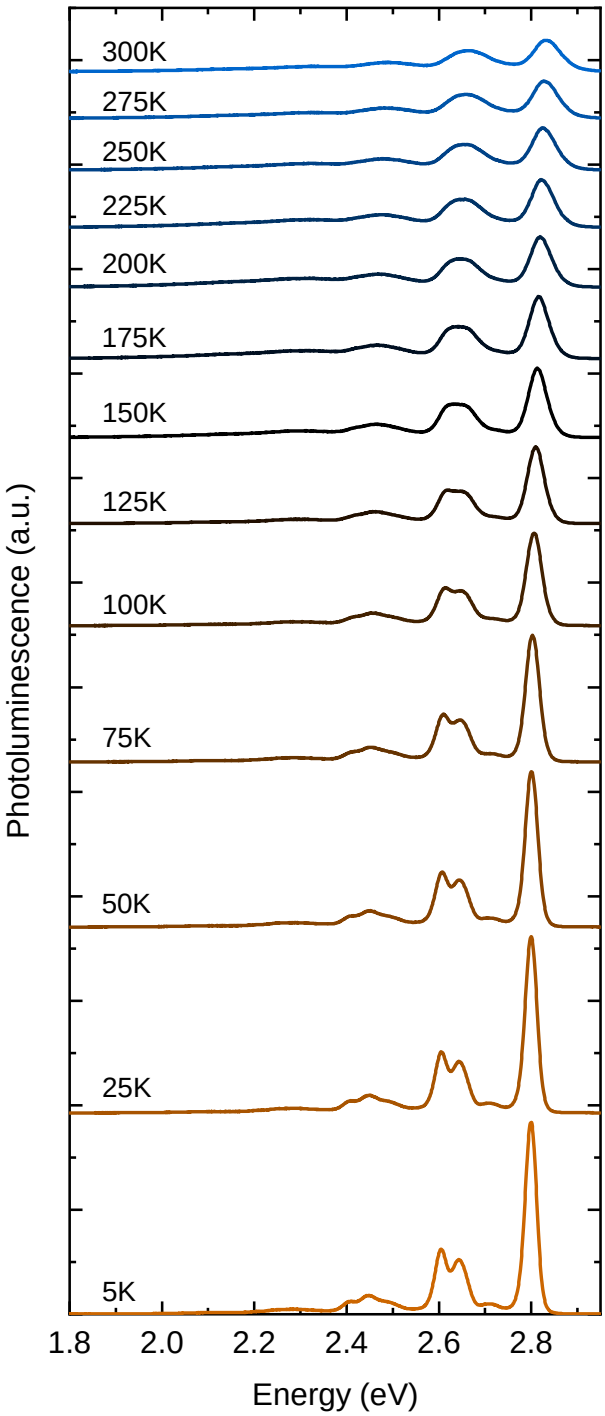


Figure B.7: The temperature dependence of the thin film photoluminescence of β phase 5% ligand copolymer. The spectra have been displaced along the vertical axis for ease of comparison.

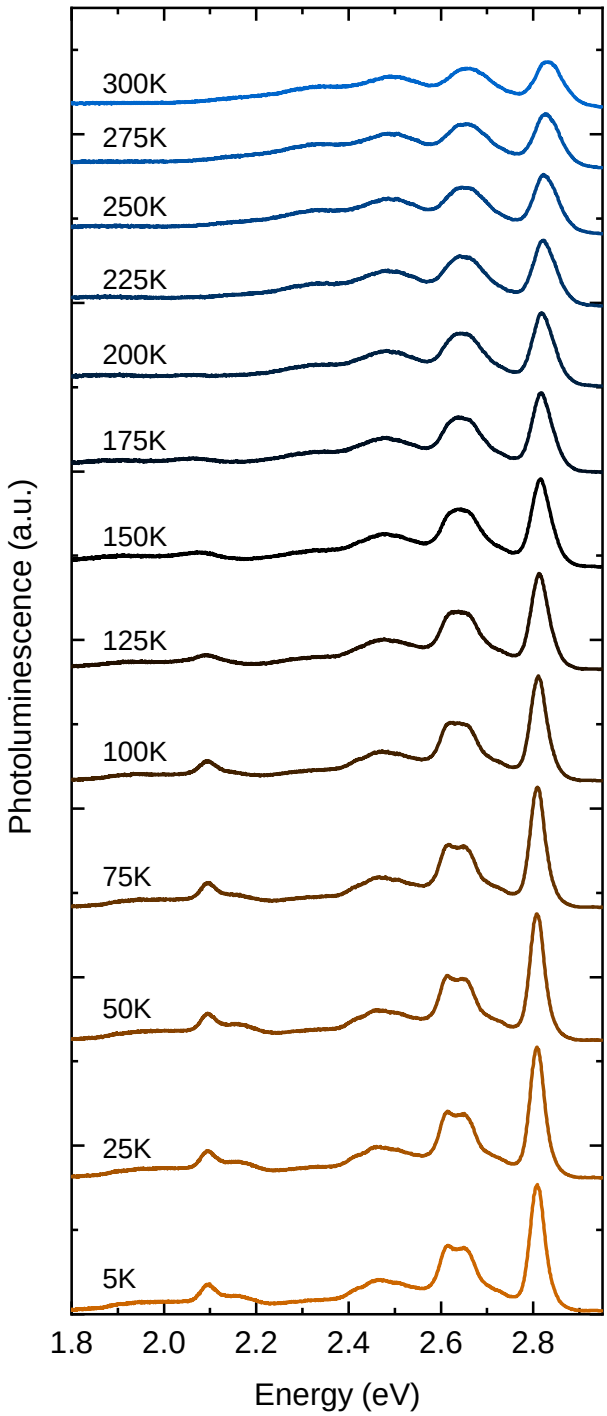


Figure B.8: The temperature dependence of the thin film photoluminescence of β phase 5% Pt copolymer. The spectra have been displaced along the vertical axis for ease of comparison.

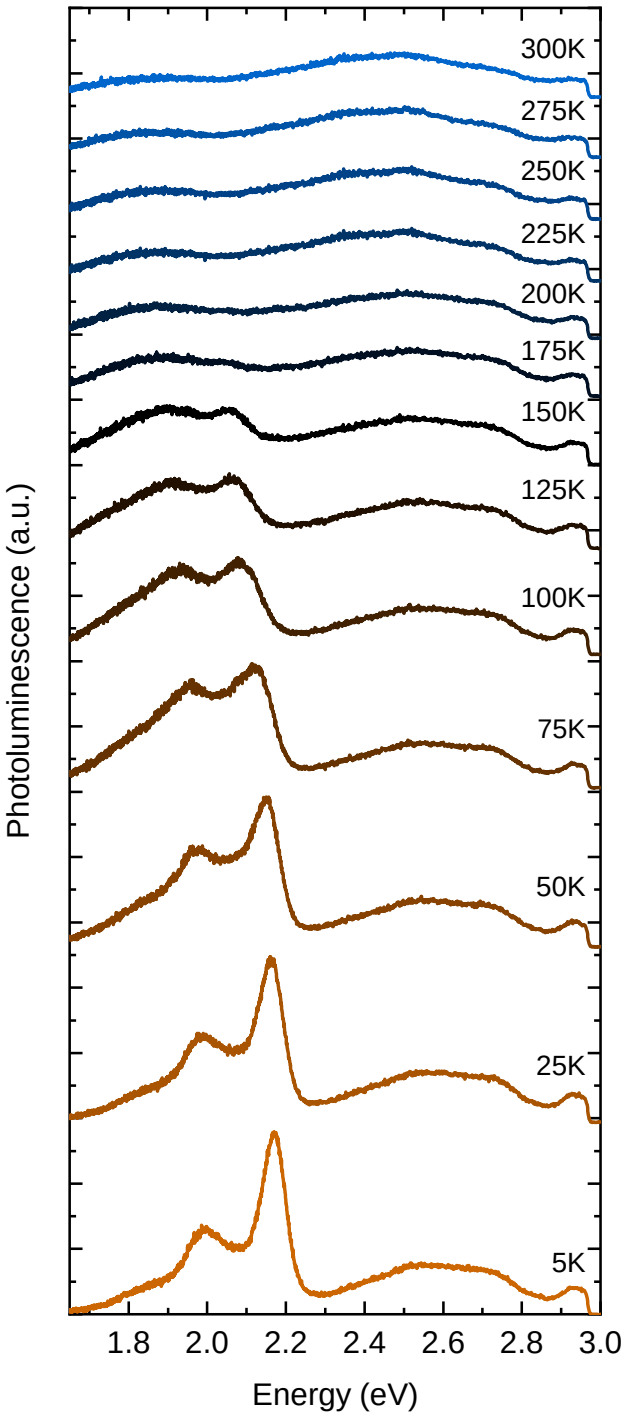


Figure B.9: The temperature dependence of the thin film photoluminescence of glassy phase 5% Pt copolymer. The spectra have been displaced along the vertical axis for ease of comparison.

References

[1] H. Shirakawa et al. “Electical Conductivity in Doped Polyacetylene”. In: *Physical Review Letters* 39.17 (1977), pp. 1098–1101.

[2] J. H. Burroughes et al. “Light-emitting diodes based on conjugated polymers”. In: *Nature* 347.6293 (1990), pp. 539–541.

[3] M. Ariu et al. “The effect of morphology on the temperature-dependent photoluminescence quantum efficiency of the conjugated polymer poly(9, 9-dioctylfluorene)”. In: *Journal of Physics Condensed Matter* 14.42 (2002), pp. 9975–9986.

[4] M. Redecker et al. “Nondispersive hole transport in an electroluminescent polyfluorene”. In: *Applied Physics Letters* 73.11 (1998), pp. 1565–1567.

[5] M. Ariu et al. “Exciton migration in β-phase poly(9,9-dioctylfluorene)”. In: *Physical Review B - Condensed Matter and Materials Physics* 67.19 (2003), pp. 1–11.

[6] M. Grell et al. “Interplay of physical structure and photophysics for a liquid crystalline polyfluorene”. In: *Macromolecules* 32.18 (1999), pp. 5810–5817.

[7] A. Köhler and H. Bässler. *Electronic Processes in Organic Semiconductors*. Weinheim, Germany: Wiley-VCH Verlag GmbH, 2015.

[8] P. Atkins and R. Friedman. *Molecular Quantum Mechanics*. 5th edn. Oxford, United Kingdom: Oxford University Press, 2010.

[9] M. Pope and C. E. Swenberg. *Electronic Processes in Organic Crystals and Polymers*. 2nd edn. Oxford, United Kingdom: Oxford University Press, 1999.

[10] W. Demtröder. *Molecular Physics*. Weinheim, Germany: Wiley-VCH Verlag GmbH, 2005.

[11] A. Perevedentsev. “Chain Conformation and the Photophysics of Polyfluorenes”. PhD thesis. Imperial College of Science, Technology and Medicine, London, UK, 2015.

[12] J. L. Bredas. “Mind the gap!” In: *Materials Horizons* 1.1 (2014), pp. 17–19.

[13] J. Rissler. “Effective conjugation length of π-conjugated systems”. In: *Chemical Physics Letters* 395.1-3 (2004), pp. 92–96.

[14] J. S. Wilson. “Triplet States in Platinum-Containing Conjugated Polymers”. PhD thesis. University of Cambridge, 2001.

[15] A. Köhler et al. “The singlet-triplet energy gap in organic and Pt-containing phenylene ethynylene polymers and monomers”. In: *Journal of Chemical Physics* 116.21 (2002), pp. 9457–9463.

[16] A. P. Monkman et al. “The effect of conjugation length on triplet energies, electron delocalization and electron-electron correlation in soluble polythiophenes”. In: *Journal of Chemical Physics* 115.19 (2001), pp. 9046–9049.

[17] D. Hertel et al. “Phosphorescence in conjugated poly(para-phenylene)-derivatives”. In: *Advanced Materials* 13.1 (2001), pp. 65–70.

[18] A. Köhler and H. Bässler. “Triplet states in organic semiconductors”. In: *Materials Science and Engineering R: Reports* 66.4-6 (2009), pp. 71–109.

[19] M. A. Baldo et al. “Excitonic singlet-triplet ratio in a semiconducting organic thin film”. In: *Physical Review B - Condensed Matter and Materials Physics* 60.20 (1999), pp. 14422–14428.

[20] A. S. Dhoot and N. C. Greenham. “Triplet formation in polyfluorene devices”. In: *Advanced Materials* 14.24 (2002), pp. 1834–1837.

[21] M. Wohlgenannt et al. “Formation cross-sections of singlet and triplet excitons in π-conjugated polymers”. In: *Nature* 409.6819 (2001), pp. 494–497.

[22] J. S. Wilson et al. “Spin-dependent exciton formation in π-conjugated compounds”. In: *Nature* 413.6858 (2001), pp. 828–831.

[23] B. H. Wallikewitz et al. “Triplet dynamics in fluorescent polymer light-emitting diodes”. In: *Physical Review B - Condensed Matter and Materials Physics* 85.4 (2012), pp. 22–25.

[24] G. W. Robinson and R. P. Frosch. “Electronic excitation transfer and relaxation”. In: *The Journal of Chemical Physics* 38.5 (1963), pp. 1187–1203.

[25] W. Siebrand. “Radiationless Transitions in Polyatomic Molecules. I. Calculation of Franck-Condon Factors”. In: *The Journal of Chemical Physics* 46.2 (1967), pp. 440–447.

[26] R. Englman and J. Jortner. “The energy gap law for radiationless transitions in large molecules”. In: *Molecular Physics* 18.2 (1970), pp. 285–287.

[27] J. S. Wilson et al. “The energy gap law for triplet states in pt-containing conjugated polymers and monomers”. In: *Journal of the American Chemical Society* 123.38 (2001), pp. 9412–9417.

[28] T. Förster. “10th Spiers Memorial Lecture. Transfer mechanisms of electronic excitation”. In: *Discuss. Faraday Soc.* 27 (1959), pp. 7–17.

[29] D. L. Dexter. “A theory of sensitized luminescence in solids”. In: *The Journal of Chemical Physics* 21.5 (1953), pp. 836–850.

[30] E. Zojer et al. “Green emission from poly(fluorene)s: The role of oxidation”. In: *Journal of Chemical Physics* 117.14 (2002), pp. 6794–6802.

[31] S. I. Hintschich et al. “Population and decay of keto states in conjugated polymers”. In: *Journal of Chemical Physics* 119.22 (2003), pp. 12017–12022.

[32] L. Romaner et al. “The influence of keto defects on photoexcitation dynamics in polyfluorene”. In: *Synthetic Metals* 139.3 (2003), pp. 851–854.

[33] A. P. Monkman et al. “Triplet Energies of pi-Conjugated Polymers”. In: *Physical Review B* 86.7 (2001), pp. 1358–1361.

[34] W. Warta and N. Karl. “Hot holes in naphthalene: High, electric-field-dependent mobilities”. In: *Physical Review B* 32.2 (1985), pp. 1172–1182.

[35] L. B. Schein, C. B. Duke, and A. R. McGhie. “Observation of the band-hopping transition for electrons in naphthalene”. In: *Physical Review Letters* 40.3 (1978), pp. 197–200.

[36] D. T. James. “Developing Structural Probes for Designed Molecular Architectures”. PhD thesis. Imperial College of Science, Technology and Medicine, London, UK, 2012.

[37] T. Holstein. “Studies of polaron motion Part II. The "Small" Polaron”. In: *Annals of Physics* 8.3 (1959), pp. 343–389.

[38] H. Bässler. “Charge Transport in Disordered Organic Photoconductors a Monte Carlo Simulation Study”. In: *Physica Status Solidi (B)* 175.1 (1993), pp. 15–56.

[39] A. Miller and E. Abrahams. “Impurity conduction at low concentrations”. In: *Physical Review* 120.3 (1960), pp. 745–755.

[40] S. V. Novikov and A. V. Vannikov. “Cluster structure in the distribution of the electrostatic potential in a lattice of randomly oriented dipoles”. In: *Journal of Physical Chemistry* 99.40 (1995), pp. 14573–14576.

[41] S. V. Novikov et al. “Essential Role of Correlations in Governing Charge Transport in Disordered Organic Materials”. In: *Physical Review Letters* 81.20 (1998), pp. 4472–4475.

[42] T. Kreouzis et al. “Temperature and field dependence of hole mobility in poly(9,9-dioctylfluorene)”. In: *Physical Review B - Condensed Matter and Materials Physics* 73.23 (2006), pp. 1–15.

[43] H. H. Lu et al. “Self-dopant formation in poly(9,9-di-n-octylfluorene) via a dipping method for efficient and stable pure-blue electroluminescence”. In: *Advanced Materials* 19.18 (2007), pp. 2574–2579.

[44] B. K. Yap et al. “Simultaneous optimization of charge-carrier mobility and optical gain in semiconducting polymer films”. In: *Nature Materials* 7.5 (2008), pp. 376–380.

[45] Q. Zhao, S. J. Liu, and W. Huang. “Polyfluorene-based blue-emitting materials”. In: *Macromolecular Chemistry and Physics* 210.19 (2009), pp. 1580–1590.

[46] A. Perevedentsev et al. “Dip-pen patterning of poly(9,9-dioctylfluorene) chain-conformation-based nano-photonic elements”. In: *Nature Communications* 6.5977 (2015), pp. 1–9.

[47] Q. Zhang et al. “An easy approach to control β-phase formation in PFO films for optimized emission properties”. In: *Molecules* 22.2 (2017), pp. 1–8.

[48] W. Chunwaschirasiri et al. “Chain conformations and photoluminescence of poly(di-n-octylfluorene)”. In: *Physical Review Letters* 94.10 (2005), pp. 3–6.

[49] A. L. T. Khan et al. “Morphology-dependent energy transfer within polyfluorene thin films”. In: *Physical Review B - Condensed Matter and Materials Physics* 69.8 (2004), pp. 1–8.

[50] M. Ariu et al. “Study of the different structural phases of the polymer poly(9,9-dioctyl fluorene) using Raman spectroscopy”. In: *Synthetic Metals* 116.1-3 (2001), pp. 217–221.

[51] M. Ariu, D. G. Lidzey, and D. D. C. Bradley. “Influence of film morphology on the vibrational spectra of dioctyl substituted polyfluorene (PFO)”. In: *Synthetic Metals* 111-112 (2000), pp. 607–610.

[52] M. Grell et al. “Chain geometry, solution aggregation and enhanced dichroism in the liquid-crystalline conjugated polymer poly(9,9-dioctylfluorene)”. In: *Acta Polymerica* 49.8 (1998), pp. 439–444.

[53] A. Perevedentsev et al. “Solution-crystallization and related phenomena in 9,9-dialkyl-fluorene polymers. I. Crystalline polymer-solvent compound formation for poly(9,9-dioctylfluorene)”. In: *Journal of Polymer Science, Part B: Polymer Physics* 53.21 (2015), pp. 1481–1491.

[54] M. C. Chen et al. “Nanoscale ordered structure distribution in thin solid film of conjugated polymers: Its significance in charge transport across the film and in performance of electroluminescent device”. In: *Journal of Physical Chemistry B* 113.32 (2009), pp. 11124–11133.

[55] M. E. Caruso and M. Anni. “Real-time investigation of solvent swelling induced β -phase formation in poly(9,9-dioctylfluorene)”. In: *Physical Review B - Condensed Matter and Materials Physics* 76.5 (2007), pp. 1–4.

[56] G. Ryu, P. N. Stavrinou, and D. D. C. Bradley. “Spatial patterning of the β-phase in poly(9,9-dioctylfluorene): A metamaterials-inspired molecular conformation approach to the fabrication of polymer semiconductor optical structures”. In: *Advanced Functional Materials* 19.20 (2009), pp. 3237–3242.

[57] J. Peet et al. “Controlled β-phase formation in poly(9,9-di-n-octylfluorene) by processing with alkyl additives”. In: *Advanced Materials* 20.10 (2008), pp. 1882–1885.

[58] M. Grell et al. “Interplay of physical structure and photophysics for a liquid crystalline polyfluorene”. In: *Macromolecules* 32.18 (1999), pp. 5810–5817.

[59] S. H. Chen et al. “Crystalline forms and emission behavior of poly(9,9-di-n-octyl-2,7-fluorene)”. In: *Macromolecules* 38.2 (2005), pp. 379–385.

[60] M. Grell et al. “A Glass-Forming Conjugated Main-Chain Liquid Crystal Polymer for Polarized Electroluminescence Applications”. In: *Advanced Materials* 9.10 (1997), pp. 798–802.

[61] M. Sims et al. “On the use of optical probes to monitor the thermal transitions in spin-coated poly(9,9-dioctylfluorene) films”. In: *Journal of Physics Condensed Matter* 17.41 (2005), pp. 6307–6318.

[62] J. Mooney and P. Kambhampati. “Get the basics right: Jacobian conversion of wavelength and energy scales for quantitative analysis of emission spectra”. In: *Journal of Physical Chemistry Letters* 4.19 (2013), pp. 3316–3318.

[63] S. H. Chen, A. C. Su, and S. A. Chen. “Noncrystalline phases in poly(9,9-di-n-octyl-2,7-fluorene)”. In: *Journal of Physical Chemistry B* 109.20 (2005), pp. 10067–10072.

[64] U. Scherf and E. J. W. List. "Semiconducting polyfluorenes - towards reliable structure-property relationships". In: *Advanced Materials* 14.7 (2002), pp. 477–487.

[65] A. L. T. Khan, M. J. Banach, and A. Köhler. "Control of β-phase formation in polyfluorene thin films via Franck-Condon analysis". In: *Synthetic Metals* 139.3 (2003), pp. 905–907.

[66] T. Virgili et al. "Ultrafast resonant optical switching in isolated polyfluorenes chains". In: *Applied Physics Letters* 86.9 (2005), pp. 1–3.

[67] A. D. Jenkins and K. L. Loening. "Nomenclature". In: *Comprehensive Polymer Science and Supplements*. Oxford, United Kingdom: Pergamon Press, 1989, pp. 13–54.

[68] L. D. Bonifacio, B. V. Lotsch, and G. A. Ozin. "Periodic Mesoporous Materials: Holes Filled with Opportunities". In: *Comprehensive Nanoscience and Technology*. Academic Press, 2011, pp. 69–125.

[69] T. Yamamoto et al. "Preparation of π-Conjugated poly(thiophene-2,5-diyl), poly(p-phenylene), and related polymers using zero valent nickel-complexes-Linear structure and properties of the π-conjugated polymers". In: *Macromolecules* 25.4 (1992), pp. 1214–1223.

[70] N. Miyaura and A. Suzuki. "Palladium-Catalyzed Cross-Coupling Reactions of Organoboron Compounds". In: *Chemical Reviews* 95.7 (1995), pp. 2457–2483.

[71] F. B. Dias, T. J. Penfold, and A. P. Monkman. "Photophysics of thermally activated delayed fluorescence molecules". In: *Methods and Applications in Fluorescence* 5.012001 (2017), pp. 1–25.

[72] J. De Mello, H. F. Wittmann, and R. H. Friend. "An Improved Experimental Determination of External Photoluminescence Quantum Efficiency". In: *Advanced Materials* 9.3 (1997), pp. 230–232.

[73] A. Many and G. Rakavy. "Theory of Transient Space-Charge-Limited Currents in Solids in the Presence of Trapping". In: *Physical review* 126.6 (1962), pp. 1980–1988.

[74] A. Kokil, K. Yang, and J. Kumar. "Techniques for characterization of charge carrier mobility in organic semiconductors". In: *Journal of Polymer Science, Part B: Polymer Physics* 50.15 (2012), pp. 1130–1144.

[75] J. R. Harwell et al. "Probing the energy levels of perovskite solar cells: Via Kelvin probe and UV ambient pressure photoemission spectroscopy". In: *Physical Chemistry Chemical Physics* 18.29 (2016), pp. 19738–19745.

[76] I. D. Baikie et al. "Dual Mode Kelvin Probe : featuring Ambient Pressure Photoemission Spectroscopy and Contact Potential Difference". In: *Energy Procedia* 60 (2014), pp. 48–56.

[77] I. D. Baikie et al. "Near ambient pressure photoemission spectroscopy of metal and semiconductor surfaces". In: *Physica Status Solidi (C) Current Topics in Solid State Physics* 12.3 (2015), pp. 259–262.

[78] M. Redecker et al. "High mobility hole transport fluorene-triarylamine copolymers". In: *Advanced Materials* 11.3 (1999), pp. 241–246.

[79] R. U. A. Khan et al. "Hole mobility within arylamine-containing polyfluorene copolymers: A time-of-flight transient-photocurrent study". In: *Physical Review B - Condensed Matter and Materials Physics* 75.3 (2007), pp. 1–14.

[80] H. H. Fong, A. Papadimitratos, and G. G. Malliaras. "Nondispersive hole transport in a polyfluorene copolymer with a mobility of 0.01 cm2V-1s-1". In: *Applied Physics Letters* 89.17 (2006), pp. 87–90.

[81] H. H. Fong et al. "Hole injection in a model fluorene-triarylamine copolymer". In: *Advanced Functional Materials* 19.2 (2009), pp. 304–310.

[82] I. Hamilton et al. "Controlling Molecular Conformation for Highly Efficient and Stable Deep-Blue Copolymer Light-Emitting Diodes". In: *ACS Applied Materials and Interfaces* 10.13 (2018), pp. 11070–11082.

[83] Y. Tamai et al. "Triplet exciton dynamics in fluorene-amine copolymer films". In: *Chemistry of Materials* 26.8 (2014), pp. 2733–2742.

[84] C. E. Richards and R. T. Phillips. "Solvatochromic effects on the photoinduced charge-transfer states in donor-acceptor substituted polydioctylfluorenes". In: *ChemPhysChem* 12.15 (2011), pp. 2831–2835.

[85] A. J. Cadby et al. "Film morphology and photophysics of polyfluorene". In: *Physical Review B - Condensed Matter and Materials Physics* 62.23 (2000), pp. 15604–15609.

[86] W. C. Tsoi et al. "Observation of the β-phase in two short-chain oligofluorenes". In: *Advanced Functional Materials* 18.4 (2008), pp. 600–606.

[87] M. Campoy-Quiles et al. "Thickness-dependent thermal transition temperatures in thin conjugated polymer films". In: *Macromolecules* 39.22 (2006), pp. 7673–7680.

[88] S. H. Chen et al. "Crystalline forms and emission behavior of poly(9,9-di-n-octyl-2,7-fluorene)". In: *Macromolecules* 38.2 (2005), pp. 379–385.

[89] P. S. Davids, I. H. Campbell, and D. L. Smith. "Device model for single carrier organic diodes". In: *Journal of Applied Physics* 82.12 (1997), pp. 6319–6325.

[90] G. Greczynski, T. Kugler, and W. R. Salaneck. "Characterization of the PEDOT-PSS system by means of X-ray and ultravioler photoelectron spectroscopy". In: *Thin Solid Films* 354.1-2 (1999), pp. 129–135.

[91] J. S. Kim et al. "Characterisation of the properties of surface-treated indium-tin oxide thin films". In: *Synthetic Metals* 101.1 (1999), pp. 111–112.

[92] T. M. Brown et al. "Built-in field electroabsorption spectroscopy of polymer light-emitting diodes incorporating a doped poly(3,4-ethylene dioxythiophene) hole injection layer". In: *Applied Physics Letters* 75.12 (1999), pp. 1679–1681.

[93] A. J. Campbell et al. "Transient and steady-state space-charge-limited currents in polyfluorene copolymer diode structures with ohmic hole injecting contacts". In: *Applied Physics Letters* 76.13 (2000), pp. 1734–1736.

[94] P. Prins et al. "Enhanced charge-carrier mobility in β -phase polyfluorene". In: *Physical Review B - Condensed Matter and Materials Physics* 74.11 (2006), pp. 10–12.

[95] S. Foster. "On the influence of physical and chemical structure on charge transport in disordered semiconducting materials and devices". PhD thesis. Imperial College of Science, Technology and Medicine, London, UK, 2013.

[96] D. Poplavskyy, J. Nelson, and D. D. C. Bradley. "Dispersive and non-dispersive hole transport in fluorene-arylamine copolymers". In: *Macromolecular Symposia* 212.1 (2004), pp. 415–420.

[97] W. D. Gill. "Drift mobilities in amorphous charge-transfer complexes of trinitrofluorenone and poly-n-vinylcarbazole". In: *Journal of Applied Physics* 43.12 (1972), pp. 5033–5040.

[98] Y. N. Gartstein and E. M. Conwell. "High-field hopping mobility in molecular systems with spatially correlated energetic disorder". In: *Chemical Physics Letters* 245.4-5 (1995), pp. 351–358.

[99] D. Poplavskyy, J. Nelson, and D. D. C. Bradley. "Ohmic hole injection in poly(9,9-dioctylfluorene) polymer light-emitting diodes". In: *Applied Physics Letters* 83.4 (2003), pp. 707–709.

[100] S. Janietz et al. "Electrochemical determination of the ionization potential and electron affinity of poly(9,9-dioctylfluorene)". In: *Applied Physics Letters* 73.17 (1998), pp. 2453–2455.

[101] T. Miteva et al. "Improving the performance of polyfluorene-based organic light-emitting diodes via end-capping". In: *Advanced Materials* 13.8 (2001), pp. 565–570.

[102] I. D. Baikie et al. "Ambient pressure photoemission spectroscopy of metal surfaces". In: *Applied Surface Science* 323 (2014), pp. 45–53.

[103] I. I. Fishchuk et al. "Transition from trap-controlled to trap-to-trap hopping transport in disordered organic semiconductors". In: *Physical Review B - Condensed Matter and Materials Physics* 73.11 (2006), pp. 1–11.

[104] A. Kadashchuk et al. "The origin of thermally stimulated luminescence in neat and molecularly doped charge transport polymer systems". In: *Chemical Physics* 247.2 (1999), pp. 307–319.

[105] D. H. Dunlap, P. E. Parris, and V. M. Kenkre. "Charge-Dipole Model for the Universal Field Dependence of Mobilities in Molecularly Doped Polymers". In: *Physical Review Letters* 77.3 (1996), pp. 542–545.

[106] D. M. Pai, J. F. Yanus, and M. Stolka. "Trap-controlled hopping transport". In: *Journal of Physical Chemistry* 88.20 (1984), pp. 4714–4717.

[107] P. M. Borsenberger et al. "Hole trapping in molecularly doped polymers: The hoesterey-letson formalism". In: *Japanese Journal of Applied Physics, Part 1: Regular Papers and Short Notes and Review Papers* 38.1A (1999), pp. 117–121.

[108] P. M. Borsenberger, E. H. Magin, and S. A. Visser. "Charge Trapping in Molecularly Doped Polymers". In: *Japanese Journal of Applied Physics, Part 1: Regular Papers and Short Notes and Review Papers* 37.4A (1998), pp. 1945–1949.

[109] D. Venkateshvaran et al. "Approaching disorder-free transport in high-mobility conjugated polymers". In: *Nature* 515.7527 (2014), pp. 384–388.

[110] V. Lemaur et al. “Resilience to Conformational Fluctuations Controls Energetic Disorder in Conjugated Polymer Materials: Insights from Atomistic Simulations”. In: *Chemistry of Materials* 31.17 (2019), pp. 6889–6899.

[111] H. Bronstein et al. “The role of chemical design in the performance of organic semiconductors”. In: *Nature Reviews Chemistry* 4.2 (2020), pp. 66–77.

[112] W. Zhang et al. “Indacenodithiophene semiconducting polymers for high-performance, air-stable transistors”. In: *Journal of the American Chemical Society* 132.33 (2010), pp. 11437–11439.

[113] J. S. Kim et al. “Phase Separation in Polyfluorene-Based Conjugated Polymer Blends: Lateral and Vertical Analysis of Blend Spin-Cast Thin Films”. In: *Macromolecules* 37.8 (2004), pp. 2861–2871.

[114] J. S. Kim et al. “Spin-cast thin semiconducting polymer interlayer for improving device efficiency of polymer light-emitting diodes”. In: *Applied Physics Letters* 87.2 (2005), pp. 28–31.

[115] J. Bailey et al. “Understanding the role of ultra-thin polymeric interlayers in improving efficiency of polymer light emitting diodes”. In: *Journal of Applied Physics* 115.20 (2014).

[116] Y. Zhu, A. Babel, and S. A. Jenekhe. “Phenoxazine-Based Conjugated Polymers : A New Class of Organic Semiconductors for Field-Effect Transistors”. In: *Macromolecules* 38.19 (2005), pp. 7983–7991.

[117] L. Yang et al. “Theoretical investigations on the modulation of the polymer electronic and optical properties by introduction of phenoxazine”. In: *Polymer* 47.9 (2006), pp. 3229–3239.

[118] M. Cheng et al. “A novel phenoxazine-based hole transport material for efficient perovskite solar cell”. In: *Journal of Energy Chemistry* 24.6 (2015), pp. 698–706.

[119] A. Perevedentsev et al. “Spectroscopic properties of poly(9,9-dioctylfluorene) thin films possessing varied fractions of β-phase chain segments: enhanced photoluminescence efficiency via conformation structuring”. In: *Journal of Polymer Science, Part B: Polymer Physics* 54.19 (2016), pp. 1995–2006.

[120] S. Gaisford, V. Kett, and P. Haines, eds. *Principles of Thermal Analysis and Calorimetry*. 2nd edn. Cambridge, United Kingdom: The Royal Society of Chemistry, 2016.

[121] C. Müller. “On the glass transition of polymer semiconductors and its impact on polymer solar cell stability”. In: *Chemistry of Materials* 27.8 (2015), pp. 2740–2754.

[122] M. Campoy-Quiles et al. “Thickness-dependent thermal transition temperatures in thin conjugated polymer films”. In: *Macromolecules* 39.22 (2006), pp. 7673–7680.

[123] D. Liu, R. O. Orozco, and T. Wang. “Deviations of the glass transition temperature in amorphous conjugated polymer thin films”. In: *Physical Review E - Statistical, Nonlinear, and Soft Matter Physics* 88.2 (2013), pp. 1–5.

[124] S. F. Alvarado et al. “Direct determination of the exciton binding energy of conjugated polymers using a scanning tunneling microscope”. In: *Physical Review Letters* 81.5 (1998), pp. 1082–1085.

[125] S. M. Gali et al. “Energetic fluctuations in amorphous semiconducting polymers: Impact on charge-carrier mobility”. In: *Journal of Chemical Physics* 147.13 (2017).

[126] J. C. Sancho-García et al. “Joint theoretical and experimental characterization of the structural and electronic properties of poly(dioctylfluorene-alt-N-butylphenyl diphenylamine)”. In: *Journal of Physical Chemistry B* 108.18 (2004), pp. 5594–5599.

[127] A. Berntsen et al. “Stability of polymer LEDs”. In: *Optical Materials* 9.1-4 (1998), pp. 125–133.

[128] S. A. Carter et al. “Polymeric anodes for improved polymer light-emitting diode performance”. In: *Applied Physics Letters* 70.16 (1997), pp. 2067–2069.

[129] D. Y. Chung et al. “Flexible multilayer inverted polymer light-emitting diodes with a gravure contact printed Cs2 CO3 electron injection layer”. In: *Applied Physics Letters* 98.10 (2011), pp. 2011–2014.

[130] A. R. Buckley et al. “Energy transfer dynamics in polyfluorene-based polymer blends”. In: *Chemical Physics Letters* 339.5-6 (2001), pp. 331–336.

[131] C. I. Wilkinson et al. “Enhanced performance of pulse driven small area polyfluorene light emitting diodes”. In: *Applied Physics Letters* 79.2 (2001), pp. 171–173.

[132] S. A. Choulis et al. “The effect of interfacial layer on the performance of organic light-emitting diodes”. In: *Applied Physics Letters* 87.11 (2005), pp. 1–4.

[133] J. Hwang et al. “Photoelectron spectroscopic study of the electronic band structure of polyfluorene and fluorene-arylamine copolymers at interfaces”. In: *Journal of Physical Chemistry C* 111.3 (2007), pp. 1378–1384.

[134] Z. Zhu et al. “Polyfluorene derivatives are high-performance organic hole-transporting materials for inorganic-organic hybrid perovskite solar cells”. In: *Advanced Functional Materials* 24.46 (2014), pp. 7357–7365.

[135] A. J. Campbell, D. D. C. Bradley, and H. Antoniadis. “Dispersive electron transport in an electroluminescent polyfluorene copolymer measured by the current integration time-of-flight method”. In: *Applied Physics Letters* 79.14 (2001), pp. 2133–2135.

[136] J. Zaumseil et al. “Quantum efficiency of ambipolar light-emitting polymer field-effect transistors”. In: *Journal of Applied Physics* 103.6 (2008).

[137] Y. Zhang and P. W. M. Blom. “Electron and hole transport in poly(fluorene-benzothiadiazole)”. In: *Applied Physics Letters* 98.14 (2011), pp. 96–99.

[138] J. S. Kim et al. “Spin-cast thin semiconducting polymer interlayer for improving device efficiency of polymer light-emitting diodes”. In: *Applied Physics Letters* 87.2 (2005), pp. 28–31.

[139] N. Chitraningrum et al. “Modulating the line shape of magnetoconductance by varying the charge injection in polymer light-emitting diodes”. In: *AIP Advances* 8.2 (2018).

[140] J. J. M. Halls et al. “Efficient photodiodes from interpenetrating polymer networks”. In: *Nature* 376.6540 (1995), pp. 498–500.

[141] A. C. Arias et al. “Photovoltaic performance and morphology of polyfluorene blends: A combined microscopic and photovoltaic investigation”. In: *Macromolecules* 34.17 (2001), pp. 6005–6013.

[142] Y. Cao et al. “Improved quantum efficiency for electroluminescence in semiconducting polymers”. In: *Nature* 397.6718 (1999), pp. 414–417.

[143] J. J. M. Halls et al. “Charge- and energy-transfer processes at polymer/polymer interfaces: A joint experimental and theoretical study”. In: *Physical Review B - Condensed Matter and Materials Physics* 60.8 (1999), pp. 5721–5727.

[144] J. Huang et al. “Efficient flexible polymer light emitting diodes with conducting polymer anodes”. In: *Journal of Materials Chemistry* 17 (2007), pp. 3551–3554.

[145] A. C. Morteani et al. “Barrier-Free Electron-Hole Capture in Polymer Blend Heterojunction Light-Emitting Diodes”. In: *Advanced Materials* 15.20 (2003), pp. 1708–1712.

[146] A. C. Morteani et al. “Exciton regeneration at polymeric semiconductor heterojunctions”. In: *Physical Review Letters* 92.24 (2004), pp. 1–4.

[147] J. Chappell et al. “Correlating structure with fluorescence emission in phase-separated conjugated-polymer blends”. In: *Nature Materials* 2.9 (2003), pp. 616–621.

[148] W. Renzi et al. “Exploring the experimental photoluminescence, Raman and infrared responses and density functional theory results for TFB polymer”. In: *Synthetic Metals* 236 (Feb. 2018), pp. 24–30.

[149] A. C. Arias et al. “Vertically segregated polymer-blend photovoltaic thin-film structures through surface-mediated solution processing”. In: *Applied Physics Letters* 80.10 (2002), pp. 1695–1697.

[150] H. J. Snaith et al. “Charge Generation Kinetics and Transport Mechanisms in Blended Polyfluorene Photovoltaic Devices”. In: *Nano Letters* 2.12 (2002), pp. 1353–1357.

[151] S. Reineke et al. “White organic light-emitting diodes with fluorescent tube efficiency”. In: *Nature* 459.7244 (2009), pp. 234–238.

[152] G. Schwartz et al. “Triplet harvesting in hybrid white organic light-emitting diodes”. In: *Advanced Functional Materials* 19.9 (2009), pp. 1319–1333.

[153] Y. Sun et al. “Management of singlet and triplet excitons for efficient white organic light-emitting devices”. In: *Nature* 440.7086 (2006), pp. 908–912.

[154] M. Lehnhardt et al. “Room temperature lifetime of triplet excitons in fluorescent host/guest systems”. In: *Organic Electronics* 12.3 (2011), pp. 486–491.

[155] Y. Luo and H. Aziz. “Correlation between triplet-triplet annihilation and electroluminescence efficiency in doped fluorescent organic light-emitting devices”. In: *Advanced Functional Materials* 20.8 (2010), pp. 1285–1293.

[156] M. Lebental et al. “Diffusion of triplet excitons in an operational organic light-emitting diode”. In: *Physical Review B - Condensed Matter and Materials Physics* 79.16 (2009), pp. 1–13.

[157] S. Baluschev et al. “Upconversion photoluminescence in poly(ladder-type-pentaphenylene) doped with metal (II)-octaethyl porphyrins”. In: *Applied Physics Letters* 86.6 (2005), pp. 1–3.

[158] F. Laquai et al. “Efficient upconversion fluorescence in a blue-emitting spirobifluorene- anthracene copolymer doped with low concentrations of Pt(II)octaethylporphyrin”. In: *Journal of Chemical Physics* 123.7 (2005).

[159] A. Monguzzi, R. Tubino, and F. Meinardi. “Upconversion-induced delayed fluorescence in multicomponent organic systems: Role of Dexter energy transfer”. In: *Physical Review B - Condensed Matter and Materials Physics* 77.15 (2008), pp. 3–6.

[160] A. J. Sandee et al. “Solution-processible conjugated electrophosphorescent polymers”. In: *Journal of the American Chemical Society* 126.22 (2004), pp. 7041–7048.

[161] F. Galbrecht et al. “Semiconducting polyfluorenes with electrophosphorescent on-chain platinum-salen chromophores”. In: *Chemical Communications* 18 (2005), pp. 2378–2380.

[162] S. T. Hoffmann et al. “Triplet energy transfer in conjugated polymers. III. An experimental assessment regarding the influence of disorder on polaronic transport”. In: *Physical Review B - Condensed Matter and Materials Physics* 81.16 (2010), pp. 1–6.

[163] E. J. W. List et al. “The Effect of Keto Defect Sites on the Emission Properties of Polyfluorene-Type Materials”. In: *Advanced Materials* 14.5 (2002), pp. 374–378.

[164] A. Köhler and D. Beljonne. “The singlet-triplet exchange energy in conjugated polymers”. In: *Advanced Functional Materials* 14.1 (2004), pp. 11–18.

[165] C. Rothe and A. Monkman. “Dynamics and trap-depth distribution of triplet excited states in thin films of the light-emitting polymer poly(9,9-di(ethylhexyl)fluorene)”. In: *Physical Review B - Condensed Matter and Materials Physics* 65.7 (2002), pp. 1–4.

[166] C. Rothe et al. “Triplet exciton state and related phenomena in the β-phase of poly(9,9-dioctyl)fluorene”. In: *Physical Review B - Condensed Matter and Materials Physics* 70.19 (2004), pp. 1–10.

[167] C. Rothe and A. P. Monkman. “Triplet exciton migration in a conjugated polyfluorene”. In: *Physical Review B - Condensed Matter and Materials Physics* 68.7 (2003), pp. 1–11.

[168] J. S. Wilson et al. “Triplet states in a series of Pt-containing ethynylenes”. In: *Journal of Chemical Physics* 113.17 (Nov. 2000), pp. 7627–7634.

[169] B. Kraabel, D. Moses, and A. J. Heeger. “Direct observation of the intersystem crossing in poly(3-octylthiophene)”. In: *The Journal of Chemical Physics* 103.12 (1995), pp. 5102–5108.

[170] B. Movaghar et al. “Diffusion and relaxation of energy in disordered organic and inorganic materials”. In: *Physical Review B - Condensed Matter and Materials Physics* 33.8 (1986), pp. 5545–5554.

[171] S. Athanasopoulos et al. “To hop or not to hop? Understanding the temperature dependence of spectral diffusion in organic semiconductors”. In: *Journal of Physical Chemistry Letters* 4.10 (2013), pp. 1694–1700.

[172] L. S. Devi et al. “Triplet energy transfer in conjugated polymers. I. Experimental investigation of a weakly disordered compound”. In: *Physical Review B - Condensed Matter and Materials Physics* 78.4 (2008), pp. 1–8.

[173] I. I. Fishchuk et al. “Triplet energy transfer in conjugated polymers. II. A polaron theory description addressing the influence of disorder”. In: *Physical Review B - Condensed Matter and Materials Physics* 78.4 (2008), pp. 1–8.

[174] S. T. Hoffmann et al. “Spectral diffusion in poly(para-phenylene)-type polymers with different energetic disorder”. In: *Physical Review B - Condensed Matter and Materials Physics* 81.11 (2010), pp. 1–8.

[175] H. F. Haneef, A. M. Zeidell, and O. D. Jurchescu. “Charge carrier traps in organic semiconductors: A review on the underlying physics and impact on electronic devices”. In: *Journal of Materials Chemistry C* 8.3 (2020), pp. 759–787.

[176] A. Rose. “Space-Charge-Limited Currents in Solids”. In: *Physical Review* 97.6 (1955), pp. 1538–1544.

[177] M. A. Lampert. “Simplified theory of space-charge-limited currents in an insulator with traps”. In: *Physical Review* 103.6 (1956), pp. 1648–1656.

[178] P. Mark and W. Helfrich. “Space-charge-limited currents in organic crystals”. In: *Journal of Applied Physics* 33.1 (1962), pp. 205–215.

[179] S. Nespurek and E. A. Silinsh. “Space-Charge-Limited Current Theory for Molecular Crystals with Gaussian Distribution of Local Trapping States”. In: *Physica Status Solidi (A) Applied Research* 34.2 (1976), pp. 747–759.

[180] H. T. Nicolai, M. M. Mandoc, and P. W. M. Blom. “Electron traps in semiconducting polymers: Exponential versus Gaussian trap distribution”. In: *Physical Review B - Condensed Matter and Materials Physics* 83.19 (2011), pp. 1–5.